https://doi.org/10.5194/egusphere-2026-4713
Preprint. Discussion started: 21 August 2026


# Mixed-Phase Microphysical Evolution in Large Eddy Simulations of Tropical Cumulus Congestus: Developing and Evaluating a Laboratory-based Ice Multiplication Parameterization of Freezing Drops

McKenna W. Stanford[1,2,a], Alice Keinert[3], Ann M. Fridlind[2], Alexei A. Kiselev[3], Daniel A. Knopf[4,5], Andrew S. Ackerman[2], Thomas Leisner[3,6], and Paul Lawson[7]

[1]Center for Climate Systems Research (CCSR), Columbia University, New York, New York
[2]NASA Goddard Institute for Space Studies (GISS), New York, New York
[3]Institute of Meteorology and Climate Research Atmospheric Aerosol Research, Karlsruhe Institute of Technology (KIT), Karlsruhe, Germany
[4]School of Marine and Atmospheric Sciences, Stony Brook University, Stony Brook, NY, USA
[5]Department of Chemistry, Stony Brook University, Stony Brook, NY, USA
[6]Institut für Umweltphysik, Universität Heidelberg, Heidelberg, Germany
[7]Stratton Park Engineering Company, Inc., Boulder, CO, USA
[a]Current affiliation: Atmospheric, Climate, and Earth Sciences Division, Pacific Northwest National Laboratory, Richland, WA, USA

**Correspondence:** McKenna W. Stanford (mckenna.stanford@pnnl.gov)

**Abstract.** Ice microphysical processes modulate cloud structure, evolution, and Earth's radiative balance, yet secondary ice production (SIP)—whereby fragmentation enhances ice number concentrations ($N_{\mathrm{ice}}$) beyond what ice-nucleating particle (INP) populations alone can explain—remains poorly constrained. We develop a drop-shattering parameterization based on laboratory-observed pressure release event frequencies during drop freezing and evaluate it, alongside a water-activity-based immersion-freezing model for primary ice formation, in large eddy simulations (LES) of a tropical cumulus congestus case from NASA CAMP$^2$Ex—the second of a two-part study extending liquid-phase results from Part I into the mixed-phase region. Bin and double-moment bulk simulations are evaluated against in situ aircraft observations from 0 to $-15$°C. The baseline parameterization negligibly enhances $N_{\mathrm{ice}}$; a $10\times$ multiplier on per-event splinter numbers—reflecting substantial production uncertainty—increases $N_{\mathrm{ice}}$ by 1–2 orders of magnitude. The bulk scheme reaches localized maxima near $10^3$ L$^{-1}$, while the bin scheme reaches 10–20 L$^{-1}$, reflecting fundamentally different collision-kernel structures between the schemes. A primary–secondary ice feedback emerges exclusively in the bin scheme, driven by INP enrichment of precipitation-sized drops through collision-coalescence and INP accumulation; this feedback is absent in the bulk scheme due to its lack of aerosol core mass tracking. The $10\times$ parameterization partially reconciles a 1–2 order-of-magnitude deficit in simulated concentrations for sizes $>$200 $\mu$m relative to observed particle size distributions, with turbulence-induced collision enhancement essential for conditioning SIP efficiency. Together, these bin and bulk implementations provide a foundation for improving SIP representation in large-scale models.

https://doi.org/10.5194/egusphere-2026-4713
Preprint. Discussion started: 21 August 2026


## 1 Introduction

Ice production in clouds plays a crucial role in understanding their microphysical and macrophysical structure, evolution, and radiative properties (Cantrell and Heymsfield, 2005; Sullivan et al., 2018). Observed ice number concentrations ($N_{\text{ice}}$) often exceed concentrations of ice nucleating particles (INPs) by orders of magnitude (Ladino et al., 2017; Lasher-Trapp et al., 2016; Hallett and Mossop, 1974; Heymsfield and Willis, 2014; Taylor et al., 2016), suggesting that primary ice nucleation plays a subordinate role in realizing observed $N_{\text{ice}}$. This discrepancy is generally attributed to ice multiplication, or secondary ice production (SIP), in which ice particles undergo a fragmentation mechanism to enhance $N_{\text{ice}}$, often in an explosive manner (Korolev and Leisner, 2020). The considerable uncertainties that exist in understanding ice multiplication processes and their wide-ranging implications on weather and climate simulation have recently motivated detailed laboratory experiments (e.g., Lauber et al., 2018; Keinert et al., 2020b; Kleinheins et al., 2021a; Seidel et al., 2023), improved remote sensing techniques capable of detecting SIP (e.g., Luke et al., 2021; Li et al., 2021; Billault-Roux et al., 2023; Pfeifer et al., 2025), and the devoted Secondary Production of Ice in Cumulus Experiment (SPICULE) airborne field campaign (Lawson et al., 2023). A persistent consequence of these uncertainties is a systematic underproduction of $N_{\text{ice}}$ in numerical models relative to observations, with downstream impacts on simulated radar reflectivity, ice crystal size distributions, and the partitioning of precipitation between convective and stratiform regions in organized convective systems (e.g., Blossey et al., 2007; Li et al., 2008; Matsui et al., 2009; Lang et al., 2011, 2014; Varble et al., 2011, 2014; Caine et al., 2013; Franklin et al., 2016; Stanford et al., 2017; Han et al., 2019; Qu et al., 2022).

A review by Korolev and Leisner (2020) identified three well-established SIP mechanisms: (1) rime-splintering (Hallett-Mossop), (2) shattering during drop freezing, and (3) fragmentation due to ice-ice collisions. The most widely studied process—rime-splintering—was initially proposed by Hallett and Mossop (1974) and Mossop and Hallett (1974), where ice particles collide with supercooled droplets, undergo riming, and subsequent splintering proceeds. This process occurs within a temperature range from -3 to -8 °C, though additional multiplication mechanisms are often observed within and outside of this range (e.g., Lawson et al., 2015). However, recent laboratory experiments suggest limited to no evidence of the Hallett-Mossop process as a productive SIP mechanism (Seidel et al., 2023). Ice-ice collisions causing mechanical fragmentation have also been suggested to contribute to enhanced $N_{\text{ice}}$ (e.g., Phillips et al., 2017a, b), particularly in turbulent convective clouds.

Recent studies have emphasized the potential prevalence of the drop shattering mechanism, or fragmentation of freezing drops (FFD), particularly in tropical cumuli and mesoscale convective systems (e.g., Lawson et al., 2015; Huang et al., 2017, 2022; Korolev et al., 2024; Sullivan et al., 2018; Korolev et al., 2020; Qu et al., 2020; Lauber et al., 2021; Luke et al., 2021; Lawson et al., 2022; Billault-Roux et al., 2023; Lachapelle et al., 2025; Pfeifer et al., 2025). As the supercooled droplet begins to freeze, latent heat is released and an ice shell forms, surrounding the interior liquid. Internal pressure builds from the inward growth of the ice shell and is released, leading to explosive fragmentation of the drop. However, recent work has shown that these pressure release events are not limited to a generalized complete shattering of the ice shell, but rather undergo a variety of mechanisms that result in matter being ejected from the freezing drop without necessary complete shattering (Lauber et al., 2018; Keinert et al., 2020b; Kleinheins et al., 2021a). For example, Lauber et al. (2018) introduced evidence of events

https://doi.org/10.5194/egusphere-2026-4713
Preprint. Discussion started: 21 August 2026


characterized as breakups, crackings, bubble bursts, and jettings during freezing of levitated drops, while Keinert et al. (2020b) showed an enhancement of drop shattering probability by these same mechanisms for drizzle drops falling at terminal velocity.

In Stanford et al. (2025, hereafter Part I), we developed an aerosol-constrained case study simulation to evaluate drop size distribution (DSD) evolution in tropical cumulus congestus observed during the NASA Cloud, Aerosol, and Monsoon Processes Philippines Experiment (CAMP$^2$Ex; Reid et al., 2023). Constrained by airborne polarimetry retrievals and viewing evolution from a thermal-based perspective, it was shown that DSDs broaden with height and droplet number concentrations ($N_d$) decrease with height. This DSD evolution is consistent with an active collision-coalescence process, which is potentially important for FFD because enhanced $N_{\mathrm{ice}}$ probabilities have been shown to increase with drop size (e.g. Field et al., 2006; Phillips et al., 2018; Lauber et al., 2018). Lawson et al. (2022) proposed an active collision-coalescence process as essential to produce copious ice particles observed in several tropical cumulus congestus field campaigns. Indeed, the degree to which $N_d$ decreased with height (coincident with DSD broadening) in Part I was modulated by the efficiency of collision-coalescence. By constraining the warm-phase microphysical evolution of growing cumulus congestus in Part I, this Part II study extends evaluation of to the ice phase.

Aircraft measurements from the cumulus congestus case study evaluated in Part I show evidence of ice multiplication via particle imagery of broken frozen drops and spicules. Herein, laboratory experiments from Keinert et al. (2020b) and Kleinheins et al. (2021a) are composited to develop an ice multiplication parameterization for FFD as a function of drop size and temperature with a narrow focus on fragments emitted during pressure release events. This size-temperature dependence is consistent with the dominant controls of shattering probability (e.g. Takahashi et al., 1977; Kolomeychuk et al., 1975), similar to the parameterization developed by Phillips et al. (2018) which composited the majority of past laboratory-based studies for FFD.

The parameterization is implemented into both bin (size-resolved) and bulk microphysics schemes and evaluated in large eddy simulations (LES) of the case study described in Part I that realized cloud top temperatures (CTTs) down to -15 °C, though the parameterization is applicable to temperatures down to -30 °C. In-situ aircraft measurements of PSDs from CAMP$^2$Ex, spanning the mixed-phase region, are used as a first constraint for evaluation. We further explore potential feedback mechanisms between primary ice production (PIP) and SIP and the role of turbulence-induced collision enhancement in modulating SIP.

The remainder of this article is structured as follows: a description of the laboratory experiments and empirical parameterization construction are provided in Section 2. Details of the LES, microphysics schemes and their PIP and SIP parameterizations, and aircraft measurements are described in Section 3. Simulation results and observational comparisons are presented in Section 4. A discussion is provided in Section 5 followed by conclusions in Section 6. A complete list of symbols, variables, and acronyms is provided in Appendix D.

https://doi.org/10.5194/egusphere-2026-4713
Preprint. Discussion started: 21 August 2026


## 2 Laboratory Experiments and Parameterization Construction

Experimental data follow from Keinert et al. (2020b) and Kleinheins et al. (2021a), performed at the Karlsruhe Institute of Technology (KIT). These experiments spanned temperatures from -5 to -25 °C and a drop diameter of 300 $\mu$m. Pure water droplets were levitated in electrodynamic balance (Hoffmann et al., 2013) with an airflow resembling terminal velocity at $\approx$ 1.3 m s$^{-1}$. Freezing was initiated by injecting fine ice crystals into the airflow. SIP events were recorded using a high-resolution infrared thermography system (ImageIR 7340, InfraTec GmbH) and a high speed video (HSV) camera (Phantom v710, Vision Research). The thermography system measured the surface temperature of the droplet and the pressure of the liquid core was inferred using the relationship for pressure-dependent melting point depression (Kleinheins et al., 2021a). Pressure release events (PREs) were identified by the thermography system, while the HSV camera captured changes in shape and structure of the droplet and identification of ejected matter or other phenomena (e.g., bubble bursting).

For parameterization development, we distinguish between large ice fragments and tiny ice splinters. Here, large fragments are defined as $> 5$ $\mu$m diameter and are potentially visible in the high speed video footage. A common example of a large fragment is the broken halves of a drop after it completely cracks and separates. We focus here only on ice multiplication events that lead to production of tiny ice splinters, justified by the expectation that large fragments contribute significantly less to SIP-produced $N_{\text{ice}}$ relative to tiny fragments. This sensitivity is explored by scaling the assumption of one large fragments vs. ten tiny splinters (Section 4). However, we note that future work can easily include the explicit contribution by large fragments as demonstrated by Phillips et al. (2018). In the KIT laboratory experiments, we were able to quantify the number of events that could lead to tiny splinter production (e.g. PREs, breakup, jetting, bubble bursts), but not the exact number of ejected splinters because such particles are too small to be detected by the HSV microscopy system. Nonetheless, since the PRE event frequency was measured over a broad temperature range, this data provides valuable insight into the temperature dependence of splinter production events.

Based on the results of Kleinheins et al. (2021a), the number of potential splinter production events increases with decreasing temperature (Fig. 1). Applying a polynomial fit to the experimental data yields the following expression representing the number of PREs ($n_{\text{PRE}}$):

$$n_{\text{PRE}}(T) = -0.0046T^2 - 0.2854T + 2.838\,, \tag{1}$$

where $T$ is temperature in degrees Celsius. This yields a PRE number of 4 for a droplet freezing at -5 °C, increasing to 7 events at -25 °C, and an asymptote for temperatures colder than -30 °C. This increase with decreasing temperature notably differs from the thermal peak $\approx$ -15 °C that characterizes large fragment production (Lauber et al., 2018; Keinert et al., 2020b) and from previously established parameterizations for SIP production from FFD (e.g. Phillips et al., 2018).

Following Phillips et al. (2018), we extract information on the size-dependence for tiny splinter production using past literature. Criteria for study inclusion is that droplets were able to rotate freely in experiments, while either being levitated in airflow or experiencing free fall. Rotation during droplet freezing ensures the symmetry of spherical heat loss of the ice shell to the environment, which has a strong influence on the SIP event frequency, as experimentally demonstrated by Johnson and

https://doi.org/10.5194/egusphere-2026-4713
Preprint. Discussion started: 21 August 2026


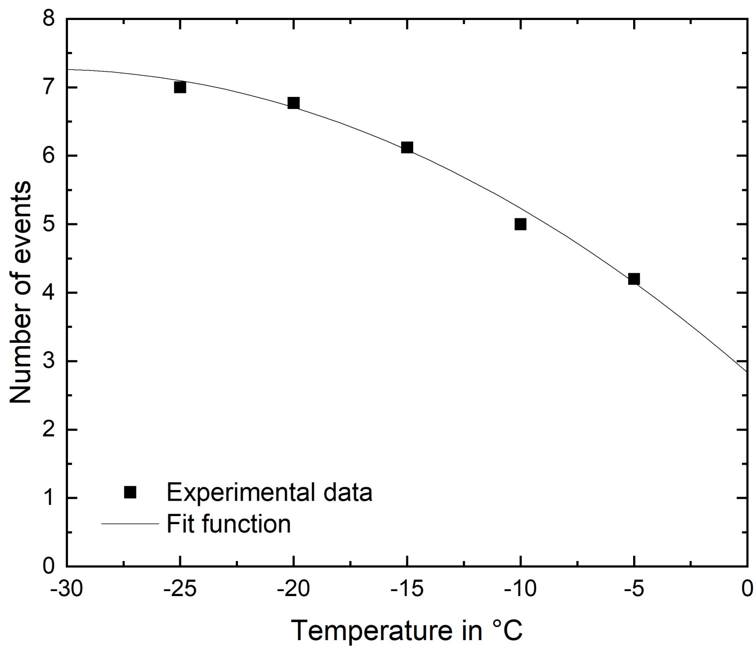


**Figure 1.** Fit function for the number of pressure release events ($n_{\mathrm{PRE}}$) for droplets of 300 $\mu$m in diameter as a function of temperature. Squares show the individual experimental data points.

Hallett (1968). Two experimental studies meet this criteria, while providing the number of tiny fragments produced during droplet freezing: Takahashi et al. (1977) and Kolomeychuk et al. (1975) (hereafter TY77 and K75, respectively).

TY77 utilized a cloud chamber 14.7 m in height to detect ice multiplication from drop sizes ranging from 50 to 500 $\mu$m and temperatures ranging from $\approx$ -6 °C to -17 °C. They conducted 19 experiments at different temperatures and drop sizes with 5000 - 20000 droplets in each experiment. Droplets were frozen with silver iodide in suspension. Splinter detection was performed via impaction on silicone oil at the bottom of the chamber and the number of splinters was controlled relative to the number of background crystals.

For sizes larger than 500 $\mu$m, K75 tested 75 drops with an average diameter of 1.6 mm (range 1.2 to 1.9 mm). Drops were levitated in a water-saturated nitrogen stream and no seeding was used for freezing initiation. Droplets froze at a median temperature of -18 °C, ranging from -12 °C to -25 °C. Splinters were measured via impaction on a supercooled sugar solution with negligible background crystals contributing to total ice number. On average, a frozen drop produced 9.4 splinters, with 7 of the 75 drops producing 50-150 splinters each and dominating overall fragmentation numbers.

The final parameterization describing the number of tiny splinters as a function of drop size and temperature, $N_t(D,T)$, is developed by expanding $n_{\mathrm{PRE}}(T)$ into the third dimension with the drop size dependence, which incorporates the number of splinters, described by a linear fit between the two studies with one-to-one weighting. Surfaces of $N_t(D,T)$ are shown in

https://doi.org/10.5194/egusphere-2026-4713
Preprint. Discussion started: 21 August 2026


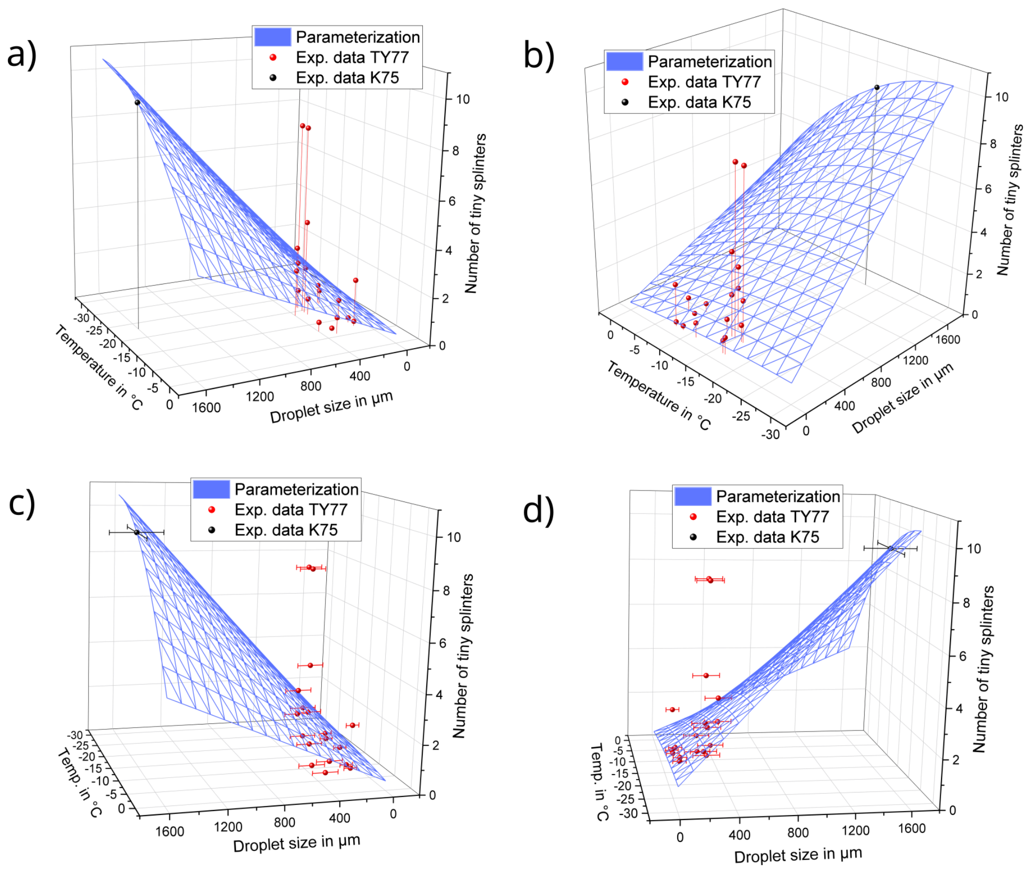


**Figure 2.** Surfaces for the number of tiny splinters as a function of drop diameter and temperature. Dots and lines in (a) and (b) represent the exact data points from TY77 (red dots, their Table 1) and K75 (black dot, their Table 4) with lines extended to the surface. Lines in (c) and (d) show error bars for each data point. Panels (b) and (d) are rotated projections of (a) and (c), respectively.

Fig. 2. The resulting piecewise linear formulation is given by

$$N_t(D,T) = \begin{cases} (-0.0046T^2 - 0.2854T + 2.838)(0.0008D + 0.136) & 50\,\mu m < D \leq 1600\,\mu m \\ 1.416(-0.0046T^2 - 0.2854T + 2.838) & D > 1600\,\mu m \end{cases} \tag{2}$$

where $D$ is drop diameter in $\mu$m for a given temperature. The number of splinters is assumed to be constant for diameters $> 1600$ $\mu$m, which is supported by recent studies. Lachapelle et al. (2025) evaluated in-situ aircraft observations collected during ice pellet precipitation events and found that the Lawson et al. (2015) FFD parameterization, which predicts the fragment number as proportional to the fourth power of diameter, required a constant size dependence for drops larger than 950 $\mu$m in order to realize observed $N_{\rm ice}$. They also established an observed range of 5-8 splinters per drop, similarly to the parameterization developed here. In addition, Pfeifer et al. (2025) evaluated observations of a rain re-freezing event and reported 1-6 splinters

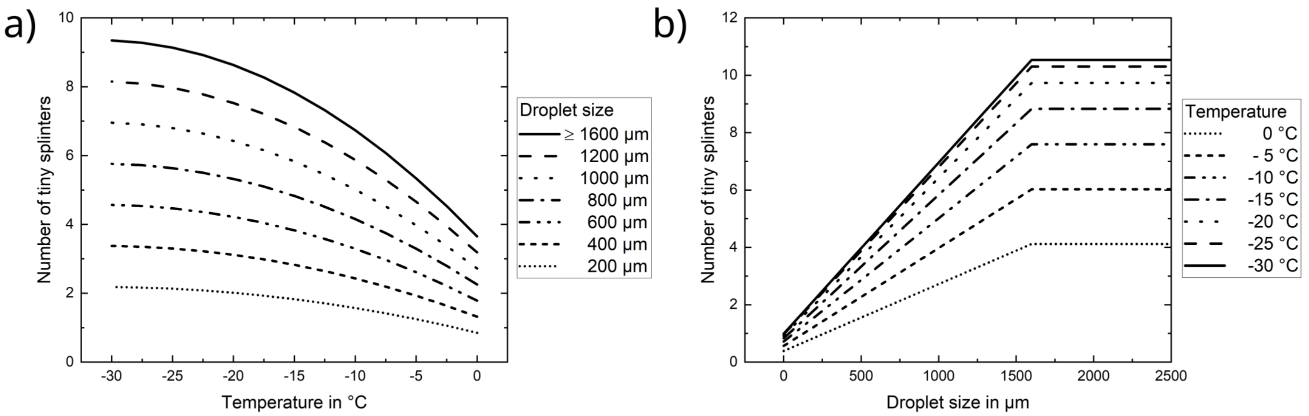


**Figure 3.** Parameterized number of tiny splinters ($N_t$) as a function of (a) temperature for different drop sizes and (b) drop diameter for different temperatures.

per drop with an optimal size range of 0.5-1 mm without substantial increase in probabilities for larger sizes. While their dataset does not allow for providing additional data points which could be used in our parameterization, their observations support leveling off of the number of secondary ice splinters for super-mm freezing rain droplets. Fig. 3 shows the final parameterization of $N_t$ as a function of temperature for various drop sizes (Fig. 3a) and as a function of drop size for various temperatures (Fig. 3b). A 3D surface of $N_t$ is also provided in in Fig. 4.

We note several important distinctions about this parameterization construction. First, only the event frequency associated with tiny splinter production was able to be measured in the laboratory experiments (Fig. 1), but not the exact fragment number, for which we rely on limited literature data. This sensitivity is tested by applying a 10-fold multiplicative factor to $N_t$ (Section 4). Although past literature has scaled splinter number production to yield size dependencies and associated fragment numbers, the number of splinters remains the most uncertain component of the parameterization. Second, the parameterization is truncated at -30 °C, which is sufficient for the current study where observed CTTs reach only -15 °C at their coldest. Nonetheless, the asymptote of $N_t$ for temperatures colder than -30 °C (Fig. 1) suggests that a linear extrapolation beyond -30 °C may be valid. Third, for simplicity, we assume that the splinter numbers increase linearly with droplet size (up to 1.6 mm) since there is lack of experimental data for SIP production for drops larger than those studied by K75 and further supported by the recent observational studies suggesting limited size dependencies on SIP for sizes $> \approx 1$ mm (Lachapelle et al., 2025; Pfeifer et al., 2025). Finally, there is limited literature evidence to support extrapolating the lower size limit beyond 50 $\mu$m. No production of large fragments has been observed in experimental settings close to atmospheric conditions for droplets smaller than 50 $\mu$m in diameter (Hobbs and Alkezweeny, 1968). Adkins (1960) found no evidence of tiny fragments produced from droplets between 4 $\mu$m and 13 $\mu$m in diameter and Bader et al. (1974) found no tiny ice particles in excess to background ice crystal concentration for droplets freezing in thermal equilibrium at diameters of 30 $\mu$m and 42 $\mu$m. Therefore, we assume no tiny splinter production for droplets smaller than 50 $\mu$m in diameter.

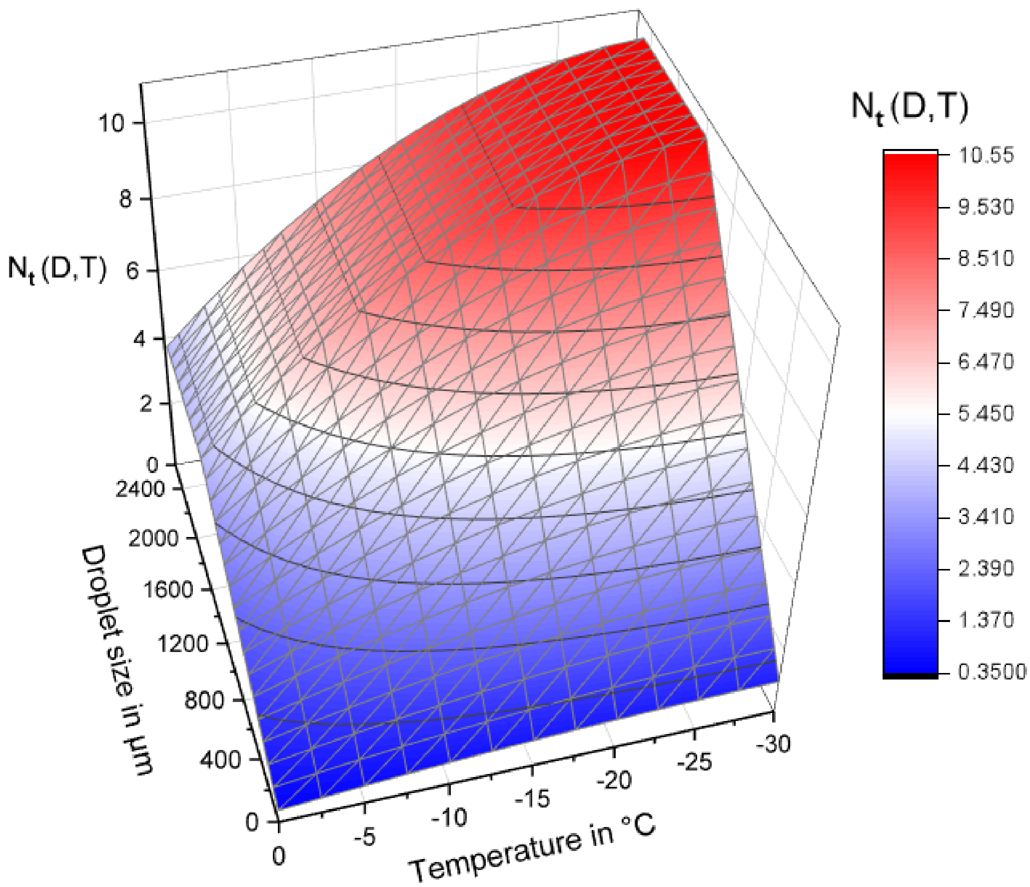


**Figure 4.** Final piecewise-linear formulation of the number of tiny splinters ($N_t$) as a function of drop diameter and temperature.

## 3 Data and Experimental Design: Large Eddy Simulations, SIP Parameterizations, and Aircraft Measurements

### 3.1 Large Eddy Simulations

The Distributed Hydrodynamic Aerosol and Radiative Modeling for Atmospheres (DHARMA; Stevens and Bretherton, 1996; Stevens et al., 2002; Ackerman et al., 2000) LES code is used here with the same set-up as Part I. Briefly, the model is run with doubly periodic boundary conditions on a 19.2 x 19.2 km domain, a horizontal mesh of 100 m, vertical grid spacing that increases between 20 and 100 m within the relevant tropospheric depth, and a dynamics time step of 1 s. Subgrid-scale fluxes are parameterized using a dynamic Smagorinsky turbulence model (Kirkpatrick et al., 2006) and ocean surface fluxes follow the bulk aerodynamic formula from Zeng et al. (1998). Simulations from Part I showed an evolving field of thermals that reached successively higher heights before transiting sub-0 °C altitudes, after which ice production commences in the simulations evaluated herein. We refer to Part I for further details on the evolution of liquid DSDs prior to reaching 0°C.

https://doi.org/10.5194/egusphere-2026-4713
Preprint. Discussion started: 21 August 2026


**Table 1.** Simulation Details.

| Simulation Name | Description |
|---|---|
| BIN_CNTL | Bin microphysics setup described in text |
| BULK_CNTL | Bulk microphysics setup described in text |
| BIN_SIP | As in BIN_CNTL but with FFD ice multiplication parameterization implemented |
| BULK_SIP | As in BULK_CNTL but with FFD ice multiplication parameterization implemented |
| BIN_SIP_10X | As in BIN_SIP but with a multiplicative factor of 10 applied to Eq. 2 |
| BULK_SIP_10X | As in BULK_SIP but with a multiplicative factor of 10 applied to Eq. 2 |
| BIN_NOTURB | As in BIN_CNTL but without turbulence-induced collision enhancement |
| BIN_NOTURB_SIP | As in BIN_SIP but without turbulence-induced collision enhancement |
| BIN_NOTURB_SIP_10X | As in BIN_SIP_10X but without turbulence-induced collision enhancement |

In Part I, the large-scale vertical motion profiles (Part I's Fig. 3) represented a dipole of ascent below 5 km and subsidence between 5 and 10 km. Here, the dipole transition is increased to 7 km to enable more developed growth of turrets through the 0 to -15 °C layer where observed ice multiplication was evident. We note that the large-scale vertical motion profile is not well-constrained and was indeed highly variable in mesoscale simulations from which the profile was derived, such that the profile used here lies within that variability. The SIP parameterization is implemented into the Community Aerosol-Radiation-Microphysics Application (CARMA) bin microphysics scheme (Ackerman et al., 1995; Jensen et al., 1998) and the double moment bulk microphysics scheme described in Part I. Each of these schemes are subsequently described, and a complete list of the associated simulations for each scheme are provided in Table 1. Importantly, we note that the term "SIP" hereafter refers only to the FFD process. Exploring other SIP mechanisms is beyond the scope of this work, though we provide sensitivity tests that include the Hallett-Mossop process in Appendix C and discuss these additional SIP mechanisms, the observational evidence for their activity in this case, and the implications for neglecting them in Section 5.

### 3.1.1 Bin Microphysics

CARMA explicitly resolves PSD shape for species including unactivated aerosol, liquid water, and ice. All species use 50 mass-doubling bins for number concentration following a mass ratio of 1.35 for aerosol and 1.65 for liquid and ice. Aerosols are represented as ammonium bisulfate for which the dissolved component (core mass) is tracked in the liquid and ice species. As in Part I, the aerosol size distribution is represented by the sum of three lognormal modes roughly corresponding to nucleation, Aitken, and accumulation modes that vary with height. Each bin has a hygroscopicity of 0.4. The mass of the smallest aerosol bin corresponds to a diameter of $\approx$ 10 nm and the largest bin a diameter of $\approx$ 1.5 $\mu$m. For liquid, the smallest size bin equals that of a 2 $\mu$m drop and the largest bin a diameter of 7.78 mm.

https://doi.org/10.5194/egusphere-2026-4713
Preprint. Discussion started: 21 August 2026


For ice, properties are representative of a dense ice class that is most representative of the freezing drops we aim to simulate. We follow the approach developed by Böhm (1989, 1992a, b, c, 1994, 1999, 2004) in which the mass, maximum dimension, projected area, and aspect ratio assigned to each bin are used to calculate hydrometeor fall speeds and collision efficiencies. Following van Diedenhoven et al. (2012), the power law relationships between an ice crystal's maximum dimension ($D_{\max}$) and its mass and projected areas are taken from Mitchell (1996) such that ice crystals with $D_{\max} < 5$ $\mu$m are assumed to be solid spheres, particles with $D_{\max} > 200$ $\mu$m are assumed to take the form of lump graupel reported by Mitchell (1996), and an interpolation technique represents the transition range between 5-200 $\mu$m. Aspect ratios are unity for $D_{\max} < 5$ $\mu$m, 0.8 for $D_{\max} > 200$ $\mu$m, and are linearly interpolated in between. Together, these yield a mass grid in which the smallest bin represents a $D_{\max}$ of 2.25 $\mu$m and the largest bin a $D_{\max}$ of 17.8 mm. Capacitance is calculated assuming oblate spheroids to approximate the impact of ice habit on vapor deposition and sublimation rates (Pruppacher and Klett, 2010).

Fast microphysical processes such as condensation and vapor exchange are calculated with a minimum timestep of 0.1 s while slower processes such as collision-coalescence operate on the native timestep. Aerosol activation occurs when the supersaturation exceeds a critical value defined by the Köhler equilibrium relations. Collision-coalescence follows from the exponential collection scheme of Bott (1998) to solve the stochastic collection equation. Liquid-liquid collisions use coalescence efficiencies from Beard and Ochs (1984) and collision efficiencies from Hall (1980); the Hall (1980) collision efficiencies are also applied to ice-containing pairs as an approximation. The coalescence efficiency for liquid-ice collisions is unity and 0.1 for ice-ice collision of nondendritic crystals under dry-growth conditions (Mitchell, 1996; Wang and Chang, 1993). Part I showed that turbulence-induced collision enhancement was important for properly representing DSD broadening. We retain the theoretical turbulent collision kernel from Ayala et al. (2008) that follows from the description by Lee et al. (2021), which uses the explicitly calculated turbulent kinetic energy dissipation rate ($\varepsilon$) from the subgrid-scale (SGS) diffusion scheme and the collision efficiency enhancement from Wang and Grabowski (2009). As in Part I, we scale the SGS turbulence scheme's native $\varepsilon$ by a factor of 10 based on the finding that (1) the total mean dissipation rate was underestimated by that factor relative to the native SGS computation and (2) employing this multiplier yielded DSDs most in agreement with observations at $\approx 1$ °C. Turbulent-induced collision enhancement is similarly applied here to liquid-ice and ice-ice collisions. To investigate the impact of turbulent enhancement on SIP, whether by producing larger drops lofted to the freezing level or by enhancing collision-induced freezing, we perform sensitivity tests with the turbulence-induced collision enhancement neglected (Section 4.5).

A baseline simulation (BIN_CNTL) neglects SIP processes and is integrated for 12 hours. The BIN_SIP simulation includes SIP (described in the following subsection and Appendix B), and the BIN_SIP_10X simulation scales splinter production by a factor of 10. These simulations are restarted at 6 hours from BIN_CNTL, which is the time that PIP initiates, and 3D model fields are output every 10 minutes. The BIN_NOTURB, BIN_SIP_NOTURB, and BIN_SIP_10X_NOTURB simulations follow these respective setups but without turbulence-induced collision enhancement.

**Bin-Implemented Primary and Secondary Ice Formation**

A full description of PIP and SIP parameterization derivations are provided in Appendices A and B, respectively. A brief overview is given here. Primary ice formation is considered active only via the immersion nucleation of ice nucleating particles

https://doi.org/10.5194/egusphere-2026-4713
Preprint. Discussion started: 21 August 2026


(INPs) and follows the water activity ($a_w$) based immersion freezing model (ABIFM; Knopf and Alpert, 2013). ABIFM follows from classical nucleation theory and represents heterogeneous freezing as a stochastic process dependent only on the INP properties and the thermodynamic state of the supercooled drop. The freezing rate is defined as the product of an ice nucleation rate coefficient ($J_{\mathrm{het}}$; cm$^{-2}$ s$^{-1}$), the surface area of INP ($s_{\mathrm{INP}}$; cm$^2$), and the INP number concentration ($N_{\mathrm{INP}}$; cm$^{-3}$), where $J_{\mathrm{het}}$ depends only on temperature for immersion freezing (see Appendix A1). The aerosol core mass inside liquid drops in the bin scheme is prognostic, which is used to compute $s_{\mathrm{INP}}$ assuming one INP per drop and that the INP is represented by an organic fraction of the total aerosol volume (0.3, see Appendix A2).

Ice multiplication as defined via Eq. 2 proceeds from drops freezing either primarily via immersion nucleation (ABIFM-induced multiplication, Appendix B2) or via collisions between liquid drops and ice (collision-induced multiplication, Appendix B1). Collisional SIP requires the liquid drop to be larger than the ice crystal. In addition to the drop-size and temperature dependencies (Eq. 2), ABIFM-induced multiplication is additionally controlled by ABIFM's own temperature dependence while collision-induced multiplication is conditioned on the collision kernel from Bott (1998, see Appendix B1.1). Ice splinters produced from either freezing mechanism are introduced into the smallest ice size bin ($D_{\mathrm{max}} \approx 2.25$ $\mu$m), with concordant mass, and the remainder of mass is retained in the ice bin corresponding to the frozen drop size. Finally, we present sensitivity tests that include the rime-splintering (Hallett-Mossop) ice multiplication process in Appendix C.

### 3.1.2 Bulk Microphysics

The bulk microphysics scheme is the same used in Part I for liquid microphysics with the addition of ice, with mixed-phased microphysics broadly following Morrison et al. (2005, 2009). This scheme includes prognostic number concentration and mass for cloud, rain, cloud ice, precipitating fluffy ice (i.e, snow), and precipitating dense ice (i.e., graupel) species that all assume gamma distributions. For liquid species, we retain the following setup from Part I: the Seifert and Beheng (2001) scheme for autoconversion and self-collection, the Seifert (2008) parameterization for rain accretion, self-collection, breakup, and fallspeed, and a gamma shape parameter of 3 for rain. Aerosol activation using Köhler theory following Abdul-Razzak and Ghan (2000) is employed for 3 aerosol modes roughly corresponding to nucleation, Aitken, and activation modes with a hygroscopicity of 0.4. All ice species use an exponential size distribution. Homogeneous freezing is neglected since clouds do not reach sufficient supercooling.

**Bulk-Implemented Primary and Secondary Ice Formation**

Primary ice formation proceeds only via immersion nucleation following ABIFM (Appendix A3). Aerosol core mass is not tracked in the bulk scheme. Instead, activated aerosol number concentrations in cloud droplets for each of the three lognormal aerosol modes is tracked. The total INP surface area for each mode is computed by integrating the second moment of the lognormal size distribution and summing across modes assuming an organic fraction of 0.3. This yields explicit surface area calculations for INPs in cloud droplets that freeze via ABIFM (Appendix A3.2). However, activated aerosol number is not tracked once cloud droplets are converted to rain via autoconversion and/or accretion (i.e., we assume a complete sink of aerosol upon conversion to rain). Therefore, we assume that the activated aerosol pool in rain drops is proportional to the ratio

https://doi.org/10.5194/egusphere-2026-4713
Preprint. Discussion started: 21 August 2026


of rain mass to total liquid condensate mass; the product of this ratio and the activated aerosol number concentration in cloud droplets is used as a proxy for the untracked aerosol inside rain drops (Appendix A3.3). Such an assumption can be violated, particularly in strongly precipitating regions where little cloud liquid water (and thus tracked, activated aerosol) are present, but is necessary without introducing a new prognostic that preserves activated aerosol number during collision-coalescence.

Ice multiplication proceeds via both ABIFM-induced freezing and collision-induced freezing. In both cases, the piecewise-linear formula given by Eq. 2 is converted to a gamma function analytical form suitable for use in double-moment bulk microphysics (Appendices B1.2 and B2.2) that frames the size-dependence of Eq. 2 using incomplete gamma functions. Given the lower size threshold for the FFD process (50 $\mu$m) and the typical modal diameter of the cloud droplet species ($\approx$ 20-30 $\mu$m), we assume that ABIFM-induced multiplication occurs only within the rain species. Upon freezing of rain drops via ABIFM, ice splinters are transferred to the cloud ice species assuming the mass of a spherical ice crystal with a diameter of 5 $\mu$m.

Collision-induced SIP is assumed to occur only between collisions of the rain and cloud ice species given the requirement that the liquid drop be larger than the ice crystal. Future work could extend this to collisions between rain drops and the fluffy ice species, conditioned on a size metric representing an average distribution size for each species, but as a start we do not consider these collisions. Therefore, collisions between cloud ice and rain assume a hydrodynamic collision kernel following Reisner et al. (1998) that is integrated over the size distributions using incomplete gamma functions, again assuming that the splinters have a mass equivalent to a 5 $\mu$m-diameter sphere and the remainder of the frozen drop is transferred to the precipitating ice species (Appendix B1.2). Bulk simulations include BULK_CNTL (no SIP), BULK_SIP (FFD enabled), and BULK_SIP_10X (multiplicative factor of 10 applied to Eq. 2's integration). Finally, we include additional sensitivity tests with the rime-splintering multiplication mechanism in Appendix C.

### 3.2 Aircraft Measurements

Airborne cloud probes from both the NASA P3-B aircraft and the Stratton Park Engineering Company's (SPEC) Learjet 35 are used for observational context of PSDs. PSDs are merged between instruments measuring different size ranges. On the Learjet, instrumentation includes the fast forward scattering spectrometer probe (FFSSP; O'Connor et al., 2008; Lawson et al., 2017), the 10-$\mu$m channel 2D-stereo (2D-S) optical array probe (Lawson et al., 2006), the high-volume precipitation spectrometer probe (HVPS; Lawson et al., 1998), and the Nevzorov liquid and total water content device (Korolev et al., 1998). On the P3-B, instrumentation includes the fast cloud droplet probe (FCDP; O'Connor et al., 2008; Lawson et al., 2017), the 2D-S, and the HVPS. PSDs are composited across "cloud passes", as in Part I, determined by contiguous segments with total water content (TWC) exceeding 0.1 g m$^{-3}$. Each aircraft was also equipped with a 3-view cloud particle imager (3V-CPI; Lawson et al., 2001) that provides high-resolution cloud particle images over a size range of 2.3-2300 $\mu$m (e.g., Fig. 5). We limit analysis to cloud passes where average vertical velocities exceed 1 m s$^{-1}$ since in situ sampling targeted growing turrets and ice multiplication signals were primarily observed within and surrounding updrafts. Size thresholds used to stitch the instruments vary based on the measured cloud pass such that robust statistical samples across a range of size bins are realized. In general, the FFSSP/FCDP are used for sizes below 40-50 $\mu$m, the 2D-S is used for sizes between the FFSSP/FCDP up to 300-1000 $\mu$m, and

https://doi.org/10.5194/egusphere-2026-4713
Preprint. Discussion started: 21 August 2026


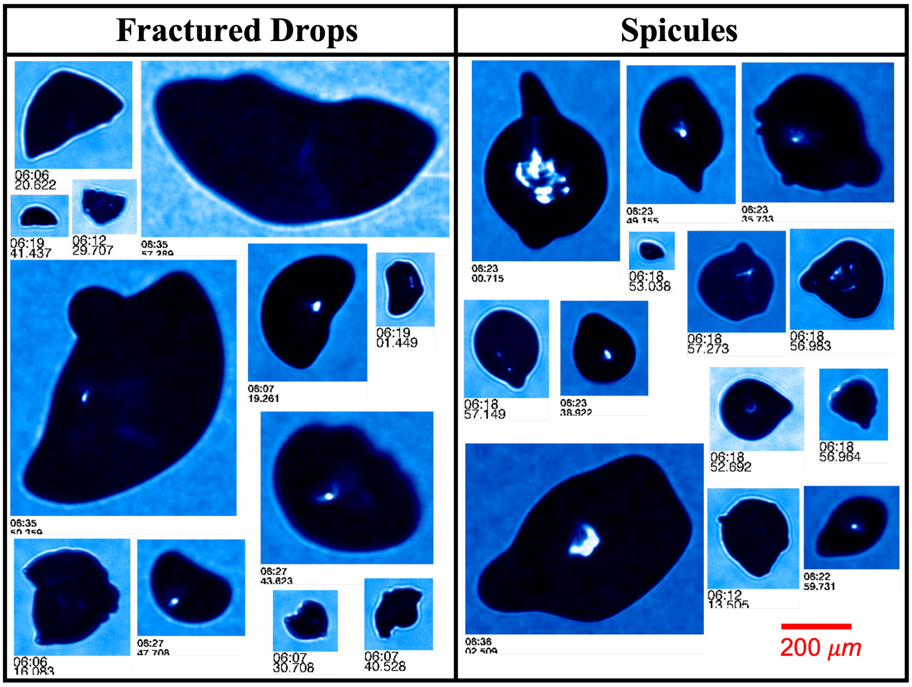


**Figure 5.** Examples of frozen fractured drops (left) and spicules (right) from the 3V-CPI onboard the NASA P3-B and SPEC Learjet during the 25 September 2019 flight.

the HVPS is used for all sizes exceeding the upper 2D-S size threshold. We note that particle-by-particle separation of ice vs. liquid hydrometeors is not explicitly performed for the CAMP$^2$Ex aircraft cloud-probe datasets used herein such that observed $N_{\mathrm{ice}}$ is not available. Instead, we present simulated size distributions for liquid-only, ice-only, and combined species and infer the contribution of FFD based on PSD structure. A full description of the observed case studied here (25 September 2019) is provided in Part I. Briefly, the in situ sampling by both aircraft targeted growing turrets of moderate-to-strong congestus (measuring vertical wind speeds up to 20 m s$^{-1}$) that reached CTTs down to -15 °C. Examples of frozen fractured drops and spicules, indicative of the FFD mechanism and complementary to images shown by Keinert et al. (2020b), are demonstrated in Fig. 5.

## 4 Results

### 4.1 Simulated Cloud-System Evolution

Simulated cloud-system evolution is demonstrated via time-height series of domain-maximum vertical velocity ($w$), domain-mean liquid water content (LWC), and domain-mean ice water content (IWC) for the BIN_CNTL and BULK_CNTL simulations (Fig. 6). Cloud-top heights (CTHs) increase from ≈2 km to a maximum of 8–9 km during hrs 8–9. Domain-averaged

https://doi.org/10.5194/egusphere-2026-4713
Preprint. Discussion started: 21 August 2026


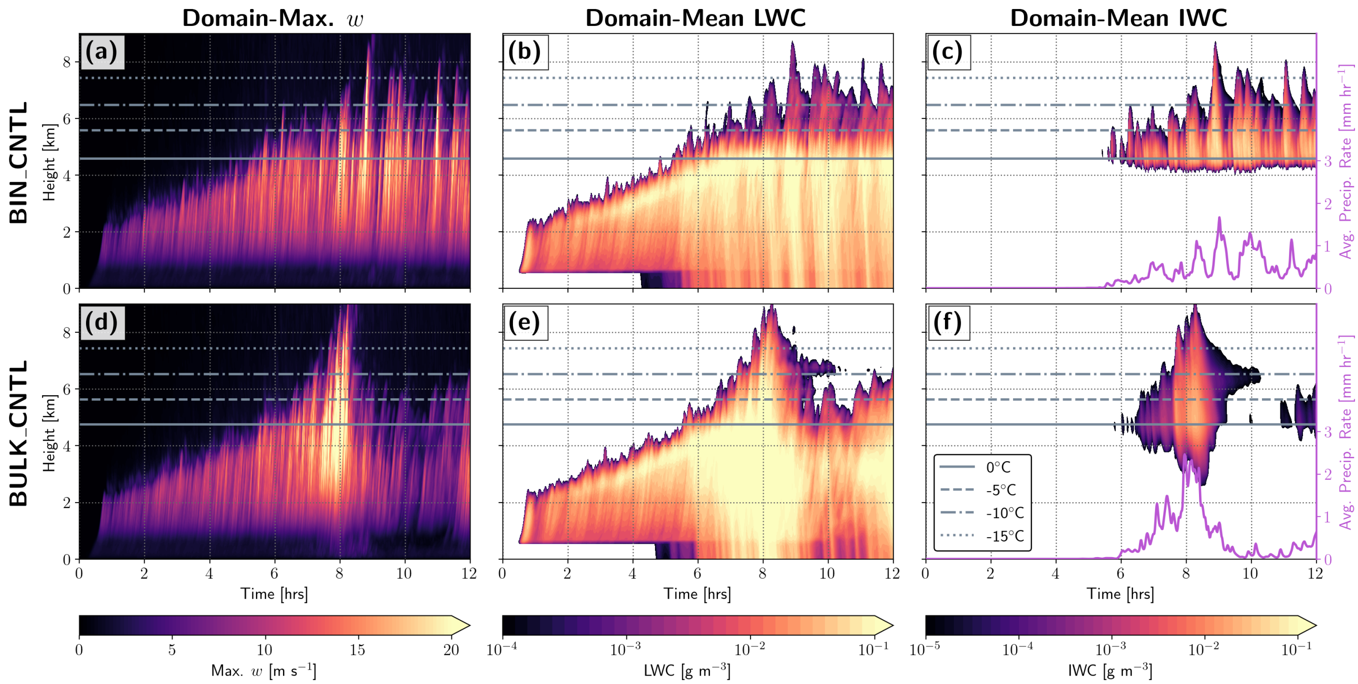


**Figure 6.** Time-height series of (a,d) domain-maximum vertical velocity ($w$), (b,e) domain-average liquid water content (LWC), and (c,f) domain-average ice water content (IWC) for (a)-(c) BIN_CNTL and (d)-(f) BULK_CNTL. Horizontal lines indicate 0 – -15 °C levels in increments of 5 °C. Purple lines (twin y-axes in c,f) show the time series of domain-average precipitation rate.

precipitation rates accelerate after ≈6 hrs, commensurate with ice initiation (Fig. 6c,f). Upon first ice formation, the bin scheme produces steady pulses of enhanced ice condensate coincident with active updrafts (Fig. 6a,c), transiting the mixed-phase region with CTTs down to $\approx -20$ °C. The bulk scheme evolves differently, where convective intensity maximizes at ≈9 hrs, with substantial CTH development after ice onset followed by system weakening during the final 3 hrs (Fig. 6d-f). Domain-mean IWC in the bulk scheme (the sum of cloud ice, fluffy ice, and dense ice) extends to 2 km below the 0 °C isotherm, indicative of precipitating dense ice, while the bin scheme rarely produces substantial IWC at temperatures warmer than 0 °C. The bulk scheme also produces colder CTTs (minimum $\approx -25$ °C). While not the focus of this study, these evolution differences reflect dynamical-microphysical feedbacks resulting from structurally distinct microphysics schemes.

### 4.2 Impacts of SIP

The effects of SIP are demonstrated with time-height series of domain mass-weighted $N_{\mathrm{ice}}$ (Fig. 7). Despite differing evolutions, both the bin and bulk schemes produce primary ice concentrations that maximize between $\approx 10^{-1}$ and 1 L$^{-1}$ (Fig. 7a,d,g). Including SIP via the baseline FFD process in either scheme introduces only very minor (< 1 order of magnitude) $N_{\mathrm{ice}}$ enhancements (Fig. 7b,e,h). The SIP_10X simulations enhance $N_{\mathrm{ice}}$, but with notable differences between the schemes. In BIN_SIP_10X, $N_{\mathrm{ice}}$ reaches maximum values of ≈10 L$^{-1}$ (Fig. 7c). In BULK_SIP_10X, $N_{\mathrm{total\ ice}}$ (the sum of

https://doi.org/10.5194/egusphere-2026-4713
Preprint. Discussion started: 21 August 2026


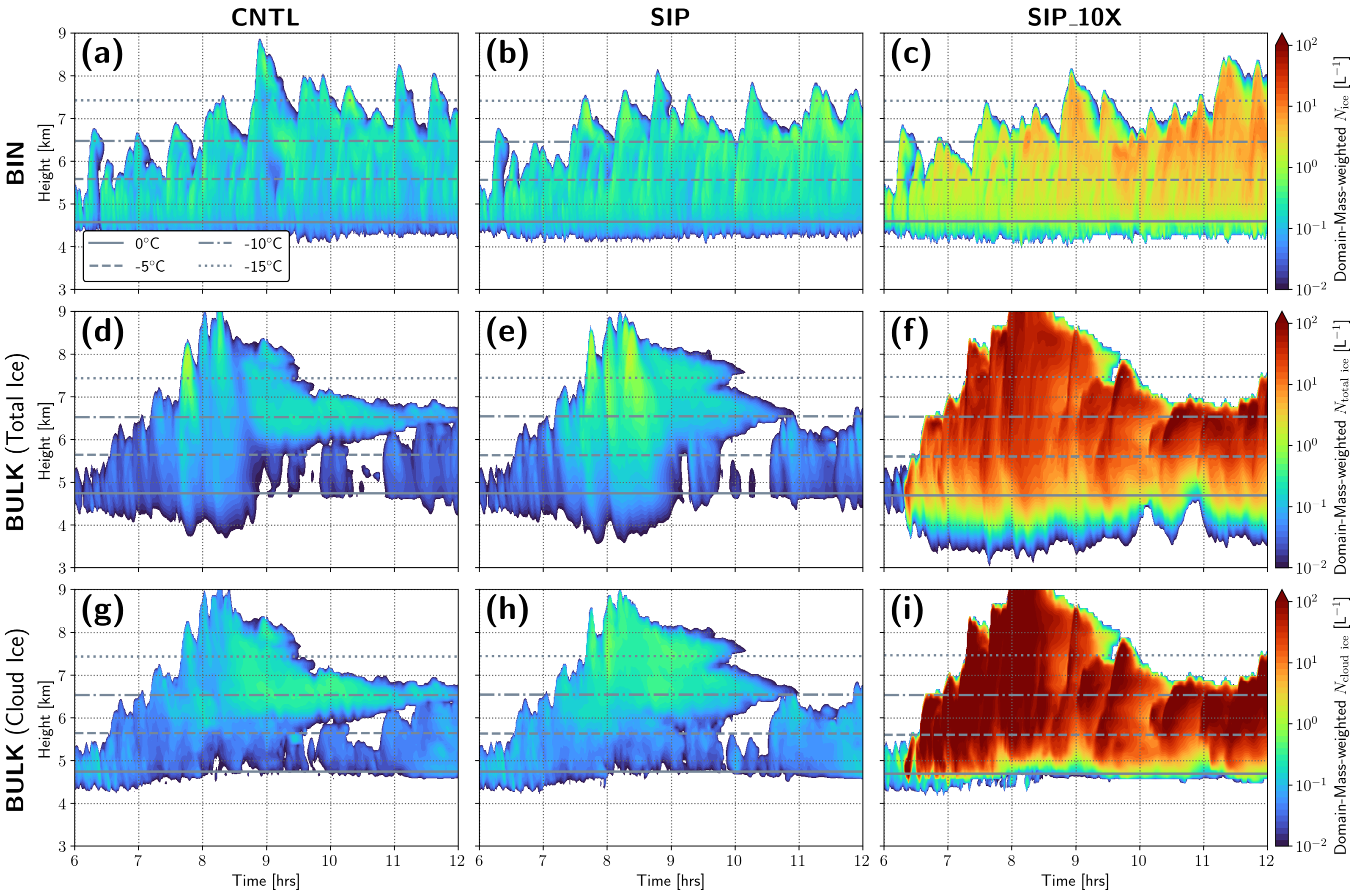


**Figure 7.** Time-height series of ice condensate mass-weighted domain-mean ice number concentration for (a)-(c) the bin scheme ($N_{\mathrm{ice}}$), (d)-(e) the bulk scheme's total ice number concentration ($N_{\mathrm{total\ ice}}$; the sum of all three ice species), and (g)-(i) the bulk scheme's cloud ice species' ice number concentration only ($N_{\mathrm{cloud\ ice}}$) for the relative (a,d,g) CNTL simulations, (b,e,h) SIP simulations, and (c,f,i) SIP_10X simulations.

https://doi.org/10.5194/egusphere-2026-4713
Preprint. Discussion started: 21 August 2026


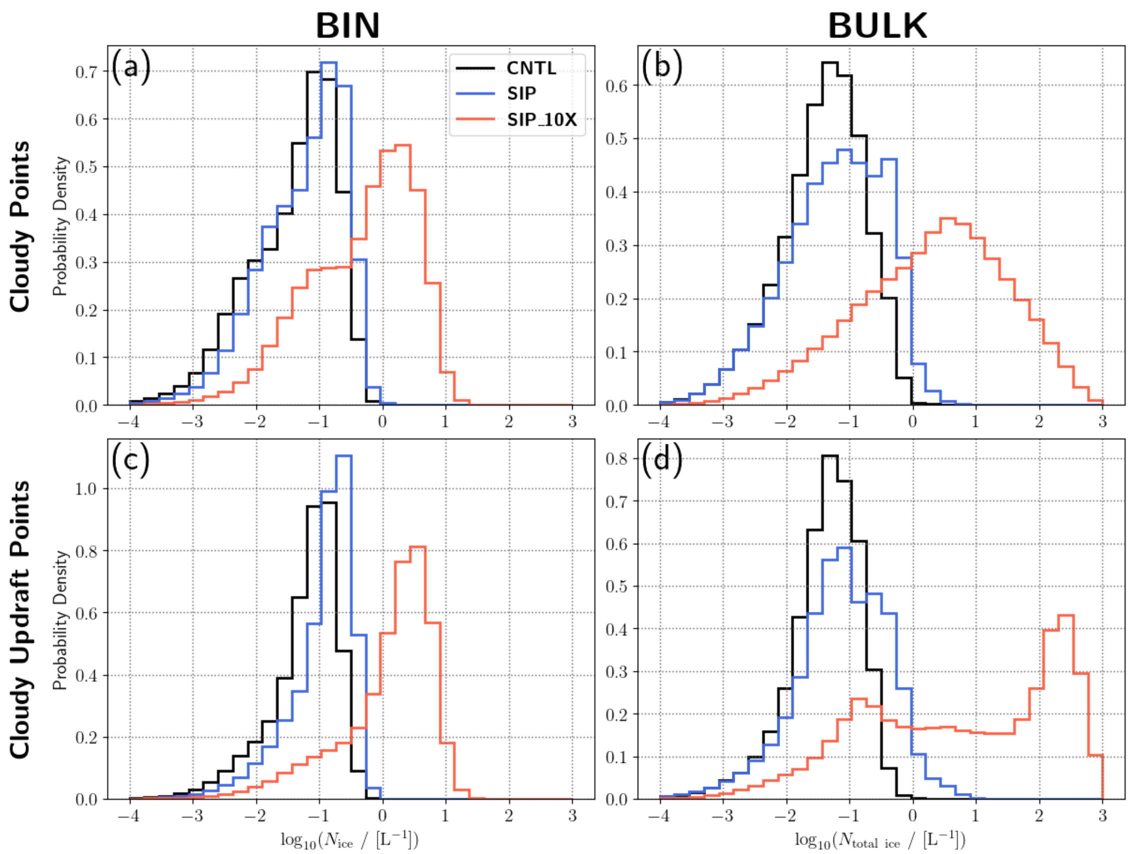


**Figure 8.** Probability density functions (PDFs) of (a,b) bin-scheme ice number concentration ($N_{\mathrm{ice}}$) and (b,d) bulk-scheme total ice number concentration ($N_{\mathrm{total\ ice}}$) for (a,b) cloudy grid points only and (c,d) cloudy updraft grid points. Only grid points with temperatures colder than 0 °C are included.

all ice species) occasionally exceeds 100 L$^{-1}$ (Fig. 7f) while $N_{\mathrm{cloud\ ice}}$ (cloud ice species only—the destination for ice splinters) produces maxima approaching $10^3$ L$^{-1}$ (Fig. 7i). The difference between the $N_{\mathrm{total\ ice}}$ and $N_{\mathrm{cloud\ ice}}$ maxima is due to the mass-weighting, where cloud ice has the highest number concentrations but lowest total mass of the three species.

These characteristics are further illustrated via probability density functions (PDFs; Fig. 8) of $N_{\mathrm{ice}}$ for sub-0°C cloudy grid points (ice mass mixing ratios, $q_{\mathrm{ice}}$, exceeding $10^{-3}$ g kg$^{-1}$) and cloudy updraft grid points ($q_{\mathrm{ice}} > 10^{-3}$ g kg$^{-1}$, $w > 1$ m s$^{-1}$). For primary ice formation (i.e., CNTL simulations), distributions peak at $\approx 10^{-1}$ L$^{-1}$ for both schemes, with only a slight shift to higher concentrations upon including the baseline SIP parameterization (cf. black and blue lines). For cloudy grid points, the SIP_10X simulations produce distribution modes between 1 and 10 L$^{-1}$. However, BULK_SIP_10X exhibits a long tail approaching $10^3$ L$^{-1}$. Narrowing sampling to include only cloudy updraft grid points reveals a bimodal structure in BULK_SIP_10X (Fig. 8d), reflecting a primary-ice mode ($\approx 10^{-1}$ L$^{-1}$) and a secondary-ice mode peaking between $10^2$ and $10^3$ L$^{-1}$, consistent with the time-height series in Fig. 7i.

https://doi.org/10.5194/egusphere-2026-4713
Preprint. Discussion started: 21 August 2026


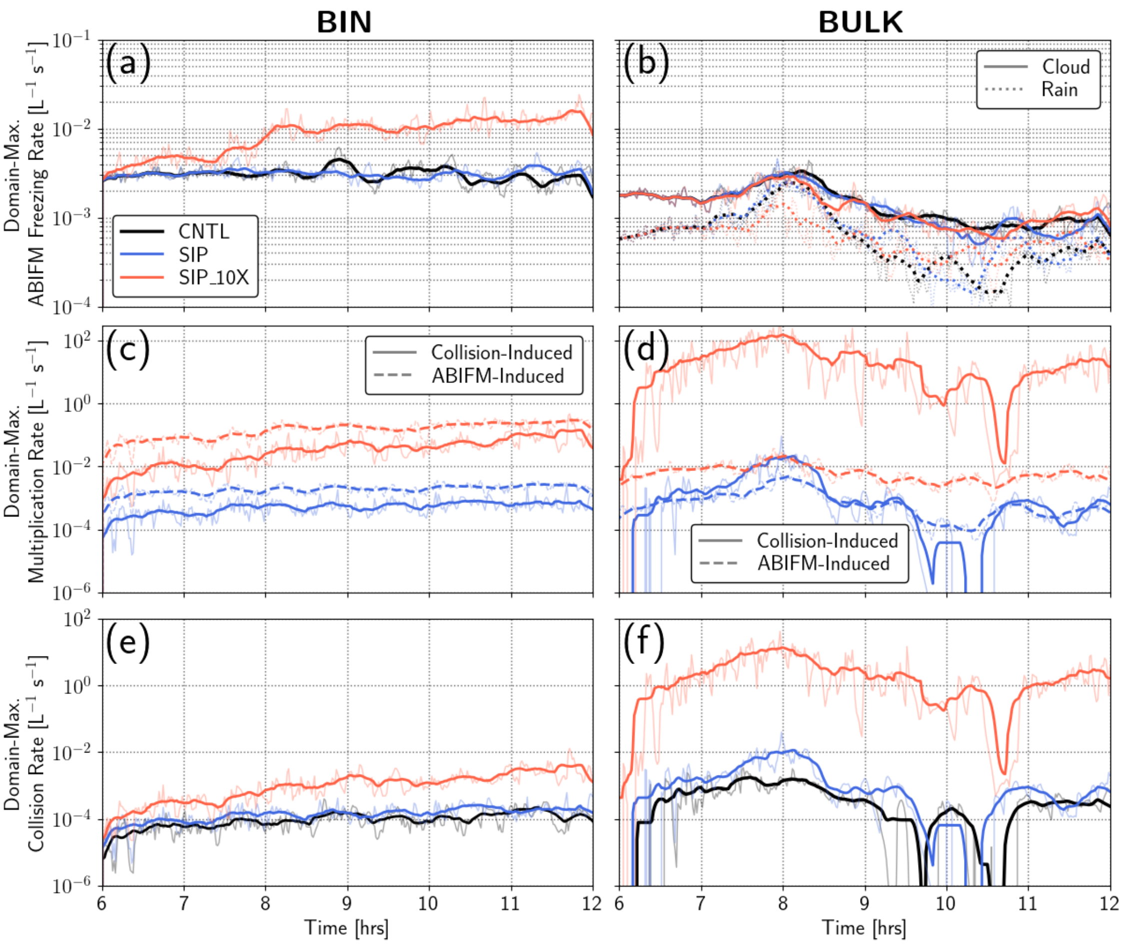


**Figure 9.** Time series of domain-maximum (a,b) ABIFM (primary) freezing rate, (c,d) multiplication rate, and (e,f) collision rate for bin scheme simulations (left column) and bulk scheme simulations (right column). Thin transparent lines are native 1-minute output while thick lines show a 20-minute running mean. Note that panels (c) and (d) separate ABIFM-induced and collision-induced multiplication rates by line style and panel (b) separates primary freezing rates by the cloud and rain species.

https://doi.org/10.5194/egusphere-2026-4713
Preprint. Discussion started: 21 August 2026


Figures 7 and 8 demonstrate two key findings: (1) the baseline SIP parameterization induces only very little $N_{\mathrm{ice}}$ enhancement relative to the CNTL simulations, and a 10× multiplier is required to yield substantial effects and (2) the 10× multiplier is more impactful in the bulk scheme than the bin scheme. The first finding is discussed in detail in Section 5, but briefly reflects a combination of uncertainty in the number of fragments produced per freezing event (see Section 2) and possibly that FFD is not a dominant multiplication mechanism in the case studied here. Nonetheless, given the uncertainty in splinter production magnitudes, the 10× multiplier is considered a tuning parameter, while the parameterization structure retains valuable temperature and size dependencies. Hereafter, we focus on the 10× simulations to more robustly explore the impacts of SIP.

To understand these differences, we examine domain-maximum time series of ice production (primary and secondary) and collision rates (Fig. 9). The primary (ABIFM) freezing rate is similar in magnitude between the bulk and bin schemes (Fig. 9a,b) for the CNTL and SIP simulations. However, in the bin scheme, the primary freezing rate is notably enhanced in BIN_SIP_10X, suggesting a potential feedback between PIP and SIP that is explored in the next section. The bulk scheme shows no such feedback, with primary ice formation rates remaining similar among all simulations. Fig. 9b also shows that PIP in the bulk scheme is dominated by freezing of cloud droplets rather than rain drops (cf. solid and dashed lines).

The domain-maximum multiplication rate, separated into ABIFM-induced and collision-induced (Fig. 9c,d), shows that SIP in the bin scheme occurs primarily due to ABIFM-induced as opposed to collision-induced freezing. Domain-maximum multiplication rates for BULK_SIP are similar between collision- and ABIFM-induced freezing. However, collision-induced freezing rates in BULK_SIP_10X are larger than ABIFM-induced rates by up to four orders of magnitude (Fig. 9d). This is reflected in the domain-maximum collision rates (Fig. 9e,f), where the collision-induced multiplication rates in the bulk scheme largely mirror the domain-maximum collision rates themselves. In the bin scheme, BIN_SIP_10X shows enhanced domain-maximum collision rates relative to the other two simulations, but remains many orders of magnitude smaller than for BULK_SIP_10X.

Figure 9 thus indicates that differences in gross ice multiplication rates between the bin and bulk schemes stem largely from enhanced rain–cloud ice collisions in the bulk scheme. We speculate that these differences are rooted in how each scheme handles newly produced splinters. In the bin scheme, splinters are placed into the smallest size bin, where their collision cross-sections with rain drops are near zero, so shattering-induced feedbacks are self-limiting. In the bulk scheme, splinters augment the number and mass moments of the cloud ice population, but collision rates continue to be evaluated for the mean properties of the full distribution, which is dominated by pre-existing, larger crystals. New splinters thus effectively inherit the collision efficiency of the ambient ice, producing a cascading amplification of collision-induced SIP that is absent in the bin scheme's more explicit, size-resolved treatment. The differences between the dominant freezing mechanisms in each scheme (immersion nucleation vs. collision-induced) and their subsequent splintering behavior warrant further investigation.

### 4.3 Feedbacks between Primary and Secondary Ice Formation

As shown in Fig. 9a, domain-maximum primary freezing rates are larger in BIN_SIP_10X than in BIN_CNTL, suggesting a feedback whereby SIP enhances primary ice formation that is specific to the bin scheme's structure. To investigate this, we compare PDFs of ABIFM-relevant drop properties computed for supercooled drops (Fig. 10).

https://doi.org/10.5194/egusphere-2026-4713
Preprint. Discussion started: 21 August 2026


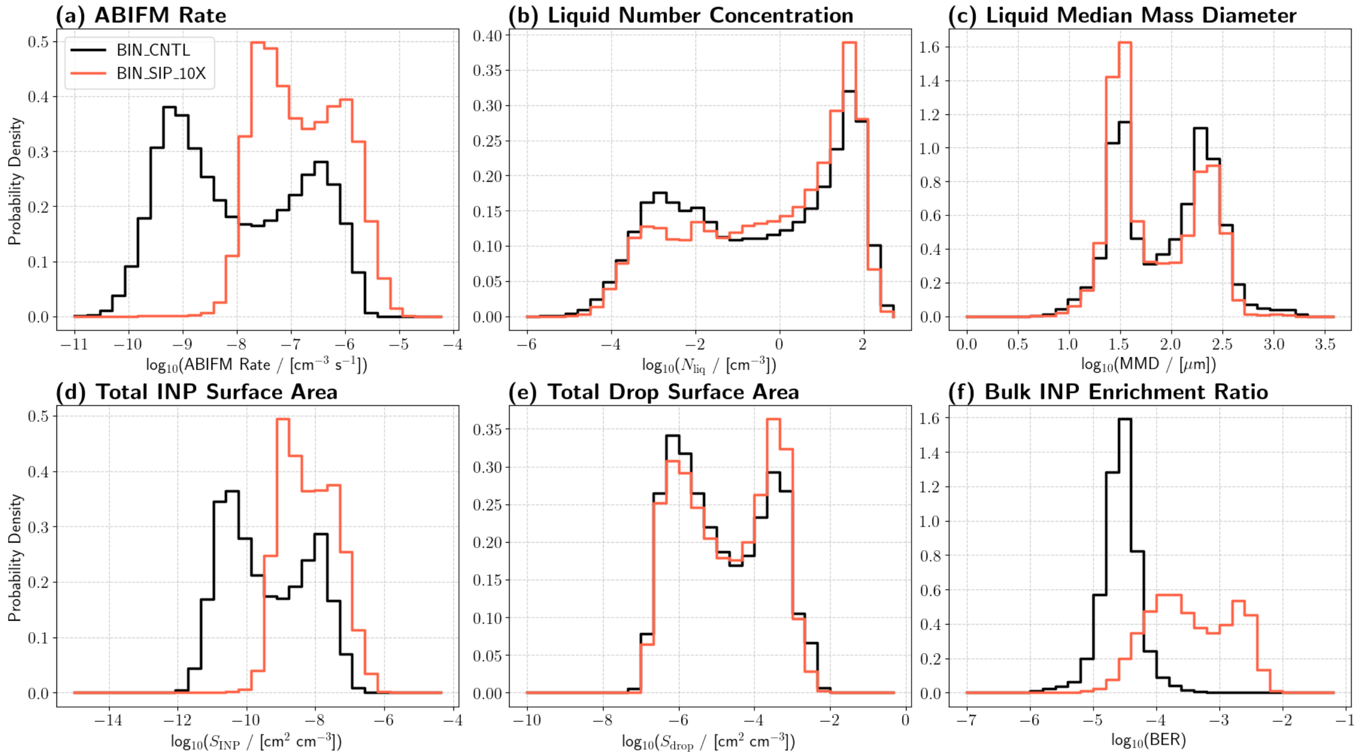


**Figure 10.** Probability density functions for the BIN_CNTL and BIN_SIP_10X simulations for all grid points with liquid mass mixing ratios exceeding $10^{-3}$ g kg$^{-1}$ at temperatures colder than 0°C for (a) ABIFM freezing rate, (b) liquid number concentration ($N_{\text{liq}}$), (c) liquid median mass diameter (MMD), (d) total ice nucleating particle (INP) surface area ($S_{\text{INP}}$), (e) total drop surface area ($S_{\text{drop}}$), and (f) the bulk INP enrichment ratio (BER, the ratio of $S_{\text{INP}}$ to $S_{\text{drop}}$). All variables are $\log_{10}$ transformed prior to binning.

The ABIFM freezing rate (Eq. A6) is the product of $J_{\text{het}}$ (cm$^{-2}$ s$^{-1}$) and the total INP surface area per grid point ($S_{\text{INP}}$; cm$^2$ cm$^{-3}$), where $S_{\text{INP}}$ is the sum, over all bins, of the product of average surface area per drop ($\bar{s}_j$; cm$^2$) and liquid number concentration ($N_{\text{liq},j}$; cm$^{-3}$) in bin $j$. Since $J_{\text{het}}$ depends only on temperature and its distributions are nearly identical between BIN_CNTL and BIN_SIP_10X (not shown), differences in the ABIFM rate between the two simulations stem largely from differences in $S_{\text{INP}}$.

The ABIFM freezing rate is bimodal in both simulations and shifted to larger values in BIN_SIP_10X (Fig. 10a), consistent with the domain-maximum rates in Fig. 9a. The bimodality reflects contributions from cloud droplets and rain drops, evident in the PDFs of $N_{\text{liq}}$ and liquid median mass diameter (MMD; Fig. 10b,c), where MMD is defined as the diameter at which half of the total mass of the DSD resides and is used as a representative size of the DSD. These distributions show a cloud droplet mode with MMDs ≈30 $\mu$m and $N_{\text{liq}}$ approaching 100 cm$^{-3}$ and a drizzle/rain mode with MMDs ≈200–300 $\mu$m and $N_{\text{liq}}$ ≈$10^{-3}$ cm$^{-3}$. BIN_SIP_10X produces more cloud droplets than BIN_CNTL (Fig. 10b), suggesting that SIP reduces the rain drop population by introducing additional freezing opportunities, leaving fewer drops available as coalescence targets.

https://doi.org/10.5194/egusphere-2026-4713
Preprint. Discussion started: 21 August 2026


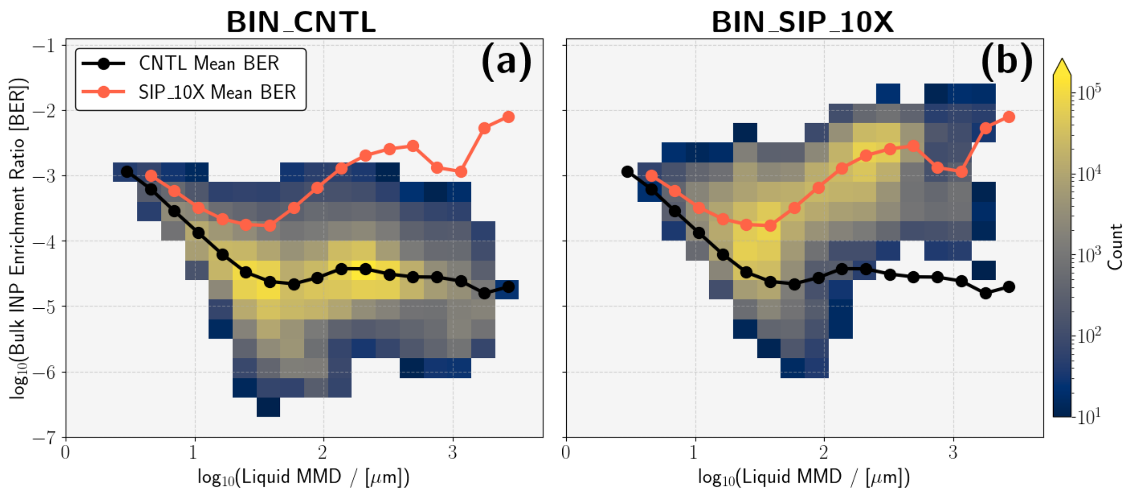


**Figure 11.** Joint histograms of median mass diameter (MMD, abscissa) and bulk ice nucleating particle (INP) enrichment ratio (BER) for (a) BIN_CNTL and (b) BIN_SIP_10X for all cloudy grid points ($q_l > 10^{-3}$ g kg$^{-3}$) and temperatures colder than 0 °C. Lines with circle markers show the mean BER for a given liquid MMD bin.

The $S_{\mathrm{INP}}$ distribution largely mirrors the ABIFM rate (Fig. 10d), as expected given similar $J_{\mathrm{het}}$ distributions. We define the bulk INP enrichment ratio (BER) as the ratio of $S_{\mathrm{INP}}$ to total drop surface area ($S_{\mathrm{drop}}$; cm$^2$ cm$^{-3}$), with distributions of $S_{\mathrm{drop}}$ and BER shown in Fig. 10e,f. The bimodality of $S_{\mathrm{drop}}$ reflects the two size modes, with BIN_SIP_10X producing a slightly larger cloud-mode $S_{\mathrm{drop}}$ than BIN_CNTL. Despite this, distribution structural differences in $S_{\mathrm{INP}}$ between the two simulations are larger than those in $S_{\mathrm{drop}}$, resulting in the BER distribution of BIN_SIP_10X being shifted to larger values by several orders of magnitude (Fig. 10f). Notably, BER is unimodal in BIN_CNTL but bimodal in BIN_SIP_10X, which we explore next.

Elevated BER in BIN_SIP_10X raises the question of why supercooled drops are more INP-enriched when SIP is active. We hypothesize two potential mechanisms: (1) SIP-induced glaciation limits condensational growth of cloud droplets via preferential diffusional growth of ice crystals (vapor competition), yielding smaller drops with the same INP core mass and thus higher BER; and (2) drops that have grown via collision-coalescence and accumulated substantial INP core mass are recycled. In the latter process, drops initially freeze, melt upon falling through the melting layer, and re-enter the liquid phase as highly enriched drops that more readily freeze upon being re-lofted above the 0°C isotherm. The vapor-competition mechanism would primarily manifest in cloud droplets and the recycling mechanism in rain drops. To distinguish between these, we produce joint histograms of BER and liquid MMD for BIN_CNTL and BIN_SIP_10X (Fig. 11).

Both simulations show two maxima in the joint BER–MMD space, representing the cloud and rain modes. In BIN_CNTL, the largest BER is associated with the smallest MMDs, reflecting freshly nucleated cloud droplets whose INP core mass represents a substantial fraction of their drop surface area. BER decreases with increasing MMD up to the cloud-to-drizzle transition (≈50–100 $\mu$m), indicative of condensational growth prior to substantial collision-coalescence, then increases slightly

https://doi.org/10.5194/egusphere-2026-4713
Preprint. Discussion started: 21 August 2026


for drops larger than 100 $\mu$m as coagulation accumulates INP cores. This boost is modest, consistent with the unimodal BER distribution in BIN_CNTL (Fig. 10f.)

BIN_SIP_10X shows higher BER than BIN_CNTL across all MMDs, with the same qualitative BER–MMD shape offset to higher values. For MMDs smaller than $\approx$30 $\mu$m, an initial interpretation is that vapor competition drives the BER enhancement. However, within the cloud droplet size range, collision-coalescence is negligible and $S_{\mathrm{INP}}$ per drop is set at activation, so condensational growth affects only $S_{\mathrm{drop}}$. If vapor competition were responsible, it would operate through a reduction in $S_{\mathrm{drop}}$, leaving $S_{\mathrm{INP}}$ unchanged. Fig. 10e showed, however, that $S_{\mathrm{drop}}$ is actually larger in BIN_SIP_10X within the cloud mode—opposite to what vapor competition predicts—ruling out this mechanism. Higher BER cannot arise from simply having more drops of the same DSD composition, since both $S_{\mathrm{INP}}$ and $S_{\mathrm{drop}}$ would scale proportionally, leaving BER unchanged. Instead, higher BER at cloud sizes implies a compositional shift toward a larger proportion of high-BER drops—for example, more freshly activated droplets whose INP core mass represents a larger fraction of their drop surface area—though the precise cause cannot be established without additional 3D process-rate diagnostics.

For MMDs larger than $\approx$30 $\mu$m, BER in BIN_SIP_10X increases substantially and peaks near $\approx$300 $\mu$m, demonstrating that rain drops are substantially INP-enriched. Unlike the cloud mode, this signal reflects genuine per-drop INP enrichment through the following proposed, but unexplored, pathway: drops that have grown by collision-coalescence accumulate INP core mass, freeze, melt, and re-enter the liquid phase with elevated $\bar{s}_j$ per drop, directly increasing $S_{\mathrm{INP}}$ and thus ABIFM rates. Although this mechanism cannot be confirmed without a Lagrangian microphysics approach, it could plausibly close the PIP–SIP feedback loop. This proposed pathway is consistent with the conceptual model of Korolev et al. (2020, 2024), who hypothesized that recirculation of drops through the melting layer initiates a chain reaction of SIP in tropical mesoscale convective systems via collision-induced freezing and shattering of recycled drops. We acknowledge that the freeze-melt-loft cycle is more readily sustained in organized convective systems where recirculation pathways are well-established (Korolev et al., 2020), and its role in the more isolated congestus regime studied here remains speculative without Lagrangian confirmation. Collectively, these results suggest that enhanced BER in BIN_SIP_10X arises from a compositional shift in the cloud droplet population as well as a genuine per-drop INP enrichment of rain drops via the freeze-melt-loft cycle. Since this feedback does not emerge in the bulk scheme (Fig. 9a,b), we attribute it to the bin scheme's explicit tracking of aerosol core mass across the full size spectrum, a capability absent in the bulk scheme.

### 4.4 Comparison of simulated and observed in situ PSDs

In situ PSDs measured in updrafts at temperature levels spanning 0 to $-15$ °C enable direct observational comparison. Observed PSDs are composited across "cloud passes", which are horizontally contiguous segments with TWC $> 0.1$ g m$^{-3}$, consistent with the definition and framework established in Part I. We use four observed temperature levels: 1 °C, $-7.4$ °C, $-11.1$ °C, and $-14.7$ °C. The $-7.4$ °C and $-14.7$ °C levels each contain two observed cloud passes, providing a measure of observed variability. All cloud passes contained moderate-to-strong updrafts, and a microphysical and dynamical summary is provided in Table 2.

https://doi.org/10.5194/egusphere-2026-4713
Preprint. Discussion started: 21 August 2026


**Table 2.** Thermodynamic, kinematic, and microphysical description of six selected cloud passes used to construct observed composite particle size distributions (PSDs). Cloud passes are defined as contiguous segments with total water content (TWC) > 0.1 g m$^{-3}$ and vertical velocity ($w$). Sample size indicates the total number of PSDs that contribute to a given composite cloud-pass PSD.

| CP | Aircraft | Transect Length [km] | Sample Size | Temp. [°C] | | | $w$ [m s$^{-1}$] | | TWC [g m$^{-3}$] | |
|---|---|---|---|---|---|---|---|---|---|---|
| | | | | Avg. | Min. | Max. | Avg. | Max | Avg. | Max |
| 1 | Learjet | 1.66 | 11 | 1.04 | 0.3 | 2.0 | 4.15 | 9.2 | 0.92 | 1.7 |
| 2 | Learjet | 0.68 | 4 | -7.3 | -7.5 | -6.9 | 1.85 | 3.6 | 0.78 | 1.1 |
| 3 | Learjet | 0.63 | 4 | -7.43 | -7.7 | -7.2 | 1.33 | 4.4 | 0.63 | 0.8 |
| 4 | P3-B | 6.84 | 25 | -11.09 | -12.2 | -9.27 | 4.18 | 18.5 | 0.66* | 2.1* |
| 5 | Learjet | 4.16 | 24 | -14.57 | -16.4 | -12.8 | 9.55 | 20.9 | 1.06 | 2.1 |
| 6 | Learjet | 1.58 | 9 | -14.76 | -15.9 | -12.9 | 3.13 | 16.0 | 1.02 | 1.8 |

*TWC from the P3-B aircraft, which did not have a bulk TWC sensor, is derived by integrating the 2D-S PSD with an assumed mass-size power law.

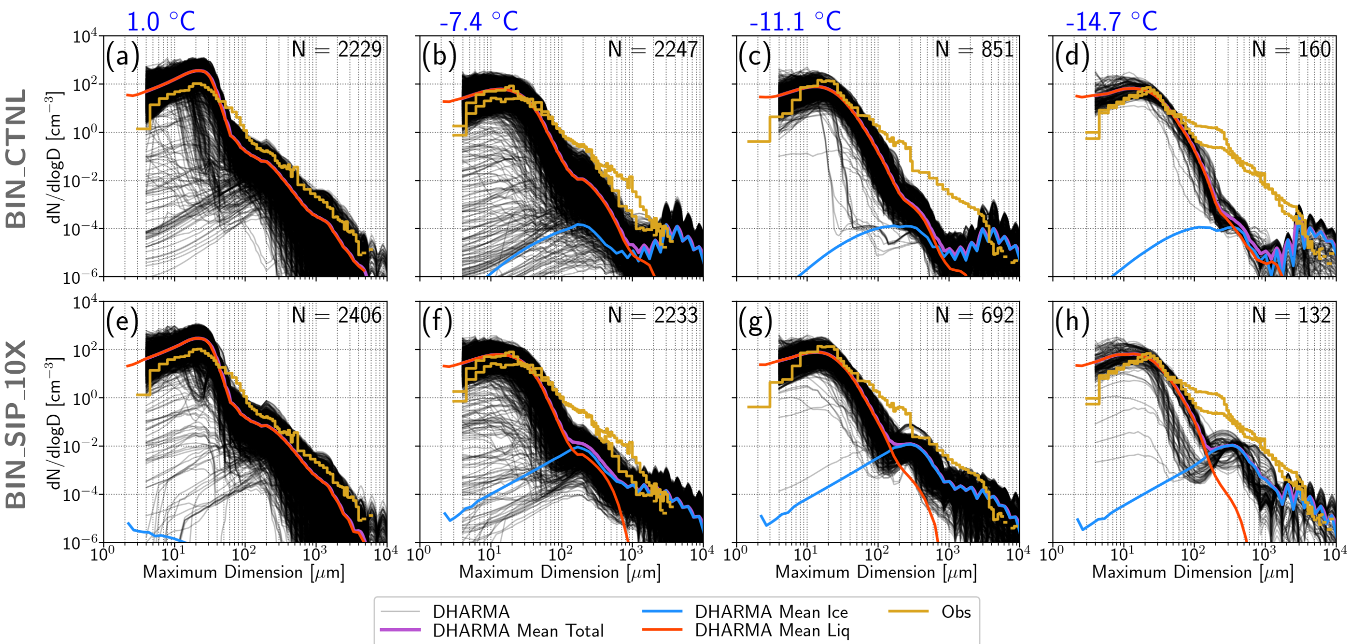


**Figure 12.** Composite particle size distributions (PSDs) for individual simulated cloud passes (transparent black lines) and observed cloud passes (mustard lines) at temperatures of (a,e) 1.0 °C, (b,f) -7.4 °C, (c,g) -11.1 °C, and (d,h) -14.7 °C for BIN_CNTL (top row) and BIN_SIP_10X (bottom row). The BIN_SIP simulation is not shown due to its similarity to BIN_CNTL. The simulated mean liquid PSD and ice PSD are shown in red and blue lines, respectively, with the simulated total PSD (sum of liquid and ice) shown as a purple line. Sample sizes given in the top right of each panel indicate the number of simulated cloud passes. Note that for temperatures of -7.4 °C and -14.7 °C, two observed cloud passes are shown. Opaque black regions indicate substantial overlap of individual simulated PSDs.

https://doi.org/10.5194/egusphere-2026-4713
Preprint. Discussion started: 21 August 2026


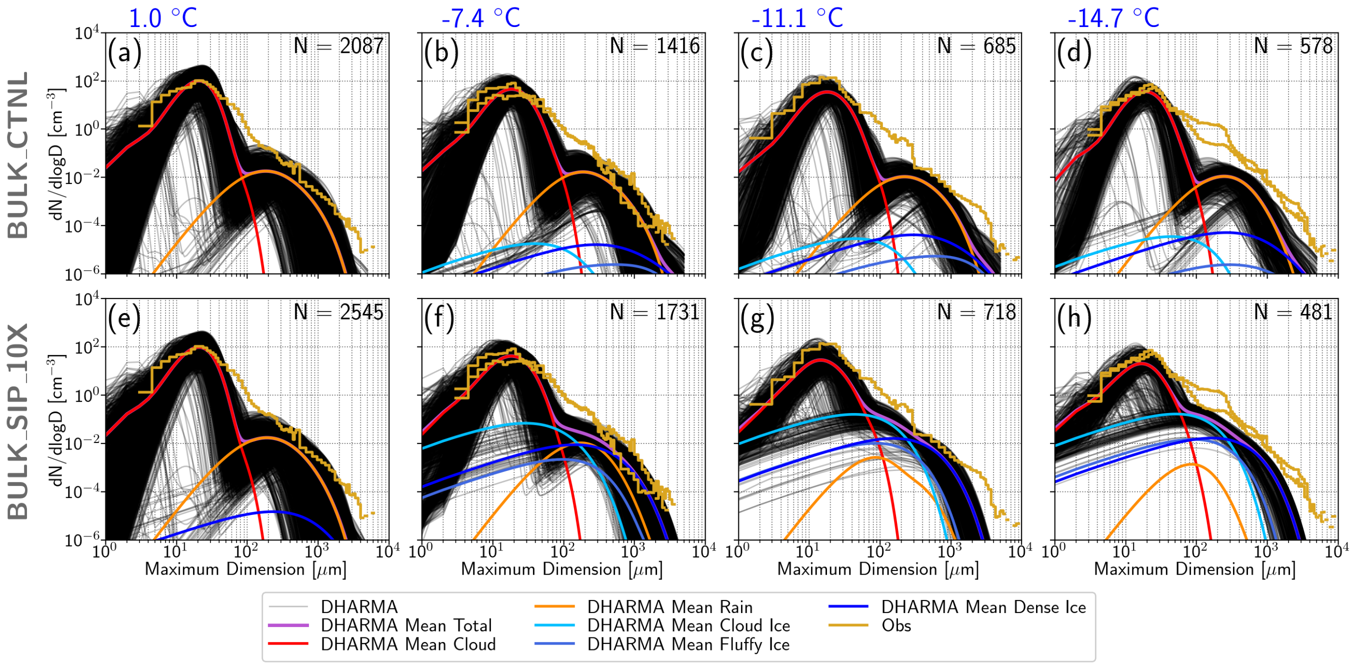


**Figure 13.** As in Fig. 12 but for the bulk scheme. Note that mean lines are shown for the bulk scheme's five species with colors indicated in the legend.

For simulations, cloud passes are constructed at each observed temperature level across the last six hours of the simulations. A single cloud-pass sample is computed by averaging the PSD for each scheme along horizontal segments meeting the TWC requirement, retaining only passes where the average $w$ exceeds 1 m s$^{-1}$. Although observed cloud passes reached much higher vertical velocities (up to 20 m s$^{-1}$ at $-14.7$ °C; Table 2), all simulated updraft passes are retained to assess whether the simulated PSDs can bound the observations. Composite PSDs are computed by summing individual species at each diameter before averaging along the horizontal segment. For the bulk scheme, individual species PSDs are reconstructed from gamma distribution moments.

PSDs at each temperature level for BIN_CNTL and BIN_SIP_10X are shown in Fig. 12. At 1 °C, simulated DSDs are biased toward more cloud droplets and fewer rain drops than observed (Fig. 12a,e), which likely affects PSDs at colder temperatures through insufficient rain drop numbers for freezing. Nonetheless, sub-freezing cloud passes show that primary ice formation (BIN_CNTL) produces a bimodal ice PSD (blue lines) with peaks near ≈200 $\mu$m and 4–5 mm. The smaller mode aligns with a shoulder in the liquid DSD at the same size (e.g., Fig. 12b), while the larger mode reflects dense ice produced from freezing rain drops. Introducing SIP (Fig. 12e–h) increases ice number concentrations in the smaller mode by up to two orders of magnitude and produces a more continuous spectrum to larger sizes. The mean PSDs (purple lines) in BIN_SIP_10X remain up to an order of magnitude below observed concentrations per bin, though individual simulated PSDs approach and at times overlap the observations, with better agreement at $-7.4$ and $-11.1$ °C than at $-14.7$ °C. The simulated mean PSDs

https://doi.org/10.5194/egusphere-2026-4713
Preprint. Discussion started: 21 August 2026


at −11.1 and −14.7 °C show a distinct shoulder near ≈200 $\mu$m that is coincident with an observed PSD shoulder. These comparisons indicate that FFD reduces the 1–2 order-of-magnitude underproduction of concentrations for sizes > ≈200 $\mu$m seen in BIN_CNTL, though a gap with observations remains.

The BULK_CNTL simulation (Fig. 13a–d) produces PSDs at all temperatures dominated by liquid, with rain number concentrations several orders of magnitude larger than all ice species even at −14.7 °C. Including SIP (Fig. 13e–h) substantially depletes rain contributions such that ice becomes the dominant species at all sub-freezing temperatures, with individual cloud-pass PSDs overlapping portions of the observed PSD at most sub-freezing temperatures and concentrations two orders of magnitude larger than in BULK_CNTL. The freezing process affects all ice species: splinters populate the cloud ice category, the remainder of each frozen drop contributes to snow and graupel, and subsequent growth transfers cloud ice into precipitating ice categories. Although the bulk scheme cannot reproduce the large-diameter tail seen in Fig. 12, its capacity for rapid self-amplifying multiplication (Figs. 7–9) allows it to close the gap with observations for sizes > 200 $\mu$m more effectively than the bin scheme.

Overall, simulated PSD comparisons with observations indicate that the tuned FFD mechanism improves the size-resolved representation of hydrometeor populations but is insufficient to fully explain the large observed concentrations at sizes > 200 $\mu$m. This likely reflects both a bias in the simulated liquid DSDs at the 0 °C level and contributions from additional SIP processes not represented here, compounded by uncertainty in the number of splinters produced per freezing event.

## 4.5 Sensitivity of SIP to turbulence-induced collision enhancement

Finally, we explore the role of turbulence-induced collision enhancement in modulating the FFD mechanism in the bin simulations, where it was shown to improve agreement with observed liquid DSDs in Part I. Note that turbulence enhancement is not included in the bulk scheme. Sensitivity to turbulent enhancement may arise through two pathways: modulating the liquid DSD before entering the mixed-phase region, or modulating collisions between liquid drops and ice within it. Turbulent enhancement is included by default in all bin simulations presented thus far, with additional simulations neglecting it denoted by the "NOTURB" suffix. Fig. 14 shows the time-height evolution of domain-mean mass-weighted $N_{\mathrm{ice}}$ for BIN_CNTL, BIN_SIP_10X, BIN_CNTL_NOTURB, and BIN_SIP_10X_NOTURB. Comparing BIN_CNTL and BIN_CNTL_NOTURB (Fig. 14a,c) shows that neglecting turbulent enhancement yields larger ice number concentrations. This is explained by the liquid DSD reaching the 0 °C level, where PDFs of liquid MMD (Fig. 15b) show that neglecting turbulent enhancement produces many more drops in the cloud mode, reflecting insufficient collision-coalescence before reaching the freezing level. Including SIP yields only modest increases in $N_{\mathrm{ice}}$ (Figs. 14d and 15a), with the modal concentration shifted by only half an order of magnitude (Fig. 16a).

Simulated cloud-pass PSDs for the NOTURB simulations show that even at 1 °C, the liquid DSDs exhibit a substantial deficit in drop numbers between ≈40 $\mu$m and 2 mm (Fig. 16; cf. solid red and dashed pink lines, where the latter represents simulations with turbulent enhancement). Upon reaching the mixed-phase region, this deficit results in ice PSDs that cannot approach observed concentrations for sizes > 200 $\mu$m even when SIP is included. Furthermore, the limited ice production inhibits system growth such that very few updrafts reach the −14.7 °C level (Fig. 16d,h). Overall, these results indicate

https://doi.org/10.5194/egusphere-2026-4713
Preprint. Discussion started: 21 August 2026


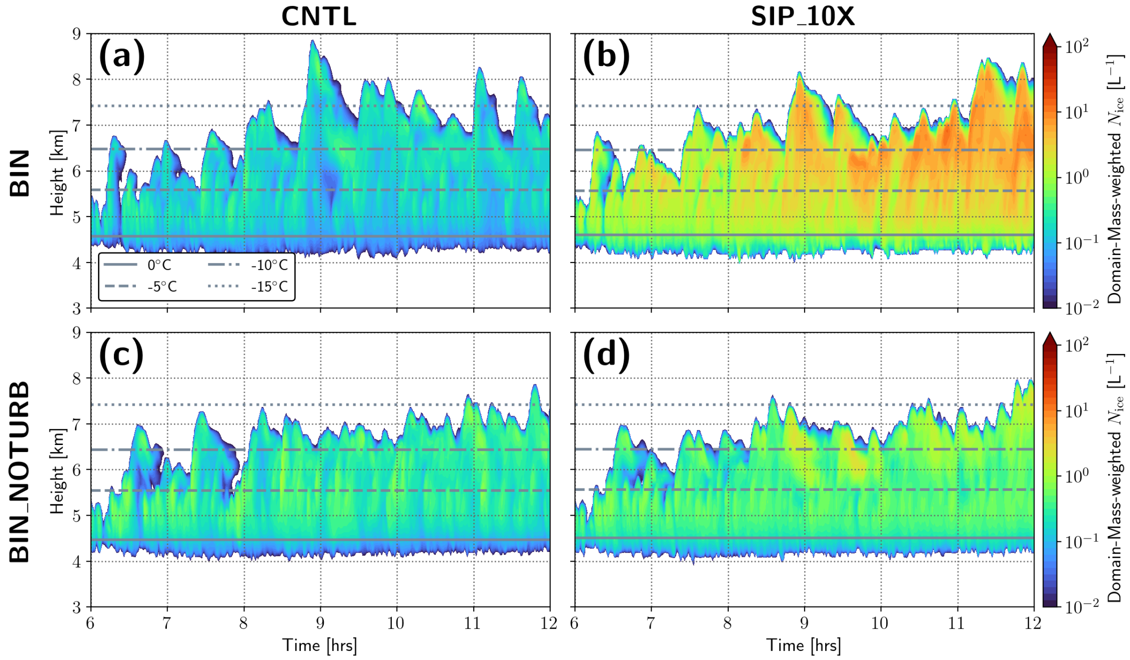


**Figure 14.** Time-height series of domain-mean condensate mass-weighted ice number concentration ($N_{\mathrm{ice}}$) for (a) BIN_CNTL, (b) SIP_10X, (c) BIN_CNTL_NOTURB, and (d) BIN_SIP_10X_NOTURB.

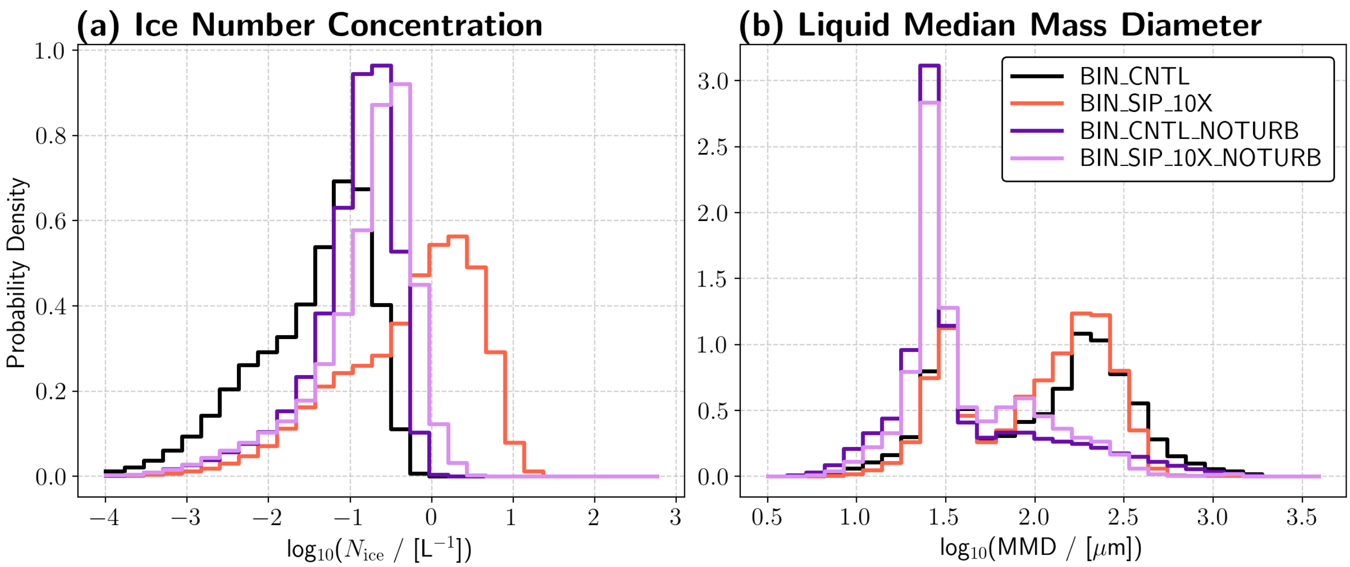


**Figure 15.** Probability density functions (PDFs) of (a) ice number concentration $N_{\mathrm{ice}}$ and (b) liquid median mass diameter (MMD) for BIN_CNTL and BIN_SIP_10X simulations (black and red lines, respectively), and BIN_CNTL_NOTURB and BIN_SIP_10X_NOTURB (dark purple and light purple lines, respectively).

https://doi.org/10.5194/egusphere-2026-4713
Preprint. Discussion started: 21 August 2026


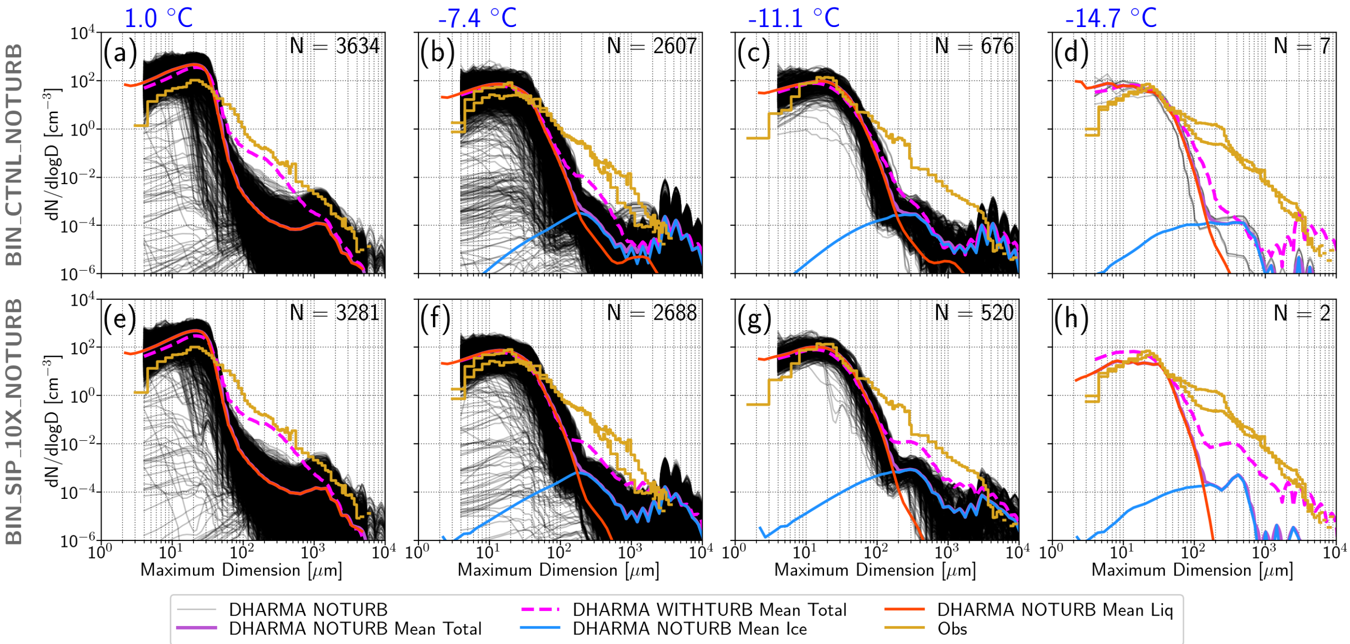


**Figure 16.** As in Fig. 12 but for the BIN_CNTL_NOTURB simulation (top row) and the BIN_SIP_10X_NOTURB simulation (bottom row). Thick dashed pink lines (denoted "WITHTURB") represent the total mean composite PSD from respective simulations that include turbulence-induced collision enhancement, as was shown in Fig. 12.

that the primary influence of turbulence-induced collision enhancement on SIP is through preconditioning of the liquid DSD before it reaches sub-0 °C temperatures, with its role in modulating ice-liquid collisions within the mixed-phase region being secondary. This finding supports Lawson et al. (2022), who presented in situ observations of PSDs in cumulus congestus across multiple geographic regions showing evidence of FFD through imagery of frozen spicules and fractured drops (e.g., Fig. 5). Those observations were coincident with liquid DSDs that broadened with increasing altitude, indicative of turbulence-induced collision enhancement that is essential not only for producing realistic liquid DSD structure (Chandrakar et al., 2024; Stanford et al., 2025), but also for the downstream ice PSDs that result from FFD and other SIP processes dependent on supercooled drops.

## 5 Discussion

### 5.1 Primary ice formation as a rate-limiting constraint on drop-shattering

The negligible contribution of baseline FFD in our simulations may reflect a compound physical bottleneck rather than a deficiency in the per-drop splinter parameterization itself. The KIT formula yields ≈ 1-2 splinters per frozen drizzle drop (300 $\mu$m) between temperatures of 0 and -15 °C, consistent with the drizzle-number-dominated DSDs beyond the cloud mode and

https://doi.org/10.5194/egusphere-2026-4713
Preprint. Discussion started: 21 August 2026


characteristic of CAMP$^2$Ex congestus. A fundamental limitation may be rather the number of drops that actually freeze. Modal ABIFM-driven primary freezing rates in our simulations are $\sim 10^{-7.5}$–$10^{-6}$ cm$^{-3}$ s$^{-1}$, constraining peak splinter production to $\lesssim 10^{-3}$ L$^{-1}$ s$^{-1}$ even in the most active updraft columns. This is compounded by two structural limitations of the present implementation: only immersion-mode nucleation is considered, and the collisional SIP pathway requires pre-existing ice to initiate—creating a self-limiting cycle in which sparse primary ice suppresses the collision-induced freezing that would otherwise feed drop-shattering. Because aerosol concentrations and organic INP fractions in our simulations are observationally constrained from CAMP2Ex, these low primary freezing rates are physically realistic rather than conservative assumptions. The SIP_10X experiments probe uncertainty in the per-drop yield of the KIT formula—which is substantial, reflecting the limited laboratory datasets underlying splinter number production—but does not address uncertainty in the primary freezing rate itself.

### 5.2 Other SIP mechanisms and a persistent primary ice constraint

Observational evidence from this case does not support an active Hallett-Mossop process. Two updraft cloud passes at similar temperatures (≈-7.3 and -7.4 °C) tell a contrasting story: CP 2 (Table 2), whose cloud top reached only ≈-8.5 °C, showed no evidence of ice production in 3V-CPI imagery, while CP 3, whose turret reached ≈-15 °C, showed clear evidence of spicules and fractured drops. This contrast suggests that ice production in this case was driven by FFD in deeper turrets rather than rime-splintering, and that the temperature range nominally associated with Hallett-Mossop was not productive here. This is consistent with Korolev et al. (2024), who found that SIP in tropical mesoscale convective systems correlated with the locations of the coldest cloud tops, suggesting that turret depth is a primary modulator of SIP activity.

Nonetheless, our Hallett-Mossop sensitivity experiments (Appendix C) are instructive. Rime splintering has been invoked as a potentially productive SIP mechanism in tropical maritime cumuli (e.g., Lasher-Trapp et al., 2016), and our Hallett-Mossop simulations produce $N_{\rm ice}$ comparable to BIN_SIP_10X (Fig. C1). Rather than resolving mechanism attribution, this equivalence reinforces the same primary-ice-rate bottleneck identified for FFD—both mechanisms are ultimately constrained by the availability of primary ice to initiate secondary events. This picture is further complicated by recent laboratory studies questioning whether rime splintering occurs as robustly as classically reported (e.g., Seidel et al., 2023), adding further uncertainty to mechanism attribution in field observations more broadly (Korolev et al., 2020). Ice-ice collisional breakup (e.g., Vardiman, 1978; Takahashi et al., 1995; Phillips et al., 2017b, a; Sotiropoulou et al., 2021) represents a third candidate mechanism for which modeling evidence is compelling (e.g., Huang et al., 2022; Qu et al., 2020, 2022, 2025), but which is not evaluated here due to necessary limited focus. Indeed, this mechanism may be particularly consequential at colder temperatures where ice concentrations are substantially higher than in the mixed-phase layer examined here (e.g., Qu et al., 2020), and evaluating it in the same LES framework is a natural high-priority next step.

### 5.3 Parameterization limitations and guidance for future use

We note that the polynomial fit for $n_{\rm PRE}(T)$ (Eq. 1) yields non-zero values approaching 0 °C, outside the observational range of the laboratory experiments ($\leq -5$ °C). In principle, large drops recycled through the melting layer could freeze near 0 °C

https://doi.org/10.5194/egusphere-2026-4713
Preprint. Discussion started: 21 August 2026


and activate the parameterization in this extrapolated range. However, ABIFM freezing rates are negligible near 0 °C even for INP-enriched drops, and collision-induced freezing is self-limiting in this temperature range given the sparse pre-existing ice. We therefore expect any spurious splinter production from this extrapolation to be negligible relative to the bulk SIP signal in the simulations presented here.

Nonetheless, users of the parameterization should exercise caution in cloud regimes where large drizzle or rain drops could freeze at temperatures close to 0 °C, such as in the vicinity of the melting layer in organized convective systems (Korolev et al., 2020, 2024) or in rain refreezing events (Pfeifer et al., 2025). In such cases, the polynomial extrapolation of $n_{\mathrm{PRE}}(T)$ toward 0 °C may introduce non-negligible splinter production outside the observationally constrained range of the parameterization. A future refinement could introduce a linear ramp of $n_{\mathrm{PRE}}$ to zero as temperature approaches 0 °C, though the slope of such a ramp would need to be defined carefully to avoid underestimating splinter production from drops recycled through the melting layer, for which non-zero production near 0 °C may be physically justified.

### 5.4 Future directions: laboratory constraints, field attribution, and parameterization intercomparison

Narrowing the uncertainties identified here requires progress on several fronts. On the laboratory side, immersion freezing parameterizations are typically associated with uncertainties of one to two orders of magnitude, though the uncertainty can increase due to the challenge of determining the INP surface area on the nanoscale (McCluskey et al., 2018; Knopf et al., 2020; Knopf and Alpert, 2023; Knopf, 2024; Alpert et al., 2022). Furthermore, there is uncertainty associated with the implemented parameterization approach (e.g. Knopf et al., 2021, 2023a; Sun et al., 2026). The potential contribution of contact-mode nucleation to primary freezing rates in convective updrafts is also not well-established. Minimizing these uncertainties and unknowns would directly address the rate-limiting factor in our FFD framework. On the observational side, coordinated airborne measurements capable of attributing $N_{\mathrm{ice}}$ enhancement to specific mechanisms through simultaneous aerosol PSD and composition, PSD, ice habit, and INP characterization would be transformative in establishing observationally constrained freezing parameterizations. A systematic intercomparison of the KIT parameterization used here with those of Lawson et al. (2015) and Phillips et al. (2018)—the latter synthesizing available laboratory evidence across decades of literature—is a natural extension that is beyond the scope of the present work; such a comparison would clarify whether per-drop yield differences in the drizzle-size range carry meaningful consequences in a realistic cloud environment.

### 5.5 Implications for large-scale model representation

Bin microphysics schemes are not feasible for regional or global models. The bulk scheme developed here—with ABIFM and FFD documented in sufficient detail in Appendices A and B to support independent reproduction—provides a tractable pathway for representing INP-driven SIP in large-scale models. An underappreciated challenge in translating any FFD parameterization to this context is that the splinter formula is only one component: a compatible treatment of INP tracking, aerosol surface area specification, and primary freezing rate integration is equally necessary. These structural requirements are common to any immersion-mode implementation, whether adopting the KIT scheme used here, Lawson et al. (2015), or Phillips

https://doi.org/10.5194/egusphere-2026-4713
Preprint. Discussion started: 21 August 2026


et al. (2018), and the explicit coupling documented in this work is intended to be informative to large-scale modelers regardless of which parameterizations are ultimately selected.

## 6 Conclusions

We have presented a new laboratory-based parameterization of ice multiplication from the fragmentation of freezing drops (FFD) and evaluated it in large eddy simulations (LESs) of cumulus congestus against observed in situ particle size distributions (PSDs). The novelty of this parameterization lies in its characterization of observed pressure release events (PREs), which account for multiple physical mechanisms of material ejection during freezing (e.g., jetting, bubble bursting, cracking, and breakup). The laboratory studies yielded a temperature dependence in which PRE frequency increased with decreasing temperature for a 300 $\mu$m drop. Although the number of ice splinters produced per PRE could not be measured directly and the experiments were performed on a single drop size, we combined this temperature dependence with size-dependent splinter-number relationships from the literature, yielding a piecewise-linear function for the number of splinters produced as a function of temperature and drop size.

The new parameterization was evaluated in LES of a tropical cumulus congestus case study observed during the NASA CAMP$^2$Ex airborne field campaign. This study extends Stanford et al. (2025), which evaluated the liquid-phase evolution of the same case with an emphasis on the evolving drop size distribution (DSD) from cloud base (temperatures $\approx$22 °C) up to the 0 °C level. We extended the simulation to include mixed-phase microphysical processes to evaluate the simulated cloud system as updraft turrets transited temperatures as low as $-15$ °C. The FFD parameterization was implemented in both bin and double-moment bulk microphysics schemes, alongside the water-activity-based immersion freezing model (ABIFM) in both schemes to represent primary ice formation via ice-nucleating particles (INPs). Simulated PSDs were then evaluated against in situ observations across the same temperature range. The primary conclusions are as follows:

- Primary ice formation in both bin and bulk schemes produced ice number concentrations ($N_{\text{ice}}$) ranging from $10^{-4}$–1 L$^{-1}$, with a distinct peak $\sim$10$^{-1}$ L$^{-1}$.

- The baseline FFD mechanism negligibly enhanced $N_{\text{ice}}$ in either scheme. Applying a 10$\times$ multiplier on the number of ice splinters produced per freezing event—which remains a large source of uncertainty—increased the modal $N_{\text{ice}}$ to between 1 and 10 L$^{-1}$.

- Maximum $N_{\text{ice}}$ in the bulk simulation employing a 10$\times$ multiplier approached 10$^3$ L$^{-1}$, while the bin scheme produced maximum $N_{\text{ice}}$ of 10–20 L$^{-1}$. This disparity reflects substantial structural differences in how collision-coalescence is represented, namely explicit size-resolved collision pairs in the bin scheme versus moment-integrated collection kernels in the bulk scheme.

- Primary nucleation (immersion freezing) was the dominant ice multiplication source in the bin scheme, while collision-induced freezing was dominant in the bulk scheme, further reflecting the structural differences in collision mechanics between the schemes.

https://doi.org/10.5194/egusphere-2026-4713
Preprint. Discussion started: 21 August 2026


- A feedback between primary and secondary ice formation was identified in the bin scheme, wherein SIP produced elevated INP enrichment relative to the control simulation. Evidence suggests this feedback may be driven by precipitation-sized drops ($>$100 $\mu$m) that underwent collision-coalescence and accumulated INP mass prior to freezing, subsequently melted below the 0 °C level, and re-froze as highly enriched drops upon being lofted above 0 °C by updrafts. INP enrichment was not exclusive to rain-sized drops, as shifts in the cloud droplet population also contributed to elevated INP enrichment in the SIP simulation. No analogous feedback emerged in the bulk scheme, attributed to the bin scheme's explicit tracking of aerosol core mass through coagulation. This potential feedback mechanism warrants further investigation with Lagrangian particle-tracking frameworks, which would also better represent the stochastic, spatially localized nature of individual freezing events that both bin and bulk schemes necessarily treat as continuous fractional occurrences.

- Comparison with in situ observed PSDs showed that at all sub-freezing temperatures, primary ice formation alone yielded number concentrations 1–2 orders of magnitude below observations for sizes $>$200 $\mu$m. Including SIP with a 10$\times$ multiplier substantially reduced this discrepancy in both schemes, producing simulated PSDs that overlapped with observed values, though the mean behavior was insufficient to fully close the gap.

- Turbulence-induced collision enhancement was essential both for producing realistic DSD structures prior to reaching 0 °C and for SIP to produce substantial $N_{\text{ice}}$ enhancement throughout the mixed-phase region. Sensitivity tests neglecting this enhancement yielded orders-of-magnitude fewer precipitation-sized drops and negligible $N_{\text{ice}}$ enhancements by SIP even with a 10$\times$ multiplier, suggesting that SIP efficiency is strongly conditioned on the availability of precipitation-sized drops transiting the mixed-phase region.

- The inability of simulated PSDs to converge fully with observations likely reflects one or more of the following: limitations in representing the liquid DSD prior to the freezing level, inadequate primary ice formation by immersion freezing, insufficient ice production by the FFD parameterization even accounting for splinter-number uncertainty, or active SIP mechanisms not addressed in this work (e.g., ice-ice collisional breakup). Observational evidence does not support an active rime-splintering process in this case (Section 5.2), though its potential contribution cannot be entirely ruled out.

The FFD parameterization introduced here represents a starting point for improved characterization of secondary ice production based on updated laboratory measurements. By focusing exclusively on FFD, the parameterization captures effects from multiple physical sub-mechanisms—jetting, cracking, and bubble bursting—through a single temperature-dependent representation, while accounting for both immersion-nucleation and collision-induced freezing. Nonetheless, substantial uncertainties remain in quantifying fragment numbers, constraining the size dependence of FFD, and bridging laboratory measurements with natural cloud observations (e.g., Luke et al., 2021; Lawson et al., 2023; Lachapelle et al., 2025; Pfeifer et al., 2025). Targeted field campaigns such as SPICULE (Lawson et al., 2023) will be essential for developing the process-level understanding needed to independently evaluate and constrain laboratory findings. The broader community has similarly recognized the quantification of PIP and SIP processes, their interactions, and their representation in Earth system models as critical knowledge gaps requiring coordinated laboratory, observational, and modeling efforts (Knopf et al., 2026). The case study developed here and in Part I, constrained by available observations, contributes a benchmark suitable for evaluating mixed-phase process representations including FFD. Significant work remains in assessing this parameterization across different cloud regimes, refining it through new laboratory and field measurements, and evaluating it alongside parameterizations of additional SIP mechanisms—efforts that will be necessary to translate these representations into large-scale models where additional complexity and scale-dependent challenges arise.

*Code availability.* Code used to generate analyses and plots in this study are available on Github (github.com/mckenna-stanford-pnnl/camp2ex_sip; Zenodo DOI will be minted upon publication). Input aerosol profiles and distribution parameters and thermodynamic and kinematic soundings used for simulations are available in Part I's archive at https://doi.org/10.5281/zenodo.15901072 (Stanford, 2025). DHARMA source code is maintained at NASA GISS and can be made available upon request.

*Data availability.* Aircraft data are available on the CAMP2Ex data repository (https://www-air.larc.nasa.gov/cgi-bin/ArcView/camp2ex, NASA Suborbital Science Data for Atmospheric Composition, 2024). Simulation output is very large and is available upon request. Data from Keinert et al. (2020b) is available at the following: doi:10.5445/IR/1000117652 (Keinert et al., 2020a). Data from Kleinheins et al. (2021a) is available at the following: doi:10.5445/IR/1000129595 (Kleinheins et al., 2021b).

https://doi.org/10.5194/egusphere-2026-4713
Preprint. Discussion started: 21 August 2026


## Appendix A: Primary Ice Formation Parameterization: Water Activity ($a_w$) Based Immersion Freezing Model (ABIFM)

### A1 Theoretical Framework

Heterogeneous freezing is represented via immersion nucleation following the water activity ($a_w$) based immersion freezing model (ABIFM; Knopf and Alpert, 2013). Following convention in the nucleation literature, this section presents foundational quantities in CGS units, with conversion to SI units for model implementation described in subsequent sections (and in Table D1). ABIFM follows from classical nucleation theory, which describes heterogeneous freezing as a stochastic process whose rate depends on the properties of the INP and the thermodynamic state of the supercooled drop. The ice nucleation rate coefficient, $J_{\mathrm{het}}$ (cm$^{-2}$ s$^{-1}$), is expressed as a function of $\Delta a_w$ as:

$$\log_{10}(J_{\mathrm{het}}) = c + m\Delta a_w\,, \tag{A1}$$

where $c$ and $m$ are empirical intercept and slope parameters, respectively. The water activity criterion, $\Delta a_w$, is defined as the difference between the water activity of the supercooled drop at temperature $T$, $a_w(T)$, and the water activity of liquid in equilibrium with ice at the same temperature, $a_w^{\mathrm{ice}}(T)$:

$$\Delta a_w = a_w(T) - a_w^{\mathrm{ice}}(T)\,, \tag{A2}$$

where, for a droplet in equilibrium with atmospheric water vapor, $a_w$ is equivalent to the relative humidity (RH). For immersion freezing of water droplets, $a_w(T) = 1$ by definition, while $a_w(T) < 1$ in subsaturated conditions. Here, $a_w^{\mathrm{ice}}$ is taken from Koop and Zobrist (2009, their Eq. 7 in Appendix). The $c$ and $m$ parameters are derived from marine boundary layer observations collected during the U.S. Department of Energy Aerosol and Cloud Experiments in the Eastern North Atlantic (ACE-ENA) campaign by Knopf et al. (2023b), yielding $m = 5.791$ and $c = 1.128$. Thus, $J_{\mathrm{het}}$ depends only on RH and $T$.

Given $J_{\mathrm{het}}$, the volumetric drop freezing rate $\dot{N}_{\mathrm{frz}}$ (cm$^{-3}$ s$^{-1}$) is defined as the product of $J_{\mathrm{het}}$, the INP surface area ($s_{\mathrm{INP}}$; cm$^2$), and the number concentration of INP-containing droplets ($N_{\mathrm{INP}}$; cm$^{-3}$):

$$\dot{N}_{\mathrm{frz}} = J_{\mathrm{het}}(\Delta a_w) \cdot s_{\mathrm{INP}} \cdot N_{\mathrm{INP}}\,, \tag{A3}$$

where $s_{\mathrm{INP}} = 4\pi r_{\mathrm{INP}}^2$ (cm$^2$) and $r_{\mathrm{INP}}$ is the INP radius (cm). This formulation follows Knopf et al. (2023a) and Sun et al. (2026), the latter as implemented in a 1D cloud model. Physically, greater INP surface area and higher concentrations of INP-containing droplets both increase the freezing rate proportionally. For the bin and bulk scheme implementations, $s_{\mathrm{INP}}$ and $N_{\mathrm{INP}}$ are determined differently, as described below.

### A2 Bin Scheme

Hereafter, all quantities are in SI units unless otherwise noted. In the bin scheme, aerosol core mass inside drops is prognostic. For the $j^{\mathrm{th}}$ bin, the immersion freezing rate ($\dot{N}_j^{\mathrm{frz}}$; m$^{-3}$ s$^{-1}$) is given by:

$$\dot{N}_j^{\mathrm{frz}} = J_{\mathrm{het}}(\Delta a_w)\bar{s}_j N_{\mathrm{liq},j}\,, \tag{A4}$$

https://doi.org/10.5194/egusphere-2026-4713
Preprint. Discussion started: 21 August 2026


where $\bar{s}_j$ is the surface area of the mean equivalent spherical INP per drop (m$^2$ drop$^{-1}$), $N_{\mathrm{liq},j}$ is the drop number concentration in the $j^{\mathrm{th}}$ bin (m$^{-3}$), and $J_{\mathrm{het}}$ is converted from cm$^{-2}$ s$^{-1}$ to m$^{-2}$ s$^{-1}$ to maintain SI units. We assume that the total scavenged aerosol core mass within each drop acts as a single, spherical ice-nucleating particle. This simplification is necessary because the model does not track the number of individual aerosol particles scavenged by a given drop. While this assumption is violated during collision-coalescence events where drops merge their aerosol loads, tracking this process would require fundamental changes to the scheme's structure. $\bar{s}_j$ is determined by dividing the bin's core mass concentration ($Q_{\mathrm{core},j}$; kg m$^{-3}$) by $N_{\mathrm{liq},j}$ and the intrinsic core-material density ($\rho_{\mathrm{core}}$; kg m$^{-3}$), assuming a spherical geometry:

$$\bar{s}_j = 4\pi \left( \frac{3}{4\pi} \frac{f_{\mathrm{org}}\, Q_{\mathrm{core},j}}{N_{\mathrm{liq},j}\, \rho_{\mathrm{core}}} \right)^{\frac{2}{3}}, \tag{A5}$$

where $\rho_{\mathrm{core}}$ is ammonium bisulfate ($1.78 \times 10^3$ kg m$^{-3}$) and $f_{\mathrm{org}}$ is the volume-weighted organic aerosol fraction. $f_{\mathrm{org}}$ is derived from the volume-fraction-weighted hygroscopicity ($\kappa$) mixing rule (Petters and Kreidenweis, 2007) assuming the inorganic component of $\kappa$ is 0.53 for $(NH_4)_2SO_4$ and the organic component is 0.1, which yields $f_{\mathrm{org}} \approx 0.3$, consistent with bulk $\kappa$ = 0.4 constrained by aerosol mass spectrometer (AMS) measurements described in Part I and used in simulations here. The total freezing rate across all drops is then the sum across bins:

$$\dot{N}^{\mathrm{frz}} = J_{\mathrm{het}}(\Delta a_w) \sum_j \bar{s}_j N_{\mathrm{liq},j}. \tag{A6}$$

### A3 Bulk Scheme

#### A3.1 Lognormal surface area integral

The bulk scheme does not carry prognostic aerosol core mass. Instead, the total INP surface area concentration is derived analytically from the lognormal aerosol size distribution of activated aerosol in each mode (here, 3 modes; see Part I). For an aerosol mode $\mathfrak{m}$ with geometric mean number radius $r_{g,\mathfrak{m}}$ (m) and activated number concentration $N_{\mathrm{ac},\mathfrak{m}}$ (m$^{-3}$), the number size distribution ($n_{\mathfrak{m}}(r)$; m$^{-4}$) is:

$$n_{\mathfrak{m}}(r) = \frac{N_{\mathrm{ac},\mathfrak{m}}}{\sqrt{2\pi}\, r \ln \sigma_{g,\mathfrak{m}}} \exp\left( -\frac{\ln^2 (r/r_{g,\mathfrak{m}})}{2 \ln^2 \sigma_{g,\mathfrak{m}}} \right). \tag{A7}$$

The total INP surface area concentration contributed by mode $\mathfrak{m}$ is the second moment of this distribution:

$$S_{\mathfrak{m}} = \int_0^{\infty} 4\pi r^2\, n_{\mathfrak{m}}(r)\, dr, \tag{A8}$$

where $S_{\mathfrak{m}}$ has units m$^2$ m$^{-3}$.

We substitute Eq. A7 into Eq. A8 and evaluate using the standard lognormal moment relation $\langle r^k \rangle = r_g^k \exp\left( \frac{k^2}{2} \ln^2 \sigma_g \right)$ with $k = 2$. As with the bin scheme, only the organic fraction $f_{\mathrm{org}}$ of the aerosol core mass acts as INP; reducing the active volume

https://doi.org/10.5194/egusphere-2026-4713
Preprint. Discussion started: 21 August 2026


by $f_{\mathrm{org}}$ scales the equivalent sphere radius as $r \propto f_{\mathrm{org}}^{1/3}$ and hence surface area as $4\pi r^2 \propto f_{\mathrm{org}}^{2/3}$. Incorporating this correction gives:

$$S_{\mathfrak{m}} = N_{\mathrm{ac},\mathfrak{m}} \cdot f_{\mathrm{org}}^{\frac{2}{3}} \cdot 4\pi r_{g,\mathfrak{m}}^2 \cdot \exp\left(2\ln^2 \sigma_{g,\mathfrak{m}}\right) \,, \tag{A9}$$

where $f_{\mathrm{org}} \approx 0.3$ (see Appendix A2), and the factor $\exp(2\ln^2 \sigma_{g,\mathfrak{m}})$ is the lognormal second-moment correction. For a perfectly monodisperse distribution ($\sigma_{g,\mathfrak{m}} = 1$) this factor equals unity; for the aerosol modes defined in Part I ($\sigma_{g,\mathfrak{m}} \approx 1.5$) it is approximately 1.4, reflecting that the distribution-mean surface area exceeds that of a particle at the geometric mean radius, $4\pi r_{g,\mathfrak{m}}^2$, due to the finite width of the distribution.

The total INP surface area concentration summed over all $\mathfrak{M}$ aerosol modes is:

$$S = \sum_{\mathfrak{m}=1}^{\mathfrak{M}} N_{\mathrm{ac},\mathfrak{m}} \cdot f_{\mathrm{org}}^{\frac{2}{3}} \cdot 4\pi r_{g,\mathfrak{m}}^2 \cdot \exp\left(2\ln^2 \sigma_{g,\mathfrak{m}}\right) \,. \tag{A10}$$

### A3.2 Cloud droplet freezing

For cloud droplets, $N_{ac,\mathfrak{m}}$ is the prognostic activated aerosol concentration in mode $\mathfrak{m}$, which tracks aerosol number that resides inside cloud droplets. The cloud freezing rate tendency is then:

$$\dot{N}_c^{\mathrm{frz}} = J_{\mathrm{het}}(\Delta a_w) \cdot S_c, \qquad S_c = \sum_{\mathfrak{m}=1}^{\mathfrak{M}} N_{\mathrm{ac},\mathfrak{m}} \cdot f_{\mathrm{org}}^{\frac{2}{3}} \cdot 4\pi r_{g,\mathfrak{m}}^2 \cdot \exp\left(2\ln^2 \sigma_{g,\mathfrak{m}}\right) \,, \tag{A11}$$

where $S_c$ has units $\mathrm{m}^2\ \mathrm{m}^{-3}$ and $\dot{N}_c^{\mathrm{frz}}$ has units $\mathrm{m}^{-3}\ \mathrm{s}^{-1}$.

### A3.3 Rain drop freezing

The bulk scheme does not carry a prognostic variable for aerosol inside rain drops. As rain forms by collision–coalescence, aerosol originally tracked via $N_{\mathrm{ac},\mathfrak{m}}$ is transferred into rain drops and treated as a complete sink—it is removed from $N_{\mathrm{ac},\mathfrak{m}}$ and not reintroduced. To approximate the INP surface area available to rain drops without introducing a new prognostic, the activated aerosol pool is partitioned between cloud and rain by their respective liquid water mixing ratios, $q_c$ and $q_r$, assuming aerosol is distributed across liquid water proportionally to liquid water mass. The fraction attributed to rain is:

$$f_r = \frac{q_r}{q_c + q_r} \tag{A12}$$

and the rain INP surface area is:

$$S_r = f_r \cdot \sum_{\mathfrak{m}=1}^{\mathfrak{M}} N_{\mathrm{ac},\mathfrak{m}} \cdot f_{\mathrm{org}}^{\frac{2}{3}} \cdot 4\pi r_{g,\mathfrak{m}}^2 \cdot \exp\left(2\ln^2 \sigma_{g,\mathfrak{m}}\right) \,. \tag{A13}$$

The rain freezing rate tendency is then:

$$\dot{N}_r^{\mathrm{frz}} = J_{\mathrm{het}}(\Delta a_w) \cdot S_r \,. \tag{A14}$$

https://doi.org/10.5194/egusphere-2026-4713
Preprint. Discussion started: 21 August 2026


**Table B1.** Polynomial coefficients for Eq. B1.

| Polynomial Expression | Value |
|---|---|
| $a_0$ | 2.838 |
| $a_1$ | -0.2854 |
| $a_2$ | -0.0046 |
| $b_0$ | 0.136 |
| $b_1$ | 0.0008* |
| $c_0$ | 1.416 |

*$b_1$ has native units of $\mu\mathrm{m}^{-1}$ since the original parameterization for $N_t(D,T)$ uses drop diameter $D$ in units of microns. To use $D$ in meters, consistent with the rest of the derivation, the coefficient $b_1$ must be scaled accordingly. The original term $0.0008D_{\mu\mathrm{m}}$ is equivalent to $800D_{\mathrm{m}}$, hence $b_1$ = 800 $\mathrm{m}^{-1}$ is used when $D$ is in meters.

This uses $N_{\mathrm{ac,m}}$ as a proxy for the untracked aerosol inside rain drops, scaled by $f_r$ to reflect the proportion of liquid water residing in rain. In strongly precipitating, low-$q_c$ conditions, most activated aerosol has already been scavenged into rain and $N_{\mathrm{ac,m}}$ will be small, causing this approximation to underestimate rain drop INP loading. A future improvement would introduce a prognostic variable that tracks the activated aerosol transferred from the cloud to rain species during collision-coalescence.

## Appendix B: Secondary Ice Production Parameterizations

Secondary ice production is assumed to proceed by two pathways: freezing of liquid drops via INP immersion nucleation (ABIFM-SIP) and via collisions between ice and supercooled liquid drops (collisional SIP). These are discussed in the following sections. First, we rewrite Eq. 2 as the following for simplicity:

$$N_t(D,T) = \begin{cases} 0 & D < D_{\mathrm{lo}} \\ (a_2T^2 + a_1T + a_0)(b_1D + b_0) & D_{\mathrm{lo}} < D \le D_{\mathrm{hi}}\,, \\ c_0(a_2T^2 + a_1T + a_0) & D > D_{\mathrm{hi}} \end{cases} \tag{B1}$$

where $D_{\mathrm{lo}}$ = 50 $\mu$m, $D_{\mathrm{hi}}$ = 1600 $\mu$m, $T$ is in units of degrees Celsius, and the coefficients for Eq. B1 are listed in Table B1. Recognizing that the term $a_2T^2 + a_1T + a_0$ is independent of diameter, we call this term $\zeta(T)$ for simplicity, which can then be removed from all integrations across particle size.

https://doi.org/10.5194/egusphere-2026-4713
Preprint. Discussion started: 21 August 2026


### B1 Collisional SIP

#### B1.1 Bin Scheme

In the bin scheme, collisional SIP is computed in two steps. First, the Bott coagulation scheme (Bott, 1998) accumulates, for each target ice bin $j_{\mathrm{frz}}$, the number concentration of drops that freeze upon collision with a smaller ice particle. For a liquid drop in bin $j_{\mathrm{liq}}$ (diameter $D_{j_{\mathrm{liq}}} > D_{\mathrm{lo}}$) colliding with an ice particle in bin $j_{\mathrm{ice}}$ ($D_{j_{\mathrm{ice}}} < D_{j_{\mathrm{liq}}}$), the resulting frozen drop is distributed across target ice bins $j_{\mathrm{frz}}$ and $j_{\mathrm{frz}}+1$ according to the Bott flux-limiter weights $\mathcal{W}_{j_{\mathrm{frz}}}(j_{\mathrm{liq}}, j_{\mathrm{ice}})$. The collision-induced freezing rate into ice bin $j_{\mathrm{frz}}$, $\dot{F}_{j_{\mathrm{frz}}}$ ($\mathrm{m^{-3}\,s^{-1}}$), is therefore:

$$\dot{F}_{j_{\mathrm{frz}}} = \sum_{\substack{j_{\mathrm{liq}}:\, D_{j_{\mathrm{liq}}} > D_{\mathrm{lo}} \\ j_{\mathrm{ice}}:\, D_{j_{\mathrm{ice}}} < D_{j_{\mathrm{liq}}}}} K(D_{j_{\mathrm{liq}}}, D_{j_{\mathrm{ice}}})\, N_{\mathrm{liq},j_{\mathrm{liq}}}\, N_{\mathrm{ice},j_{\mathrm{ice}}}\, \mathcal{W}_{j_{\mathrm{frz}}}(j_{\mathrm{liq}}, j_{\mathrm{ice}})\,, \tag{B2}$$

where $K(D_{j_{\mathrm{liq}}}, D_{j_{\mathrm{ice}}})$ is the precomputed pairwise collision kernel ($\mathrm{m^3\ s^{-1}}$), $N_{\mathrm{liq},j_{\mathrm{liq}}}$ is the liquid number concentration in bin $j_{\mathrm{liq}}$ ($\mathrm{m^{-3}}$), $N_{\mathrm{ice},j_{\mathrm{ice}}}$ is the ice number concentration in bin $j_{\mathrm{ice}}$ ($\mathrm{m^{-3}}$), and bins where $D_{j_{\mathrm{liq}}} < D_{\mathrm{lo}}$ contribute zero splinters. Second, the KIT shattering multiplier is applied to the frozen drop bins to yield the splinter production rate:

$$\left(\frac{dN_{\mathrm{ice}}}{dt}\right)_{\text{coll-SIP,bin}} = \sum_{j_{\mathrm{frz}}} N_t(D_{j_{\mathrm{frz}}}, T)\, \dot{F}_{j_{\mathrm{frz}}}\,, \tag{B3}$$

where $N_t(D_{j_{\mathrm{frz}}}, T)$ (Eq. B1) is evaluated at the frozen-drop bin diameter $D_{j_{\mathrm{frz}}}$, which approximates the original liquid drop diameter upon freezing.

#### B1.2 Bulk Scheme

We start by assuming that the collision-induced FFD process in a double moment bulk microphysics scheme operates only during collisions of the rain and cloud ice species. In the absence of ice multiplication, we may define the time rate of change for the number concentration of cloud ice due to collisions between cloud ice and rain (notably representing a sink of both cloud ice and rain that forms either graupel or snow), following Reisner et al. (1998), by the following general formula:

$$\frac{dN_{ci}}{dt} = \int\limits_{D_r=0}^{\infty} \int\limits_{D_{ci}=0}^{\infty} K(D_r, D_{ci}) n_r(D_r) n_{ci}(D_{ci}) dD_r dD_{ci}\,, \tag{B4}$$

where $N_{ci}$ is the cloud ice number concentration ($\mathrm{m^{-3}}$), $D_r$ is the diameter of rain (m), $D_{ci}$ is the diameter of cloud ice (m), $n_r(D_r)$ is the number concentration of rain for diameter $D_r$ ($\mathrm{m^{-4}}$), $n_{ci}(D_{ci})$ is the number concentration of cloud ice for diameter $D_{ci}$ ($\mathrm{m^{-4}}$), and $K(D_r, D_{ci})$ is the hydrodynamic collision kernel between the species ($\mathrm{m^3\ s^{-1}}$). Since Eq. B4 represents a sink of cloud ice, we transform it into a source by including $N_t(D, T)$ (Eq. 2) in the integrand:

$$\left(\frac{dN_{ci}}{dt}\right)_{\text{coll-SIP,bulk}} = \int\limits_{D_r=0}^{\infty} \int\limits_{D_{ci}=0}^{\infty} K(D_r, D_{ci}) n_r(D_r) n_{ci}(D_{ci}) N_t(D_r, T) dD_r dD_{ci}\,. \tag{B5}$$

https://doi.org/10.5194/egusphere-2026-4713
Preprint. Discussion started: 21 August 2026


First, we recognize that the ice number concentration tendency due to FFD is independent of the size of cloud ice, such that the integral $\int_{D_{ci}=0}^{\infty} n_{ci}(D_{ci})dD_{ci} = N_{ci}$ and is pulled outside of the integrand. Next, we define a generalized form of the hydrodynamic collision kernel as follows:

$$K(D_r, D_{ci}) = E_{r,ci}(D_r, D_{ci})\pi \left(\frac{D_r + D_{ci}}{2}\right)^2 |V_r - V_{ci}|, \tag{B6}$$

where $V_r$ and $V_{ci}$ are the fall velocities of rain and cloud ice, respectively, and $E_{r,ci}$ is the collection efficiency (assumed to be unity). Eq. B6 is simplified by recognizing that $D_r \gg D_{ci}$ and $V_r \gg V_{ci}$ such that $K(D_r, D_{ci}) \approx \frac{\pi}{4} D_r^2 V_r$. In the warm-phase bulk microphysics setup employed in the current study, we use the Seifert (2008) parameterization for the rain fallspeed, which is defined as follows for a double-moment species:

$$V_{k,r} = \epsilon_0 - \epsilon_1 \left(1 + \frac{\epsilon_2}{\lambda_r}\right)^{-(\mu_r + k + 1)}, \tag{B7}$$

where $k$ is the moment (= 0 for number concentration), $\mu_r$ is the rain gamma distribution shape parameter (unitless), $\lambda_r$ is the rain gamma distribution slope parameter (units of m$^{-1}$), $\epsilon_0$ = 9.65 m s$^{-1}$, $\epsilon_1$ = 9.8 m s$^{-1}$, and $\epsilon_2$ = 600 m$^{-1}$. Therefore, we use the number-weighted bulk fallspeed for rain (dropping subscript $k$ for simplicity), $V_r$, calculated using Eq. B7 with $k = 0$ and the local rain distribution parameters $(\lambda_r, \mu_r)$. This value is then treated as constant in the diameter integration of Eq. B5. However, generalized power-law fall speed relationships are easily adaptable to this formulation and would appear as an additional diameter moment in the final equation. By employing these simplifications, Eq. B5 reduces to the following:

$$\left(\frac{dN_{ci}}{dt}\right)_{\text{coll-SIP,bulk}} = E_{r,ci}\frac{\pi}{4} V_r N_{ci} \int\limits_{D_r=0}^{\infty} D_r^2 n_r(D_r) N_t(D_r, T) dD_r\,. \tag{B8}$$

Finally, the rain PSD is defined as $n_r(D_r) = N_{0,r} D_r^{\mu_r} e^{-\lambda_r D_r}$, where $\mu_r$, $\lambda_r$, and $N_{0,r}$ are the shape, slope, and intercept parameters, respectively. Now, we must integrate $N_t(D_r, T)$ over the rain distribution in a piecewise manner. Dropping the subscript $r$ from $D$ for convenience, and integrating $N_t(D, T)$ over the rain PSD in a piecewise manner, Eq. B8 becomes:

$$\left(\frac{dN_{ci}}{dt}\right)_{\text{coll-SIP,bulk}} = E_{r,ci}\frac{\pi}{4} V_r N_{ci} \zeta(T) N_{0,r} \times \left[ b_1 \int\limits_{D_{\text{lo}}}^{D_{\text{hi}}} D^{\mu_r+3} e^{-\lambda_r D} dD + b_0 \int\limits_{D_{\text{lo}}}^{D_{\text{hi}}} D^{\mu_r+2} e^{-\lambda_r D} dD + c_0 \int\limits_{D_{\text{hi}}}^{\infty} D^{\mu_r+2} e^{-\lambda_r D} dD \right]. \tag{B9}$$

The bracketed term in Eq. B9 can now be represented as an incomplete gamma function. In a generalized form, the complete gamma function $\Gamma(\nu)$ is the sum of the lower incomplete gamma function $\gamma(\nu, x)$ and the upper incomplete gamma function $\Gamma(\nu, x)$ such that $\Gamma(\nu) = \gamma(\nu, x) + \Gamma(\nu, x)$. Here, $\nu$ is the argument (generally the sum of the shape parameter and the diameter moment plus 1), $x$ is the upper limit of integration for $\gamma(\nu, x)$, and $x$ is the lower limit of integration for $\Gamma(\nu, x)$. The general form for the lower incomplete gamma function is given by the following:

$$\gamma(\nu, x) = \int\limits_0^x y^{\nu-1} e^{-y} dy \tag{B10}$$

https://doi.org/10.5194/egusphere-2026-4713
Preprint. Discussion started: 21 August 2026


and for the upper incomplete gamma function as follows:

$$\Gamma(\nu, x) = \int_x^\infty y^{\nu-1} e^{-y} dy\,. \tag{B11}$$

Each bracketed term in Eq. B9 follows the general form $\int D^{k+\mu_r} e^{-\lambda_r D} dD$, where $k$ is the integer moment. Therefore, we make the substitutions that $x = \lambda_r D \Rightarrow D = \frac{x}{\lambda_r} \Rightarrow dD = \frac{dx}{\lambda_r}$. This transforms the generalized integral as follows: $\int D^{k+\mu_r} e^{-\lambda_r D} dD = \frac{1}{\lambda_r^{\mu_r+k+1}} \int x^{\mu_r+k} e^{-x} dx$. Importantly, since the lower limit for the first two bracketed terms in Eq. B9 is non-zero, we must express these bounded integrals as the difference of two lower incomplete gamma functions, each integrated from zero to the upper and lower limits. For example, this would take the following form: $\int_{x_1}^{x_2} y^{\nu-1} e^{-y} dy = \int_0^{x_2} y^{\nu-1} e^{-y} dy - \int_0^{x_1} y^{\nu-1} e^{-y} dy = \gamma(\nu, x_2) - \gamma(\nu, x_1)$, which yields $x_1 = \lambda_r D_{\text{lo}}$ and $x_2 = \lambda_r D_{\text{hi}}$. Now, we define $\nu - 1 = \mu_r + k \Rightarrow \nu = \mu_r + k + 1$. The first two bracketed terms in Eq. B9 are lower incomplete gamma functions (actually, the difference of two), while the last term is the upper incomplete gamma function. Therefore, Eq. B9 becomes:

785 $$\left(\frac{dN_{ci}}{dt}\right)_{\text{coll-SIP,bulk}} = E_{r,ci} \frac{\pi}{4} V_r N_{ci} \zeta(T) N_{0,r} \times \left[ b_1 \lambda_r^{-(\mu_r+4)} \left( \gamma(\mu_r+4, \lambda_r D_{\text{hi}}) - \gamma(\mu_r+4, \lambda_r D_{\text{lo}}) \right) + b_0 \lambda_r^{-(\mu_r+3)} \left( \gamma(\mu_r+3, \lambda_r D_{\text{hi}}) - \gamma(\mu_r+3, \lambda_r D_{\text{lo}}) \right) + c_0 \lambda_r^{-(\mu_r+3)} \Gamma(\mu_r+3, \lambda_r D_{\text{hi}}) \right]. \tag{B12}$$

Eq. B12 gives the cloud ice number concentration source from FFD, with all variables in SI units. We assume that each ice fragment is 5 $\mu$m, giving an individual fragment mass of $m_{\text{SIP}} = \frac{4}{3}\pi\rho_{ci}(2.5\times10^{-6})^3$ kg, where $\rho_{ci}$ = 917 kg m$^{-3}$. The resulting mass tendency, $\left(\frac{dq_{ci}}{dt}\right)_{\text{coll-SIP,bulk}}$, is a source term for cloud ice mass in units of kg kg$^{-1}$ s$^{-1}$. This mass originates from the collected rainwater. Per the model's mass conservation, this term should be accompanied by an equivalent sink in the rain mass. The remaining mass of the collected rain, now frozen, is transferred to graupel if the rain mass mixing ratio exceeds 0.1 g kg$^{-1}$ and snow otherwise, either of which represent the fractured frozen drop.

### B2 ABIFM-SIP

#### B2.1 Bin Scheme

In the bin scheme, FFD due to immersion freezing is computed directly alongside the ABIFM freezing calculation. For each drop bin $j$ with diameter $D_j$, immediately after the ABIFM freezing rate $\dot{N}_j^{\text{frz}}$ is calculated (Eq. A4), the number of splinters produced per unit time is:

$$\left(\frac{dN_{\text{ice}}}{dt}\right)_{\text{ABIFM-SIP,bin}} = \zeta(T)\left[ \sum_{\substack{j: \\ D_{\text{lo}} \le D_j \le D_{\text{hi}}}} (b_1 D_j + b_0)\, \dot{N}_j^{\text{frz}} + \sum_{\substack{j: \\ D_j > D_{\text{hi}}}} c_0\, \dot{N}_j^{\text{frz}} \right], \tag{B13}$$

https://doi.org/10.5194/egusphere-2026-4713
Preprint. Discussion started: 21 August 2026


where $\dot{N}_j^{\text{frz}} = J_{\text{het}}(\Delta a_w)\,\bar{s}_j\,N_{\text{liq},j}$ is the ABIFM freezing rate in bin $j$ (Eq. A4), $\zeta(T) = a_2T^2 + a_1T + a_0$ is the temperature-dependent prefactor of the KIT parameterization (Eq. B1), and bins where $D_j < D_{\text{lo}}$ contribute zero splinters.

### B2.2 Bulk Scheme

In the bulk scheme, the discrete bin sum in Eq. B13 is replaced by a continuous integral over the gamma rain PSD, $n_r(D) = N_{0,r}\,D^{\mu_r}e^{-\lambda_r D}$. FFD by immersion freezing of the cloud species is neglected given the lower limit of the base FFD parameterization (Eq. B1). The number concentration of ABIFM-frozen drops per unit diameter interval per unit volume is $J_{\text{het}}(\Delta a_w)\,\bar{s_r}\,n_r(D)$, where $\bar{s_r} = S_r/N_r$ (m$^2$ drop$^{-1}$) is the mean INP surface area per rain drop, obtained by dividing the lognormal-integrated surface area $S_r$ (Eq. A13) by the rain number concentration $N_r$ (m$^{-3}$). The splinter source rate is therefore:

$$\left(\frac{dN_{ci}}{dt}\right)_{\text{ABIFM-SIP,bulk}} = \int_0^\infty J_{\text{het}}(\Delta a_w)\,\bar{s_r}\;N_t(D,T)\,n_r(D)\,dD. \tag{B14}$$

Substituting the gamma rain PSD and pulling $J_{\text{het}}(\Delta a_w)$, $\bar{s}$, and $N_{0,r}$ outside the integral:

$$\left(\frac{dN_{ci}}{dt}\right)_{\text{ABIFM-SIP,bulk}} = J_{\text{het}}(\Delta a_w)\frac{S_r}{N_r}N_{0,r}\int_{D=0}^\infty N_t(D,T)D^{\mu_r}e^{-\lambda_r D}dD. \tag{B15}$$

Expanding $N_t(D,T)$ piecewise following Eq. B1 and pulling $\zeta(T)$ outside the integral:

$$\left(\frac{dN_{ci}}{dt}\right)_{\text{ABIFM-SIP,bulk}} = J_{\text{het}}(\Delta a_w)\frac{S_r}{N_r}\zeta(T)\,N_{0,r} \quad\times\quad \left[b_1\int_{D_{\text{lo}}}^{D_{\text{hi}}} D^{\mu_r+1}\,e^{-\lambda_r D}\,dD + b_0\int_{D_{\text{lo}}}^{D_{\text{hi}}} D^{\mu_r}\,e^{-\lambda_r D}\,dD + c_0\int_{D_{\text{hi}}}^{\infty} D^{\mu_r}\,e^{-\lambda_r D}\,dD\right]. \tag{B16}$$

Applying the same substitution $x = \lambda_r D$ as for the collision SIP (see Appendix B1.2, following Eqs. B9-B12), the integrals reduce to incomplete gamma functions. The final analytic form is:

$$\left(\frac{dN_{ci}}{dt}\right)_{\text{ABIFM-SIP,bulk}} = J_{\text{het}}(\Delta a_w)\frac{S_r}{N_r}\zeta(T)\,N_{0,r} \quad\times\quad \Big[b_1\,\lambda_r^{-(\mu_r+2)}\Big(\gamma(\mu_r+2,\,\lambda_r D_{\text{hi}}) - \gamma(\mu_r+2,\,\lambda_r D_{\text{lo}})\Big) + b_0\,\lambda_r^{-(\mu_r+1)}\Big(\gamma(\mu_r+1,\,\lambda_r D_{\text{hi}}) - \gamma(\mu_r+1,\,\lambda_r D_{\text{lo}})\Big) + c_0\,\lambda_r^{-(\mu_r+1)}\,\Gamma(\mu_r+1,\,\lambda_r D_{\text{hi}})\Big]. \tag{B17}$$

The mass and rain sink tendencies follow identically to collisional SIP: $(dq_{ci}/dt)_{\text{ABIFM-SIP,bulk}} = m_{\text{SIP}}\,(dN_{ci}/dt)_{\text{ABIFM-SIP,bulk}}$, which is simultaneously removed from the rain mass mixing ratio.

https://doi.org/10.5194/egusphere-2026-4713
Preprint. Discussion started: 21 August 2026


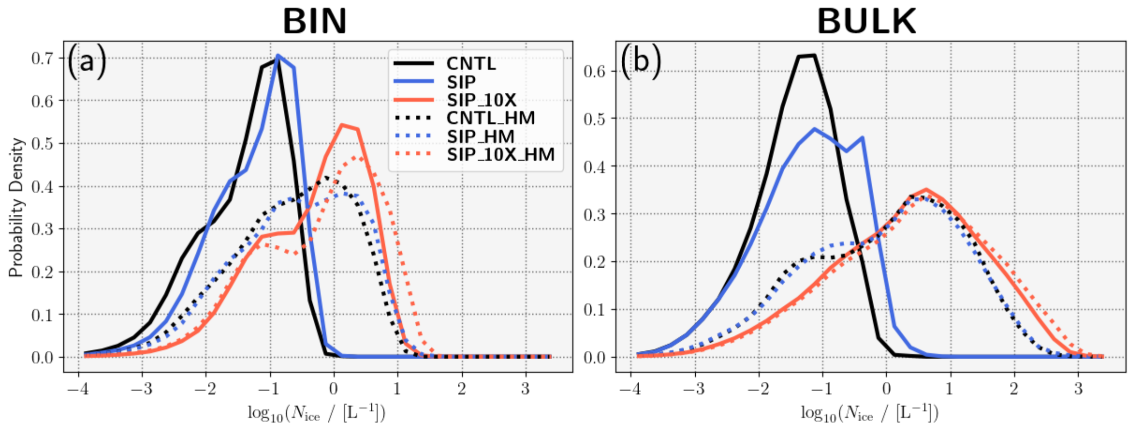


**Figure C1.** Probability distribution functions of ice number concentrations ($N_{\mathrm{ice}}$) for simulations without Hallett-Mossop (solid lines) and with Hallett-Mossop (dotted lines) for (a) bin-scheme simulations and (b) bulk-scheme simulations. Only cloudy grid points ($q_{\mathrm{ice}} > 10^{-3}$ g kg$^{-1}$) at temperatures colder than 0 °C are included.

## Appendix C: Inclusion of Hallett-Mossop SIP mechanism

Sensitivity tests are performed that include the Hallett-Mossop (rime-splintering) SIP mechanism. In the bin scheme, Hallett-Mossop follows from Pruppacher and Klett (2010, their Section 16.1.6) which assumes 1 splinter for every 250 collisions between large ice particles and small droplets, active between -3 and -8 °C and peaking at -5 °C. The Hallett-Mossop process requires a lower drop diameter limit of 24 $\mu$m, which is notably half the lower limit of the FFD mechanism. Although the two mechanisms involve opposing collision pairs (larger ice with smaller drops for Hallett-Mossop, the opposite for FFD), there are comparatively many more opportunities for Hallett-Mossop collisions since the lower size limit includes cloud droplets that dominate the number concentrations even at supercooled temperatures (see Fig. 12-13). For the bulk scheme, the Hallett-Mossop formulation assumes 350 splinters per milligram of rimed condensate at -5 °C and scales to zero pseudo-linearly at bounds of -3 and -8 °C (Pruppacher and Klett, 2010). Rime-splintering in the bulk scheme is permitted via collisions of snow or graupel with cloud or rain, dependent on condensate mass thresholds; however, there is no explicit size limit on the liquid drop.

PDFs of $N_{\mathrm{ice}}$ are shown in Fig. C1 for the three standard simulations (CNTL, SIP, and SIP_10X) and their Hallett-Mossop counterparts (appended with "HM") for both schemes. In both bin and bulk schemes, the addition of Hallett-Mossop to the CNTL simulations (i.e., no FFD but with Hallett-Mossop) shifts the distribution modes by 1-2 orders of magnitude. Including the baseline FFD parameterization (SIP simulations) in addition to Hallett-Mossop yields distributions that are essentially indistinguishable from the CNTL_HM simulations, implying that the Hallett-Mossop process minimizes any signal from the baseline FFD mechanism. Applying the 10× multiplier to FFD, combined with the Hallett-Mossop mechanism (SIP_10X_HM), yields a slightly longer high-concentration tail for the bin scheme, while the bulk scheme's distributions are nearly identical between SIP_10X and SIP_10X_HM.

https://doi.org/10.5194/egusphere-2026-4713
Preprint. Discussion started: 21 August 2026


These results imply that the Hallett-Mossop mechanism alone is more efficient than the baseline FFD mechanism in enhancing $N_{\rm ice}$ in this case study. The FFD mechanism alone is only comparable to Hallett-Mossop in ice-enhancement contributions with a $10\times$ multiplier applied the parameterization. However, recall that this multiplier is intended to span the large uncertainty in splinter production per freezing event. Including both processes yields the highest ice concentrations, though only marginally so relative to either mechanism alone.

Notably, observational evidence from this case does not support an active Hallett-Mossop process (see Section 5.2), suggesting these sensitivity tests are best interpreted as theoretical bounds rather than representations of active mechanisms. Within that context, the Hallett-Mossop mechanism alone produces $N_{\rm ice}$ comparable to FFD only with a $10\times$ multiplier applied, and including both processes yields only marginally higher ice concentrations relative to either mechanism alone. That two mechanisms of uncertain relevance produce similar $N_{\rm ice}$ further reinforces the primary ice bottleneck identified throughout this study, whereby SIP remains ultimately constrained by the availability of primary ice regardless of which SIP mechanism is active.

## Appendix D: Nomenclature

Table D1: List of symbols, variables, and acronyms used throughout the text.

| Notation | Definition | Units |
|---|---|---|
| **1. Atmospheric State & General Properties** | | |
| CLWC | Cloud Liquid Water Content | $\mathrm{g\,m^{-3}}$ |
| INP | Ice-Nucleating Particle | – |
| IWC | Ice Water Content | $\mathrm{g\,m^{-3}}$ |
| LWC | Liquid Water Content | $\mathrm{g\,m^{-3}}$ |
| RH | Ambient atmospheric relative humidity | % |
| RWC | Rain Water Content | $\mathrm{g\,m^{-3}}$ |
| TWC | Total Water Content | $\mathrm{g\,m^{-3}}$ |
| $T$ | Ambient atmospheric temperature | K |
| $t$ | Arbitrary time | s |
| $w$ | Vertical velocity | $\mathrm{m\,s^{-1}}$ |
| $\Delta t$ | Model time step | s |
| $\rho$ | Air density | $\mathrm{kg\,m^{-3}}$ |
| **2. Microphysical Processes & Distributions** | | |
| *2a. General* | | |

Continued on next page

https://doi.org/10.5194/egusphere-2026-4713
Preprint. Discussion started: 21 August 2026




| Notation | Definition | Units |
|---|---|---|
| BER | Bulk INP Enrichment Ratio | – |
| $D$ | Arbitrary particle diameter | m |
| $D_{\max}$ | Particle maximum dimension | m |
| $f_{\mathrm{org}}$ | Organic aerosol fraction | – |
| $\kappa$ | Hygroscopicity parameter | – |
| $N$ | Volumetric number concentration for arbitrary hydrometeor species | $\mathrm{m^{-3}}$ |
| $N_{\mathrm{ice}}$ | Ice number concentration | $\mathrm{m^{-3}}$ |
| $N_{\mathrm{INP}}$ | INP number concentration | $\mathrm{m^{-3}}$ |
| $N_{\mathrm{liq}}$ | Liquid number concentration | $\mathrm{m^{-3}}$ |
| $\dot{N}_{\mathrm{frz}}$ | Arbitrary volumetric drop freezing rate | $\mathrm{m^{-3}\,s^{-1}}$ |
| $q$ | Mass mixing ratio for arbitrary hydrometeor species | $\mathrm{kg\,kg^{-1}}$ |
| $q_l$ | Total liquid mass mixing ratio | $\mathrm{kg\,kg^{-1}}$ |
| $r$ | Arbitrary particle radius | m |
| $r_{\mathrm{INP}}$ | Radius of INP | m |
| $s_{\mathrm{INP}}$ | Surface area of INP | $\mathrm{m^2}$ |
| $\varepsilon$ | Turbulent kinetic energy dissipation rate | $\mathrm{m^2\,s^{-3}}$ |
| *2b. ABIFM* | | |
| $a_w$ | Water activity | – |
| $a_w^{\mathrm{ice}}$ | Ice melting point as a function of water activity | – |
| $c$ | Intercept parameter in $J_{\mathrm{het}}$ formula | – |
| $J_{\mathrm{het}}$ | Ice nucleation rate coefficient | $\mathrm{m^{-2}\,s^{-1}}$ |
| $m$ | Slope parameter in $J_{\mathrm{het}}$ formula | – |
| $\Delta a_w$ | Water activity criterion in ABIFM | – |
| *2c. Drop-Shattering Parameterization* | | |
| $a_0$ | Polynomial coefficient in KIT parameterization (see Table B1) | – |
| $a_1$ | Polynomial coefficient in KIT parameterization (see Table B1) | $^\circ\mathrm{C}^{-1}$ |
| $a_2$ | Polynomial coefficient in KIT parameterization (see Table B1) | $^\circ\mathrm{C}^{-2}$ |
| $b_0$ | Polynomial coefficient in KIT parameterization (see Table B1) | – |
| $b_1$ | Polynomial coefficient in KIT parameterization (see Table B1) | $\mathrm{m^{-1}}$ |
| $c_0$ | Polynomial coefficient in KIT parameterization (see Table B1) | – |

Continued on next page

https://doi.org/10.5194/egusphere-2026-4713
Preprint. Discussion started: 21 August 2026


Table D1 – continued from previous page

| Notation | Definition | Units |
|---|---|---|
| $D_{\mathrm{hi}}$ | Maximum diameter for linear portion of FFD piecewise-linear formula (Eq. B1) | m |
| $D_{\mathrm{lo}}$ | Minimum diameter for FFD formula (Eq. B1) | m |
| $N_t$ | Number of ice splinter fragments produced per drop freezing event | – |
| $n_{\mathrm{PRE}}$ | Number of pressure release events as a function of temperature (Eq. 1) | – |
| $\zeta(T)$ | Temperature-dependent polynomial used in Eq. B1 ($T$ in °C) | – |
| *2d. Bin Scheme* | | |
| $\dot{F}_{j_{\mathrm{frz}}}$ | In bin scheme, flux of collision-induced frozen drops into target ice bin $j_{\mathrm{frz}}$ from the Bott coagulation scheme | $\mathrm{m^{-3}\,s^{-1}}$ |
| $j$ | In bin scheme, arbitrary bin index | – |
| $j_{\mathrm{frz}}$ | In bin scheme, destination bin index for collision-induced frozen drops | – |
| $j_{\mathrm{ice}}$ | In bin scheme, ice species bin index | – |
| $j_{\mathrm{liq}}$ | In bin scheme, liquid species bin index | – |
| $\dot{N}^{\mathrm{frz}}$ | In bin scheme, volumetric freezing rate of liquid drops due to immersion freezing, summed across all bins | $\mathrm{m^{-3}\,s^{-1}}$ |
| $\dot{N}_j^{\mathrm{frz}}$ | In bin scheme, volumetric freezing rate of liquid drops due to immersion freezing in bin $j$ | $\mathrm{m^{-3}\,s^{-1}}$ |
| $N_{\mathrm{ice},j}$ | In bin scheme, ice number concentration in bin $j$ | $\mathrm{m^{-3}}$ |
| $N_{\mathrm{liq},j}$ | In bin scheme, liquid number concentration in bin $j$ | $\mathrm{m^{-3}}$ |
| $Q_{\mathrm{core},j}$ | In bin scheme, aerosol core mass concentration in drop bin $j$ | $\mathrm{kg\,m^{-3}}$ |
| $\rho_{\mathrm{core}}$ | In bin scheme, aerosol core mass density | $\mathrm{kg\,m^{-3}}$ |
| $S_{\mathrm{drop}}$ | In bin scheme, summed drop surface area concentration across all bins | $\mathrm{m^2\,m^{-3}}$ |
| $S_{\mathrm{INP}}$ | In bin scheme, summed INP surface area concentration across all bins | $\mathrm{m^2\,m^{-3}}$ |
| $\bar{s}_j$ | In bin scheme, average aerosol core surface area per drop in bin $j$ | $\mathrm{m^2}$ drop$^{-1}$ |
| $\mathcal{W}_{j_{\mathrm{frz}}}$ | In bin scheme, flux limiter weighting from Bott (1998) across target ice bins $j$ and $j+1$ | – |
| *2e. Bulk Scheme* | | |
| $D_{ci}$ | In bulk scheme, diameter of cloud ice species | m |
| $D_r$ | In bulk scheme, diameter of rain species | m |
| $E_{r,ci}$ | In bulk scheme, collection efficiency between cloud ice and rain species | – |

Continued on next page

https://doi.org/10.5194/egusphere-2026-4713
Preprint. Discussion started: 21 August 2026


Table D1 – continued from previous page

| Notation | Definition | Units |
|---|---|---|
| $\epsilon_0$ | Coefficient in hydrometeor fallspeed calculation (Seifert, 2008) | $\mathrm{m\,s^{-1}}$ |
| $\epsilon_1$ | Coefficient in hydrometeor fallspeed calculation (Seifert, 2008) | $\mathrm{m\,s^{-1}}$ |
| $\epsilon_2$ | Coefficient in hydrometeor fallspeed calculation (Seifert, 2008) | $\mathrm{m^{-1}}$ |
| $f_r$ | In bulk scheme, rain mass fraction | – |
| $K$ | In bulk scheme, hydrodynamic collision kernel | $\mathrm{m^3\,s^{-1}}$ |
| $k$ | Integer value denoting distribution moments | – |
| $\lambda$ | Arbitrary gamma distribution slope parameter | $\mathrm{m^{-1}}$ |
| $\lambda_r$ | Gamma distribution slope parameter for rain species | $\mathrm{m^{-1}}$ |
| $\mathfrak{M}$ | Total number of aerosol modes | – |
| $\mathfrak{m}$ | Aerosol mode index | – |
| $m_{\mathrm{SIP}}$ | In bulk scheme, mass of 5-$\mu$m droplet assumed for ice fragments | kg |
| $\mu$ | Arbitrary gamma distribution shape parameter | – |
| $\mu_r$ | Gamma distribution shape parameter for rain species | – |
| $N_0$ | Arbitrary gamma distribution intercept parameter | $\mathrm{m^{-4}}$ |
| $N_{0,r}$ | Gamma distribution intercept parameter for rain species | $\mathrm{m^{-4}}$ |
| $N_{\mathrm{ac},\mathfrak{m}}$ | In bulk scheme, number concentration of activated aerosol in mode $\mathfrak{m}$ in cloud droplets | $\mathrm{m^{-3}}$ |
| $N_{ci}$ | In bulk scheme, cloud ice number concentration | $\mathrm{m^{-3}}$ |
| $n_{ci}(D)$ | In bulk scheme, cloud ice number concentration per unit diameter | $\mathrm{m^{-4}}$ |
| $n_{\mathfrak{m}}(r)$ | In bulk scheme, aerosol number concentration of mode $\mathfrak{m}$ per unit radius | $\mathrm{m^{-4}}$ |
| $N_r$ | In bulk scheme, rain number concentration | $\mathrm{m^{-3}}$ |
| $n_r(D)$ | In bulk scheme, rain number concentration per unit diameter | $\mathrm{m^{-4}}$ |
| $\dot{N}_c^{\mathrm{frz}}$ | In bulk scheme, volumetric freezing rate of cloud droplets due to immersion freezing | $\mathrm{m^{-3}\,s^{-1}}$ |
| $\dot{N}_r^{\mathrm{frz}}$ | In bulk scheme, volumetric freezing rate of rain due to immersion freezing | $\mathrm{m^{-3}\,s^{-1}}$ |
| $q_c$ | In bulk scheme, mass mixing ratio of cloud droplets | $\mathrm{kg\,kg^{-1}}$ |
| $q_{ci}$ | In bulk scheme, mass mixing ratio of cloud ice | $\mathrm{kg\,kg^{-1}}$ |
| $q_r$ | In bulk scheme, mass mixing ratio of rain drops | $\mathrm{kg\,kg^{-1}}$ |
| $r_g$ | Arbitrary geometric mean radius of lognormal distribution | m |
| $r_{g,\mathfrak{m}}$ | Geometric mean radius of lognormal distribution for aerosol mode $\mathfrak{m}$ | m |

Continued on next page

https://doi.org/10.5194/egusphere-2026-4713
Preprint. Discussion started: 21 August 2026


Table D1 – continued from previous page

| Notation | Definition | Units |
|---|---|---|
| $\rho_{ci}$ | In bulk scheme, bulk density of cloud ice | $\mathrm{kg\,m^{-3}}$ |
| $S$ | In bulk scheme, total INP surface area concentration summed over all $\mathfrak{M}$ aerosol modes | $\mathrm{m^2\,m^{-3}}$ |
| $S_c$ | In bulk scheme, total INP surface area concentration in cloud droplets summed over all aerosol modes | $\mathrm{m^2\,m^{-3}}$ |
| $S_{\mathfrak{m}}$ | In bulk scheme, INP surface area concentration in aerosol mode $\mathfrak{m}$ | $\mathrm{m^2\,m^{-3}}$ |
| $S_r$ | In bulk scheme, total INP surface area concentration in rain drops summed over all aerosol modes | $\mathrm{m^2\,m^{-3}}$ |
| $\bar{s}_r$ | In bulk scheme, mean INP surface area per rain drop | $\mathrm{m^2}$ drop$^{-1}$ |
| $\sigma_g$ | Arbitrary geometric standard deviation of lognormal distribution | – |
| $\sigma_{g,\mathfrak{m}}$ | Geometric standard deviation of lognormal distribution for aerosol mode $\mathfrak{m}$ | – |
| $V_k$ | In bulk scheme, $k^{\mathrm{th}}$-moment fallspeed (Seifert, 2008) | $\mathrm{m\,s^{-1}}$ |
| $V_{k,ci}$ | In bulk scheme, fall velocity of cloud ice species for moment $k$ | $\mathrm{m\,s^{-1}}$ |
| $V_{k,r}$ | In bulk scheme, fall velocity of rain species for moment $k$ | $\mathrm{m\,s^{-1}}$ |
| $V_r$ | In bulk scheme, number-weighted bulk fall velocity of rain ($k=0$ in Eq. B7) | $\mathrm{m\,s^{-1}}$ |
| *2f. Gamma Functions* | | |
| $\Gamma(\nu)$ | Complete gamma function, where $\nu$ is an arbitrary argument | – |
| $\Gamma(\nu,x)$ | Upper incomplete gamma function, where $\nu$ is an arbitrary argument and $x$ is the lower limit of integration | – |
| $\gamma(\nu,x)$ | Lower incomplete gamma function, where $\nu$ is an arbitrary argument and $x$ is the upper limit of integration | – |
| **3. Acronyms & Models** | | |
| 2D-S | 2D-Stereo optical array probe | – |
| 3V-CPI | 3-View Cloud Particle Imager | – |
| ABIFM | Water Activity ($a_w$) Based Immersion Freezing Model | – |
| CARMA | Community Aerosol-Radiation-Microphysics Application | – |
| CTH | Cloud-Top Height | – |
| CTT | Cloud-Top Temperature | – |

Continued on next page

Table D1 – continued from previous page

| Notation | Definition | Units |
|---|---|---|
| DHARMA | Distributed Hydrodynamic Aerosol and Radiative Modeling for Atmospheres | – |
| DSD | Drop Size Distribution | – |
| FCDP | Fast Cloud Droplet Probe | – |
| FFD | Fragmentation of Freezing Drops | – |
| FFSSP | Fast Forward Scattering Spectrometer Probe | – |
| HSV | High-Speed Video camera | – |
| HVPS | High-Volume Precipitation Spectrometer | – |
| KIT | Karlsruhe Institute of Technology | – |
| LES | Large Eddy Simulation | – |
| MMD | Median Mass Diameter | $\mu$m |
| PIP | Primary Ice Production | – |
| PRE | Pressure Release Event | – |
| PSD | Particle Size Distribution | – |
| SIP | Secondary Ice Production | – |

*Author contributions.* MWS and AMF conceptualized the numerical simulation portion of the study. AK developed the drop-shattering parameterization with input from AAK and TL and wrote Section 2. MWS prepared simulations with the help of ASA and AMF. PL prepared in situ cloud probe data and guided use. DAK guided primary ice parameterization development. MWS performed formal analysis and wrote all sections besides Section 2. All authors reviewed and edited the manuscript.

*Competing interests.* At least one of the (co-)authors is a member of the editorial board of *Atmospheric Chemistry and Physics*. The authors have no other competing interests to declare.

*Financial support.* This work was supported by the NASA Atmospheric Composition Campaign Data Analysis and Modeling Program (ACCDAM; grant 20-ACCDAM20-0023) and the NASA Modeling, Analysis, and Prediction Program. MWS acknowledges additional financial support by the U.S. Department of Energy (DOE) Office of Science Office of Biological and Environmental Research (BER) through the Atmospheric System Research (ASR) program under project KP1701010/57131. DAK acknowledges support by U.S. DOE

https://doi.org/10.5194/egusphere-2026-4713
Preprint. Discussion started: 21 August 2026


grant DE-SC0021034. AAK, AK, and TL acknowledge financial support by the German Research Foundation (DFG) under Grants KI 1997/1-1 and KI 1997/1-2 as well as support by the Helmholtz Association under Atmosphere and Climate Programme (ATMO).

*Acknowledgements.* Computing support was primary provided the by NASA Center for Climate Simulations (NCCS). Additional support was provided by the National Energy Research Scientific Computing Center (NERSC), a Department of Energy (DOE) Office of Science user facility supported by the Office of Science of the U.S. DOE under Contract DE-AC02-05CH11231, and the Atmospheric Radiation Measurement (ARM) user facility with operational support from the Oak Ridge Leadership Computing Facility. The Oak Ridge Leadership Computing Facility at the Oak Ridge National Laboratory is supported by the Office of Science of the U.S. DOE under Contract No. DE-AC05-00OR22725. This work was part of the NASA CAMP2Ex campaign (https://doi.org/10.5067/Suborbital/CAMP2EX2018/DATA001). Pacific Northwest National Laboratory is operated by Battelle for the 644 US Department of Energy under Contract DE-AC05-76RLO1830.

https://doi.org/10.5194/egusphere-2026-4713
Preprint. Discussion started: 21 August 2026


## References

Abdul-Razzak, H. and Ghan, S. J.: A parameterization of aerosol activation 2. Multiple aerosol types, Journal of Geophysical Research Atmospheres, 105, 6837–6844, https://doi.org/10.1029/1999JD901161, 2000.

Ackerman, A. S., Hobbs, P. V., and Toon, O. B.: A Model for Particle Microphysics, Turbulent Mixing, and Radiative Transfer in the Stratocumulus-Topped Marine Boundary Layer and Comparisons with Measurements, Journal of Atmospheric Sciences, 52, 1204 – 1236, https://doi.org/10.1175/1520-0469(1995)052<1204:AMFPMT>2.0.CO;2, 1995.

Ackerman, A. S., Toon, O. B., Stevens, D. E., Heymsfield, A. J., Ramanathan, V., and Welton, E. J.: Reduction of Tropical Cloudiness by Soot, Science, 288, 1042–1047, https://doi.org/10.1126/SCIENCE.288.5468.1042, 2000.

Adkins, C. J.: The fragmentation and electrification of very small droplets, Quarterly Journal of the Royal Meteorological Society, 86, 186, https://doi.org/https://doi.org/10.1002/qj.49708636807, 1960.

Alpert, P. A., Kilthau, W. P., O'Brien, R. E., Moffet, R. C., Gilles, M. K., Wang, B., Laskin, A., Aller, J. Y., and Knopf, D. A.: Ice-nucleating agents in sea spray aerosol identified and quantified with a holistic multimodal freezing model, Science Advances, 8, https://doi.org/10.1126/SCIADV.ABQ6842;REQUESTEDJOURNAL:JOURNAL:SCIADV;WGROUP:STRING:PUBLICATION, 2022.

Ayala, O., Rosa, B., and Wang, L. P.: Effects of turbulence on the geometric collision rate of sedimenting droplets. Part 2. Theory and parameterization, New Journal of Physics, 10, 075 016, https://doi.org/10.1088/1367-2630/10/7/075016, 2008.

Bader, M., Gloster, J., Brownscombe, J. L., and Goldsmith, P.: The production of sub-micron ice fragments by water droplets freezing in free fall or on accretion upon an ice surface, Quarterly Journal of the Royal Meteorological Society, 100, 420–426, https://doi.org/10.1002/QJ.49710042513, 1974.

Beard, K. V. and Ochs, H. T.: Collection and coalescence efficiencies for accretion, Journal of Geophysical Research: Atmospheres, 89, 7165–7169, https://doi.org/10.1029/JD089ID05P07165, 1984.

Billault-Roux, A. C., Georgakaki, P., Gehring, J., Jaffeux, L., Schwarzenboeck, A., Coutris, P., Nenes, A., and Berne, A.: Distinct secondary ice production processes observed in radar Doppler spectra: insights from a case study, Atmospheric Chemistry and Physics, 23, 10 207–10 234, https://doi.org/10.5194/ACP-23-10207-2023, 2023.

Blossey, P. N., Bretherton, C. S., Cetrone, J., Kharoutdinov, M., Blossey, P. N., Bretherton, C. S., Cetrone, J., and Kharoutdinov, M.: Cloud-Resolving Model Simulations of KWAJEX: Model Sensitivities and Comparisons with Satellite and Radar Observations, Journal of the Atmospheric Sciences, 64, 1488–1508, https://doi.org/10.1175/JAS3982.1, 2007.

Böhm, H. P.: A General Equation for the Terminal Fall Speed of Solid Hydrometeors, Journal of Atmospheric Sciences, 46, 2419 – 2427, https://doi.org/10.1175/1520-0469(1989)046<2419:AGEFTT>2.0.CO;2, 1989.

Böhm, J. P.: A general hydrodynamic theory for mixed-phase microphysics. Part III: Riming and aggregation, Atmospheric Research, 28, 103–123, https://doi.org/10.1016/0169-8095(92)90023-4, 1992a.

Böhm, J. P.: A general hydrodynamic theory for mixed-phase microphysics. Part II: collision kernels for coalescence, Atmospheric Research, 27, 275–290, https://doi.org/10.1016/0169-8095(92)90036-A, 1992b.

Böhm, J. P.: A general hydrodynamic theory for mixed-phase microphysics. Part I: drag and fall speed of hydrometeors, Atmospheric Research, 27, 253–274, https://doi.org/10.1016/0169-8095(92)90035-9, 1992c.

Böhm, J. P.: Theoretical collision efficiencies for riming and aerosol impaction, Atmospheric Research, 32, 171–187, https://doi.org/10.1016/0169-8095(94)90058-2, 1994.

https://doi.org/10.5194/egusphere-2026-4713
Preprint. Discussion started: 21 August 2026


Böhm, J. P.: Revision and clarification of "A general hydrodynamic theory for mixed-phase microphysics", Atmospheric Research, 52, 167–176, https://doi.org/10.1016/S0169-8095(99)00033-2, 1999.

Böhm, J. P.: Reply to Comment on "Revision and clarification of 'A general hydrodynamic theory for mixed-phase microphysics' [Böhm J.P., 1999, Atmos. Res. 52, 167–176]", Atmospheric Research, 69, 289–293, https://doi.org/10.1016/J.ATMOSRES.2003.10.001, 2004.

Bott, A.: A Flux Method for the Numerical Solution of the Stochastic Collection Equation, Journal of the Atmospheric Sciences, 55, 2284 – 2293, https://doi.org/10.1175/1520-0469(1998)055<2284:AFMFTN>2.0.CO;2, 1998.

Caine, S., Lane, T. P., May, P. T., Jakob, C., Siems, S. T., Manton, M. J., Pinto, J., Caine, S., Lane, T. P., May, P. T., Jakob, C., Siems, S. T., Manton, M. J., and Pinto, J.: Statistical Assessment of Tropical Convection-Permitting Model Simulations Using a Cell-Tracking Algorithm, Monthly Weather Review, 141, 557–581, https://doi.org/10.1175/MWR-D-11-00274.1, 2013.

Cantrell, W. and Heymsfield, A.: Production of Ice in Tropospheric Clouds: A Review, Bulletin of the American Meteorological Society, 86, 795–808, https://doi.org/10.1175/BAMS-86-6-795, 2005.

Chandrakar, K. K., Morrison, H., Grabowski, W. W., and Lawson, R. P.: Are turbulence effects on droplet collision–coalescence a key to understanding observed rain formation in clouds?, Proceedings of the National Academy of Sciences of the United States of America, 121, e2319664 121, https://doi.org/10.1073/PNAS.2319664121/SUPPL_FILE/PNAS.2319664121.SAPP.PDF, 2024.

Field, P. R., Heymsfield, A. J., and Bansemer, A.: Shattering and particle interarrival times measured by optical array probes in ice clouds, Journal of Atmospheric and Oceanic Technology, 23, 1357–1371, https://doi.org/10.1175/JTECH1922.1, 2006.

Franklin, C. N., Protat, A., Leroy, D., and Fontaine, E.: Controls on phase composition and ice water content in a convection-permitting model simulation of a tropical mesoscale convective system, Atmospheric Chemistry and Physics, 16, 8767–8789, https://doi.org/10.5194/ACP-16-8767-2016, 2016.

Hall, D.: A detailed microphysical model within a two-dimensional dynamic framework: Model description and preliminary results, Journal of the Atmospheric Sciences, pp. 2486–2507, https://doi.org/10.1175/1520-0469(1980)037, 1980.

Hallett, J. and Mossop, S. C.: Production of secondary ice particles during the riming process, Nature, 249, 26–28, https://doi.org/10.1038/249026A0, 1974.

Han, B., Fan, J., Varble, A., Morrison, H., Williams, C. R., Chen, B., Dong, X., Giangrande, S. E., Khain, A., Mansell, E., Milbrandt, J. A., Shpund, J., and Thompson, G.: Cloud-Resolving Model Intercomparison of an MC3E Squall Line Case: Part II. Stratiform Precipitation Properties, Journal of Geophysical Research: Atmospheres, 124, 1090–1117, https://doi.org/10.1029/2018JD029596, 2019.

Heymsfield, A. and Willis, P.: Cloud Conditions Favoring Secondary Ice Particle Production in Tropical Maritime Convection, Journal of the Atmospheric Sciences, 71, 4500–4526, https://doi.org/10.1175/JAS-D-14-0093.1, 2014.

Hobbs, P. V. and Alkezweeny, A. J.: The Fragmentation of Freezing Water Droplets in Free Fall, Journal of Atmospheric Sciences, 25, 881 – 888, https://doi.org/10.1175/1520-0469(1968)025<0881:TFOFWD>2.0.CO;2, 1968.

Hoffmann, N., Kiselev, A., Rzesanke, D., Duft, D., and Leisner, T.: Experimental quantification of contact freezing in an electrodynamic balance, Atmospheric Measurement Techniques, 6, 2373–2382, https://doi.org/10.5194/AMT-6-2373-2013, 2013.

Huang, Y., Blyth, A. M., Brown, P. R., Choularton, T. W., and Cui, Z.: Factors controlling secondary ice production in cumulus clouds, Quarterly Journal of the Royal Meteorological Society, 143, 1021–1031, https://doi.org/10.1002/QJ.2987;WGROUP:STRING:PUBLICATION, 2017.

Huang, Y., Wu, W., McFarquhar, G. M., Xue, M., Morrison, H., Milbrandt, J., Korolev, A. V., Hu, Y., Qu, Z., Wolde, M., Nguyen, C., Schwarzenboeck, A., and Heckman, I.: Microphysical processes producing high ice water contents (HIWCs) in tropical convective clouds during the HAIC-HIWC field campaign: Dominant role of secondary ice production, Atmospheric Chemistry and Physics, 22, 2365–2384, https://doi.org/10.5194/ACP-22-2365-2022, 2022.

Jensen, E. J., Toon, O. B., Tabazadeh, A., Sachse, G. W., Anderson, B. E., Chan, K. R., Twohy, C. W., Gandrud, B., Aulenbach, S. M., Heymsfield, A., Hallett, J., and Gary, B.: Ice nucleation processes in upper tropospheric wave-clouds observed during SUCCESS, Geophysical Research Letters, 25, 1363–1366, https://doi.org/10.1029/98GL00299, 1998.

Johnson, D. A. and Hallett, J.: Freezing and shattering of supercooled water drops, Quarterly Journal of the Royal Meteorological Society, 94, 468–482, https://doi.org/10.1002/QJ.49709440204, 1968.

Keinert, A., Spannagel, D., Leisner, T., and Kiselev, A.: Additional Material for "Secondary Ice Production upon Freezing of Freely Falling Drizzle Droplets" - High Speed Video Footage and SIP Event Frequencies [Dataset], https://doi.org/10.5445/IR/1000117652, 2020a.

Keinert, A., Spannagel, D., Leisner, T., and Kiselev, A.: Secondary Ice Production upon Freezing of Freely Falling Drizzle Droplets, Journal of the Atmospheric Sciences, 77, 2959–2967, https://doi.org/10.1175/JAS-D-20-0081.1, 2020b.

Kirkpatrick, M. P., Ackerman, A. S., Stevens, D. E., and Mansour, N. N.: On the Application of the Dynamic Smagorinsky Model to Large-Eddy Simulations of the Cloud-Topped Atmospheric Boundary Layer, Journal of the Atmospheric Sciences, 63, 526–546, https://doi.org/10.1175/JAS3651.1, 2006.

Kleinheins, J., Kiselev, A., Keinert, A., Kind, M., and Leisner, T.: Thermal Imaging of Freezing Drizzle Droplets: Pressure Release Events as a Source of Secondary Ice Particles, Journal of the Atmospheric Sciences, 78, 1703–1713, https://doi.org/10.1175/JAS-D-20-0323.1, 2021a.

Kleinheins, J., Kiselev, A., Keinert, A., Leisner, T., and Kind, M.: Supplementary data for J. Kleinheins et al. "Thermal imaging of freezing drizzle droplets: pressure release events as a source of secondary ice particles", Journal of the Atmospheric Sciences 2021, [Dataset]., https://doi.org/10.5445/IR/1000129595, 2021b.

Knopf, D. A.: Microanalysis Techniques to Study Atmospheric Ice Nucleation and Ice Crystal Growth, Microanalysis of Atmospheric Particles: Techniques and Applications, pp. 223–252, https://doi.org/10.1002/9781119554318.CH11, 2024.

Knopf, D. A. and Alpert, P. A.: A water activity based model of heterogeneous ice nucleation kinetics for freezing of water and aqueous solution droplets, Faraday Discussions, 165, 513–534, https://doi.org/10.1039/C3FD00035D, 2013.

Knopf, D. A. and Alpert, P. A.: Atmospheric ice nucleation, Nature Reviews Physics 2023 5:4, 5, 203–217, https://doi.org/10.1038/s42254-023-00570-7, 2023.

Knopf, D. A., Alpert, P. A., Zipori, A., Reicher, N., and Rudich, Y.: Stochastic nucleation processes and substrate abundance explain time-dependent freezing in supercooled droplets, npj Climate and Atmospheric Science 2020 3:1, 3, 2–, https://doi.org/10.1038/s41612-020-0106-4, 2020.

Knopf, D. A., Barry, K. R., Brubaker, T. A., Jahl, L. G., Jankowski, K. A., Li, J., Lu, Y., Monroe, L. W., Moore, K. A., Rivera-Adorno, F. A., Sauceda, K. A., Shi, Y., Tomlin, J. M., Vepuri, H. S. K., Wang, P., Lata, N. N., Levin, E. J. T., Creamean, J. M., Hill, T. C. J., China, S., Alpert, P. A., Moffet, R. C., Hiranuma, N., Sullivan, R. C., Fridlind, A. M., West, M., Riemer, N., Laskin, A., DeMott, P. J., Liu, X., Knopf, D. A., Barry, K. R., Brubaker, T. A., Jahl, L. G., Jankowski, K. A., Li, J., Lu, Y., Monroe, L. W., Moore, K. A., Rivera-Adorno, F. A., Sauceda, K. A., Shi, Y., Tomlin, J. M., Vepuri, H. S. K., Wang, P., Lata, N. N., Levin, E. J. T., Creamean, J. M., Hill, T. C. J., China, S., Alpert, P. A., Moffet, R. C., Hiranuma, N., Sullivan, R. C., Fridlind, A. M., West, M., Riemer, N., Laskin, A., DeMott, P. J., and Liu, X.: Aerosol–Ice Formation Closure: A Southern Great Plains Field Campaign, Bulletin of the American Meteorological Society, 102, E1952–E1971, https://doi.org/10.1175/BAMS-D-20-0151.1, 2021.

https://doi.org/10.5194/egusphere-2026-4713
Preprint. Discussion started: 21 August 2026


Knopf, D. A., Silber, I., Riemer, N., Fridlind, A. M., and Ackerman, A. S.: A 1D Model for Nucleation of Ice From Aerosol Particles: An Application to a Mixed-Phase Arctic Stratus Cloud Layer, Journal of Advances in Modeling Earth Systems, 15, e2023MS003 663, https://doi.org/10.1029/2023MS003663, 2023a.

Knopf, D. A., Wang, P., Wong, B., Tomlin, J. M., Veghte, D. P., Lata, N. N., China, S., Laskin, A., Moffet, R. C., Aller, J. Y., Marcus, M. A., and Wang, J.: Physicochemical characterization of free troposphere and marine boundary layer ice-nucleating particles collected by aircraft in the eastern North Atlantic, Atmospheric Chemistry and Physics, 23, 8659–8681, https://doi.org/10.5194/ACP-23-8659-2023, 2023b.

Knopf, D. A., Burrows, S., Creamean, J., Barahona, D., Bertram, A., Chen, S., Fan, J., Fierce, L., French, J., Fridlind, A., Kanji, Z., Kollias, P., Korolev, A., Laskin, A., Liu, X., McCluskey, C., Möhler, O., Ovchinikov, M., Phillips, V., Shaw, R., Shupe, M., Silber, I., Stratmann, F., Tan, I., Yang, F., Zhang, K., and Zheng, X.: Atmospheric System Research Workshop Report: New Directions in
}Atmospheric Ice Processes Research, DOE/SC-2023., Tech. rep., Department of Energy's Biological and Environmental Research Program, U.S. Department of Energy, Office of Science., https://doi.org/https://doi.org/10.2172/3030696, 2026.

Kolomeychuk, R. J., McKay, D. C., and Iribarne, J. V.: The Fragmentation and Electrification of Freezing Drops, Journal of Atmospheric Sciences, 32, 974 – 979, https://doi.org/10.1175/1520-0469(1975)032<0974:TFAEOF>2.0.CO;2, 1975.

Koop, T. and Zobrist, B.: Parameterizations for ice nucleation in biological and atmospheric systems, Phys. Chem. Chem. Phys., 11, 10 839–10 850, https://doi.org/10.1039/B914289D, 2009.

Korolev, A. and Leisner, T.: Review of experimental studies of secondary ice production, Atmospheric Chemistry and Physics, 20, 11 767–11 797, https://doi.org/10.5194/ACP-20-11767-2020, 2020.

Korolev, A., Heckman, I., Wolde, M., Ackerman, A. S., Fridlind, A. M., Ladino, L. A., Paul Lawson, R., Milbrandt, J., and Williams, E.: A new look at the environmental conditions favorable to secondary ice production, Atmospheric Chemistry and Physics, 20, 1391–1429, https://doi.org/10.5194/ACP-20-1391-2020, 2020.

Korolev, A., Qu, Z., Milbrandt, J., Heckman, I., Cholette, M., Wolde, M., Nguyen, C., McFarquhar, G. M., Lawson, P., and Fridlind, A. M.: High ice water content in tropical mesoscale convective systems (a conceptual model), Atmospheric Chemistry and Physics, 24, 11 849–11 881, https://doi.org/10.5194/ACP-24-11849-2024, 2024.

Korolev, A. V., Strapp, J. W., Isaac, G. A., and Nevzorov, A. N.: The Nevzorov Airborne Hot-Wire LWC–TWC Probe: Principle of Operation and Performance Characteristics, Journal of Atmospheric and Oceanic Technology, 15, 1495–1510, https://doi.org/https://doi.org/10.1175/1520-0426(1998)015<1495:TNAHWL>2.0.CO;2, 1998.

Lachapelle, M., Nichman, L., Girouard, M., Nguyen, C., Ranjbar, K., Bliankinshtein, N., Bala, K., Thériault, J. M., French, J. R., Minder, J. R., Wolde, M., Lachapelle, M., Nichman, L., Girouard, M., Nguyen, C., Ranjbar, K., Bliankinshtein, N., Bala, K., Thériault, J. M., French, J. R., Minder, J. R., and Wolde, M.: Airborne and Ground Measurements for Vertical Profiling of Secondary Ice Production during Ice Pellet Precipitation, Journal of the Atmospheric Sciences, 82, 559–583, https://doi.org/10.1175/JAS-D-24-0117.1, 2025.

Ladino, L. A., Korolev, A., Heckman, I., Wolde, M., Fridlind, A. M., and Ackerman, A. S.: On the role of ice-nucleating aerosol in the formation of ice particles in tropical mesoscale convective systems, Geophysical Research Letters, 44, 1574–1582, https://doi.org/10.1002/2016GL072455, 2017.

Lang, S. E., Tao, W.-K., Zeng, X., Li, Y., Lang, S. E., Tao, W.-K., Zeng, X., and Li, Y.: Reducing the Biases in Simulated Radar Reflectivities from a Bulk Microphysics Scheme: Tropical Convective Systems, Journal of the Atmospheric Sciences, 68, 2306–2320, https://doi.org/10.1175/JAS-D-10-05000.1, 2011.

https://doi.org/10.5194/egusphere-2026-4713
Preprint. Discussion started: 21 August 2026


Lang, S. E., Tao, W.-K., Chern, J.-D., Wu, D., Li, X., Lang, S. E., Tao, W.-K., Chern, J.-D., Wu, D., and Li, X.: Benefits of a Fourth Ice Class in the Simulated Radar Reflectivities of Convective Systems Using a Bulk Microphysics Scheme, Journal of the Atmospheric Sciences, 71, 3583–3612, https://doi.org/10.1175/JAS-D-13-0330.1, 2014.

Lasher-Trapp, S., Leon, D. C., DeMott, P. J., Villanueva-Birriel, C. M., Johnson, A. V., Moser, D. H., Tully, C. S., and Wu, W.: A multisensor investigation of rime splintering in tropical maritime cumuli, Journal of the Atmospheric Sciences, 73, 2547–2564, https://doi.org/10.1175/JAS-D-15-0285.1, 2016.

Lauber, A., Kiselev, A., Pander, T., Handmann, P., and Leisner, T.: Secondary ice formation during freezing of levitated droplets, Journal of the Atmospheric Sciences, 75, 2815–2826, https://doi.org/10.1175/JAS-D-18-0052.1, 2018.

Lauber, A., Henneberger, J., Mignani, C., Ramelli, F., Pasquier, J. T., Wieder, J., Hervo, M., and Lohmann, U.: Continuous secondary-ice production initiated by updrafts through the melting layer in mountainous regions, Atmospheric Chemistry and Physics, 21, 3855–3870, https://doi.org/10.5194/ACP-21-3855-2021, 2021.

Lawson, R. P., Stewart, R. E., and Angus, L. J.: Observations and Numerical Simulations of the Origin and Development of Very Large Snowflakes, Journal of the Atmospheric Sciences, 55, 3209 – 3229, https://doi.org/10.1175/1520-0469(1998)055<3209:OANSOT>2.0.CO;2, 1998.

Lawson, R. P., Baker, B. A., Schmitt, C. G., and Jensen, T. L.: An overview of microphysical properties of Arctic clouds observed in May and July 1998 during FIRE ACE, Journal of Geophysical Research: Atmospheres, 106, 14 989–15 014, https://doi.org/10.1029/2000JD900789, 2001.

Lawson, R. P., O'Connor, D., Zmarzly, P., Weaver, K., Baker, B., Mo, Q., and Jonsson, H.: The 2D-S (Stereo) Probe: Design and Preliminary Tests of a New Airborne, High-Speed, High-Resolution Particle Imaging Probe, Journal of Atmospheric and Oceanic Technology, 23, 1462–1477, https://doi.org/10.1175/JTECH1927.1, 2006.

Lawson, R. P., Woods, S., and Morrison, H.: The microphysics of ice and precipitation development in tropical cumulus clouds, Journal of the Atmospheric Sciences, 72, 2429–2445, https://doi.org/10.1175/JAS-D-14-0274.1, 2015.

Lawson, R. P., Gurganus, C., Woods, S., and Bruintjes, R.: Aircraft observations of cumulus microphysics ranging from the tropics to midlatitudes: Implications for a "new" secondary ice process, Journal of the Atmospheric Sciences, 74, 2899–2920, https://doi.org/10.1175/JAS-D-17-0033.1, 2017.

Lawson, R. P., Bruintjes, R., Woods, S., and Gurganus, C.: Coalescence and Secondary Ice Development in Cumulus Congestus Clouds, Journal of the Atmospheric Sciences, 79, 953–972, https://doi.org/10.1175/JAS-D-21-0188.1, 2022.

Lawson, R. P., Korolev, A. V., DeMott, P. J., Heymsfield, A. J., Bruintjes, R. T., Wolff, C. A., Woods, S., Patnaude, R. J., Jensen, J. B., Moore, K. A., Heckman, I., Rosky, E., Haggerty, J., Perkins, R. J., Fisher, T., and Hill, T. C.: The Secondary Production of Ice in Cumulus Experiment (SPICULE), Bulletin of the American Meteorological Society, 104, E51–E76, https://doi.org/10.1175/BAMS-D-21-0209.1, 2023.

Lee, H., Fridland, A. M., and Ackerman, A. S.: An Evaluation of Size-Resolved Cloud Microphysics Scheme Numerics for Use with Radar Observations. Part II: Condensation and Evaporation, Journal of the Atmospheric Sciences, 78, 1629–1645, https://doi.org/10.1175/JAS-D-20-0213.1, 2021.

Li, H., Möhler, O., Petäjä, T., and Moisseev, D.: Two-year statistics of columnar-ice production in stratiform clouds over Hyytiälä, Finland: Environmental conditions and the relevance to secondary ice production, Atmospheric Chemistry and Physics, 21, 14 671–14 686, https://doi.org/10.5194/ACP-21-14671-2021, 2021.

https://doi.org/10.5194/egusphere-2026-4713
Preprint. Discussion started: 21 August 2026


Li, Y., Zipser, E. J., Krueger, S. K., Zulauf, M. A., Li, Y., Zipser, E. J., Krueger, S. K., and Zulauf, M. A.: Cloud-Resolving Modeling of Deep Convection during KWAJEX. Part I: Comparison to TRMM Satellite and Ground-Based Radar Observations, Monthly Weather Review, 136, 2699–2712, https://doi.org/10.1175/2007MWR2258.1, 2008.

Luke, E. P., Yang, F., Kollias, P., Vogelmann, A. M., and Maahn, M.: New insights into ice multiplication using remote-sensing observations of slightly supercooled mixed-phase clouds in the Arctic, Proceedings of the National Academy of Sciences of the United States of America, 118, e2021387 118, https://doi.org/10.1073/PNAS.2021387118/SUPPL_FILE/PNAS.2021387118.SM01.GIF, 2021.

Matsui, T., Zeng, X., Tao, W.-K., Masunaga, H., Olson, W. S., Lang, S., Matsui, T., Zeng, X., Tao, W.-K., Masunaga, H., Olson, W. S., and Lang, S.: Evaluation of Long-Term Cloud-Resolving Model Simulations Using Satellite Radiance Observations and Multifrequency Satellite Simulators, Journal of Atmospheric and Oceanic Technology, 26, 1261–1274, https://doi.org/10.1175/2008JTECHA1168.1, 2009.

McCluskey, C. S., Hill, T. C., Humphries, R. S., Rauker, A. M., Moreau, S., Strutton, P. G., Chambers, S. D., Williams, A. G., McRobert, I., Ward, J., Keywood, M. D., Harnwell, J., Ponsonby, W., Loh, Z. M., Krummel, P. B., Protat, A., Kreidenweis, S. M., and DeMott, P. J.: Observations of Ice Nucleating Particles Over Southern Ocean Waters, Geophysical Research Letters, 45, 989–11, https://doi.org/10.1029/2018GL079981;CTYPE:STRING:JOURNAL, 2018.

Mitchell, D. L.: Use of Mass- and Area-Dimensional Power Laws for Determining Precipitation Particle Terminal Velocities, Journal of Atmospheric Sciences, 53, 1710 – 1723, https://doi.org/10.1175/1520-0469(1996)053<1710:UOMAAD>2.0.CO;2, 1996.

Morrison, H., Curry, J. A., and Khvorostyanov, V. I.: A New Double-Moment Microphysics Parameterization for Application in Cloud and Climate Models. Part I: Description, Journal of the Atmospheric Sciences, 62, 1665–1677, https://doi.org/10.1175/JAS3446.1, 2005.

Morrison, H., Thompson, G., and Tatarskii, V.: Impact of Cloud Microphysics on the Development of Trailing Stratiform Precipitation in a Simulated Squall Line: Comparison of One- and Two-Moment Schemes, Monthly Weather Review, 137, 991–1007, https://doi.org/10.1175/2008MWR2556.1, 2009.

Mossop, S. C. and Hallett, J.: Ice crystal concentration in cumulus clouds: Influence of the drop spectrum, Science, 186, 632–633, https://doi.org/10.1126/SCIENCE.186.4164.632, 1974.

O'Connor, D., Baker, B., and Lawson, R. P.: Upgrades to the FSSP-100 Electronics, Int. Conf. on Clouds and Precipitation, Cancun, Mexico, IAMAS, http://cabernet.atmosfcu.unam.mx/ICCP-2008/abstracts/Program_on_line/Poster_13/O-Connor_extended.pdf, 2008.

Petters, M. D. and Kreidenweis, S. M.: A single parameter representation of hygroscopic growth and cloud condensation nucleus activity, Atmospheric Chemistry and Physics, 7, 1961–1971, https://doi.org/10.5194/ACP-7-1961-2007, 2007.

Pfeifer, N., Mom, B., Moisseev, D., Hartmann, S., Meusel, J., Hoose, C., and Maahn, M.: Efficient ice multiplication from freezing raindrop fragmentation, Communications Earth & Environment 2025 6:1, 6, 942–, https://doi.org/10.1038/s43247-025-02953-3, 2025.

Phillips, V. T., Yano, J. I., Formenton, M., Ilotoviz, E., Kanawade, V., Kudzotsa, I., Sun, J., Bansemer, A., Detwiler, A. G., Khain, A., and Tessendorf, S. A.: Ice Multiplication by Breakup in Ice–Ice Collisions. Part II: Numerical Simulations, Journal of the Atmospheric Sciences, 74, 2789–2811, https://doi.org/10.1175/JAS-D-16-0223.1, 2017a.

Phillips, V. T., Yano, J. I., and Khain, A.: Ice Multiplication by Breakup in Ice–Ice Collisions. Part I: Theoretical Formulation, Journal of the Atmospheric Sciences, 74, 1705–1719, https://doi.org/10.1175/JAS-D-16-0224.1, 2017b.

Phillips, V. T., Patade, S., Gutierrez, J., and Bansemer, A.: Secondary Ice Production by Fragmentation of Freezing Drops: Formulation and Theory, Journal of the Atmospheric Sciences, 75, 3031–3070, https://doi.org/10.1175/JAS-D-17-0190.1, 2018.

Pruppacher, H. R. and Klett, J. D.: Microphysics of Clouds and Precipitation, Springer Dordrecht, 2nd edn., https://doi.org/10.1007/978-0-306-48100-0, 2010.

https://doi.org/10.5194/egusphere-2026-4713
Preprint. Discussion started: 21 August 2026


Qu, Y., Khain, A., Phillips, V., Ilotoviz, E., Shpund, J., Patade, S., and Chen, B.: The Role of Ice Splintering on Microphysics of Deep Convective Clouds Forming Under Different Aerosol Conditions: Simulations Using the Model With Spectral Bin Microphysics, Journal of Geophysical Research: Atmospheres, 125, e2019JD031 312, https://doi.org/10.1029/2019JD031312, 2020.

Qu, Z., Korolev, A., Milbrandt, J. A., Heckman, I., Huang, Y., Mcfarquhar, G. M., Morrison, H., Wolde, M., and Nguyen, C.: The impacts of secondary ice production on microphysics and dynamics in tropical convection, Atmospheric Chemistry and Physics, 22, 12 287–12 310, https://doi.org/10.5194/ACP-22-12287-2022,, 2022.

Qu, Z., Korolev, A., Milbrandt, J. A., Heckman, I., Cholette, M., Nguyen, C., and Wolde, M.: The impacts of secondary ice production on the microphysics and dynamics of mid-latitude cold season convection, Atmospheric Chemistry and Physics, 25, 17 845–17 868, https://doi.org/10.5194/ACP-25-17845-2025, 2025.

Reid, J. S., Maring, H. B., Narisma, G. T., Van Den Heever, S., Girolamo, L. D., Ferrare, R., Lawson, P., Mace, G. G., Simpas, J. B., Tanelli, S., Ziemba, L., Van Diedenhoven, B., Bruintjes, R., Bucholtz, A., Flynn, C. B., Cambaliza, M. O., Chen, G., Diskin, G. S., Flynn, J. H., Hostetler, C. A., Holz, R. E., Lang, T. J., Schmidt, K. S., Smith, G., Sorooshian, A., Thompson, E. J., Thornhill, K. L., Trepte, C., Wang, J., Woods, S., Yoon, S., Alexandrov, M., Alvarez, S., Amiot, C. G., Bennett, J. R., Brooks, M., Burton, S. P., Cayanan, E., Chen, H., Collow, A., Crosbie, E., Dasilva, A., Digangi, J. P., Flagg, D. D., Freeman, S. W., Fu, D., Fukada, E., Hilario, M. R., Hong, Y., Hristova-Veleva, S. M., Kuehn, R., Kowch, R. S., Leung, G. R., Loveridge, J., Meyer, K., Miller, R. M., Montes, M. J., Moum, J. N., Nenes, A., Nesbitt, S. W., Norgren, M., Nowottnick, E. P., Rauber, R. M., Reid, E. A., Rutledge, S., Schlosser, J. S., Sekiyama, T. T., Shook, M. A., Sokolowsky, G. A., Stamnes, S. A., Tanaka, T. Y., Wasilewski, A., Xian, P., Xiao, Q., Xu, Z., and Zavaleta, J.: The Coupling Between Tropical Meteorology, Aerosol Lifecycle, Convection, and Radiation during the Cloud, Aerosol and Monsoon Processes Philippines Experiment (CAMP2Ex), Bulletin of the American Meteorological Society, 104, E1179–E1205, https://doi.org/10.1175/BAMS-D-21-0285.1, 2023.

Reisner, J., Rasmussen, R. M., and Bruintjes, R. T.: Explicit forecasting of supercooled liquid water in winter storms using the MM5 mesoscale model, Quarterly Journal of the Royal Meteorological Society, 124, 1071–1107, https://doi.org/10.1002/QJ.49712454804, 1998.

Seidel, J. S., Kiselev, A. A., Keinert, A., Stratmann, F., Leisner, T., and Hartmann, S.: Secondary Ice Production – No Evidence of Efficient Rime-Splintering Mechanism, https://doi.org/https://doi.org/10.5194/egusphere-2023-2891, 2023.

Seifert, A.: On the Parameterization of Evaporation of Raindrops as Simulated by a One-Dimensional Rainshaft Model, Journal of the Atmospheric Sciences, 65, 3608–3619, https://doi.org/10.1175/2008JAS2586.1, 2008.

Seifert, A. and Beheng, K. D.: A double-moment parameterization for simulating autoconversion, accretion and selfcollection, Atmospheric Research, 59-60, 265–281, https://doi.org/10.1016/S0169-8095(01)00126-0, 2001.

Sotiropoulou, G., Ickes, L., Nenes, A., and Ekman, A. M.: Ice multiplication from ice-ice collisions in the high Arctic: Sensitivity to ice habit, rimed fraction, ice type and uncertainties in the numerical description of the process, Atmospheric Chemistry and Physics, 21, 9741–9760, https://doi.org/10.5194/ACP-21-9741-2021, 2021.

Stanford, M. W.: stanford_acp_camp2ex_LES_RSP_DSD, Zenodo [code], 2025.

Stanford, M. W., Varble, A., Zipser, E., Strapp, J. W., Leroy, D., Schwarzenboeck, A., Potts, R., and Protat, A.: A ubiquitous ice size bias in simulations of tropical deep convection, Atmospheric Chemistry and Physics, 17, 9599–9621, https://doi.org/10.5194/ACP-17-9599-2017, 2017.

Stanford, M. W., Fridlind, A. M., Ackerman, A. S., van Diedenhoven, B., Xiao, Q., Wang, J., Matsui, T., Hernandez-Deckers, D., and Lawson, P.: Warm-phase microphysical evolution in large-eddy simulations of tropical cumulus congestus: evaluating drop size distribution

https://doi.org/10.5194/egusphere-2026-4713
Preprint. Discussion started: 21 August 2026


evolution using polarimetry retrievals, in situ measurements, and a thermal-based framework, Atmospheric Chemistry and Physics, 25, 11 199–11 231, https://doi.org/10.5194/ACP-25-11199-2025, 2025.

Stevens, D. E. and Bretherton, S.: A Forward-in-Time Advection Scheme and Adaptive Multilevel Flow Solver for Nearly Incompressible Atmospheric Flow, Journal of Computational Physics, 129, 284–295, https://doi.org/10.1006/JCPH.1996.0250, 1996.

Stevens, D. E., Ackerman, A. S., and Bretherton, C. S.: Effects of Domain Size and Numerical Resolution on the Simulation of Shallow Cumulus Convection, Journal of the Atmospheric Sciences, 59, 3285–3301, https://doi.org/10.1175/1520-0469(2002)059, 2002.

Sullivan, S. C., Hoose, C., Kiselev, A., Leisner, T., and Nenes, A.: Initiation of secondary ice production in clouds, Atmospheric Chemistry and Physics, 18, 1593–1610, https://doi.org/10.5194/ACP-18-1593-2018, 2018.

Sun, Y., Fridlind, A. M., Silber, I., Riemer, N., and Knopf, D. A.: Prognostic simulations of mixed-phase clouds with model AC-1D v1.0: the impact of aerosol types and freezing parameterizations on ice crystal budgets, Geoscientific Model Development, 19, 1581–1617, https://doi.org/10.5194/GMD-19-1581-2026, 2026.

Takahashi, C., Yamashita, A., and Takahashi, B. C.: Production of Ice Splinters by the Freezing of Water Drops in Free Fall, Journal of the Meteorological Society of Japan. Ser. II, 55, 139–141, https://doi.org/10.2151/JMSJ1965.55.1_139, 1977.

Takahashi, T., Nagao, Y., and Kushiyama, Y.: Possible High Ice Particle Production during Graupel–Graupel Collisions, Journal of Atmospheric Sciences, 52, 4523 – 4527, https://doi.org/10.1175/1520-0469(1995)052<4523:PHIPPD>2.0.CO;2, 1995.

Taylor, J. W., Choularton, T. W., Blyth, A. M., Liu, Z., Bower, K. N., Crosier, J., Gallagher, M. W., Williams, P. I., Dorsey, J. R., Flynn, M. J., Bennett, L. J., Huang, Y., French, J., Korolev, A., and Brown, P. R.: Observations of cloud microphysics and ice formation during COPE, Atmospheric Chemistry and Physics, 16, 799–826, https://doi.org/10.5194/ACP-16-799-2016, 2016.

van Diedenhoven, B., Fridlind, A. M., Ackerman, A. S., and Cairns, B.: Evaluation of Hydrometeor Phase and Ice Properties in Cloud-Resolving Model Simulations of Tropical Deep Convection Using Radiance and Polarization Measurements, Journal of the Atmospheric Sciences, 69, 3290–3314, https://doi.org/10.1175/JAS-D-11-0314.1, 2012.

Varble, A., Fridlind, A. M., Zipser, E. J., Ackerman, A. S., Chaboureau, J. P., Fan, J., Hill, A., McFarlane, S. A., Pinty, J. P., and Shipway, B.: Evaluation of cloud-resolving model intercomparison simulations using TWP-ICE observations: Precipitation and cloud structure, Journal of Geophysical Research Atmospheres, 116, D12 206, https://doi.org/10.1029/2010JD015180, 2011.

Varble, A., Zipser, E. J., Fridlind, A. M., Zhu, P., Ackerman, A. S., Chaboureau, J. P., Fan, J., Hill, A., Shipway, B., and Williams, C.: Evaluation of cloud-resolving and limited area model intercomparison simulations using twp-ice observations: 2. precipitation microphysics, Journal of Geophysical Research, 119, 13 919–13 945, https://doi.org/10.1002/2013JD021372, 2014.

Vardiman, L.: The Generation of Secondary Ice Particles in Clouds by Crystal–Crystal Collision, Journal of Atmospheric Sciences, 35, 2168 – 2180, https://doi.org/10.1175/1520-0469(1978)035<2168:TGOSIP>2.0.CO;2, 1978.

Wang, C. and Chang, J. S.: A three-dimensional numerical model of cloud dynamics, microphysics, and chemistry: 1. Concepts and formulation, Journal of Geophysical Research: Atmospheres, 98, 14 827–14 844, https://doi.org/10.1029/92JD01393, 1993.

Wang, L. P. and Grabowski, W. W.: The role of air turbulence in warm rain initiation, Atmospheric Science Letters, 10, 1–8, https://doi.org/10.1002/ASL.210, 2009.

Zeng, X., Zhao, M., and Dickinson, R. E.: Intercomparison of Bulk Aerodynamic Algorithms for the Computation of Sea Surface Fluxes Using TOGA COARE and TAO Data, Journal of Climate, 11, 2628–2644, https://doi.org/10.1175/1520-0442(1998)011<2628:IOBAAF>2.0.CO;2, 1998.